Spring 5-10-2019

Tidal and Subtidal Processes at the Mouth of a Macrotidal Estuary

Rachel Chambers
University of Maine, rachel.chambers@maine.edu

Recommended Citation

Chambers, Rachel, "Tidal and Subtidal Processes at the Mouth of a Macrotidal Estuary" (2019). *Electronic Theses and Dissertations*. 3030.
https://digitalcommons.library.umaine.edu/etd/3030

TIDAL AND SUBTIDAL PROCESSES AT THE MOUTH OF A MACROTIDAL ESTUARY

By

Rachel Chambers

B.S. University of Rhode Island, 2017

A DISSERTATION

Submitted in Partial Fulfillment of the
Requirements for the Degree of
Master of Science
(in Civil Engineering)

The Graduate School
The University of Maine
May 2019

Advisory Committee:

Lauren Ross, Assistant Professor, Civil and Environmental Engineering, Advisor

Kimberly Huguenard, Assistant Professor of Civil and Environmental Engineering

Aldo Sottolichio, University of Bordeaux

TIDAL AND SUBTIDAL PROCESSES AT THE MOUTH OF A MACROTIDAL ESTUARY

By Rachel Chambers

Dissertation Advisor: Dr. Lauren Ross

An Abstract of the Dissertation Presented
in Partial Fulfillment of the Requirements for the
Degree of Master of Science
(in Civil Engineering)
May 2019

Secondary flows and mixing have been shown to influence sediment transport, the vertical salinity gradient, and the exchange flow in estuaries. Typically, these hydrodynamic properties are investigated with respect to time and depth and their variability across the estuary is neglected. However, recent studies have shown that secondary flows and mixing, along with mechanisms that influence them, can exhibit lateral variability. Additionally, the variability of these hydrodynamic properties has not been studied in macrotidal estuaries, where the increased tidal forcing could affect the strength and cross channel variability.

There are two primary objectives of this thesis. The first objective is to investigate the cross sectional and temporal variations in forcing mechanisms of secondary flows and analyze their impact on the observed flow structure. The second is to investigate the cross sectional and temporal variations in mixing and to link the observed patterns to variations in influencing mechanisms of mixing, such as density and vertical shear. To address these research objectives, in-situ collected data and numerical modeling techniques were utilized. Data include horizontal current velocities and TKE dissipation, which were complemented by salinity provided by the numerical model. These data were collected in the Gironde estuary located in southwestern France, a partially mixed macrotidal estuary.

The results indicate that the forcing mechanisms of secondary flows vary intratidally, with the baroclinic pressure gradient forcing a circulation pattern during flood tide and the combination of Coriolis and curvature driving an opposing circulation pattern during ebb tide. The magnitude of the forcing mechanisms vary across the estuary, and this variation is attributed to lateral variations in axial flows and density. Additionally, mixing, quantified through the vertical eddy viscosity, was found to vary across the estuary and exhibited an asymmetric pattern over flood and ebb tides. The lateral variation in mixing was attributed to the lateral asymmetry in peak axial flows, and the tidal asymmetry in mixing was attributed to temporal variations in TKE dissipation, shear, and axial flows. Observed magnitudes of mixing were found to be less than previous studies which was the result of a low dissipation to production ratio, instigated by elevated squared vertical shear.

These results imply that lateral variations in hydrodynamics of a macrotidal estuary with complex bathymetric and topographic features cannot be ignored. The sensitivity to bathymetry and topography suggests that changes in channel geometry could alter internal dynamics and have a wide spread effect on sediment transport and exchange flow.

ACKNOWLEDGEMENTS

This thesis was partially funded by the Bpifrance collaboration with the University of Bordeaux.

I would like to thank my advisor, Dr. Lauren Ross, for her support, encouragement, and incredible patience. Her enthusiasm for coastal engineering was contagious. She made even the smallest bits of progress in my research seem exciting and important, which kept me motivated and turned work into fun. I am so grateful for the opportunities that she has given me these two years; my first trip to Europe and being able to see the estuary that I spent so much time with on Matlab, the PECS conference in Galveston where I got to meet my favorite estuarine celebrities, and help finding a job after graduation.

I would like to thank the Coastal Engineering group for their feedback and encouragement, especially Preston and Sohaib who were always there when I had a quick question and didn't judge if it was really stupid.

Thank you to Dr. Aldo Sottolichio for his contribution to my papers and thesis, and for working around the 6 hour time difference.

I would also like to thank Neil Fisher for the M&M breaks and teaching me how to be a true Mainer. I owe all my kayaking and skate skiing skills to him, as well as the many bruises that I acquired during my first attempts at skijoring. Shout out to Olive and Louis who were patient with me and didn't drag me too far when I fell on my butt!

This whole Masters thing wouldn't have happened if it weren't for the support from my family, #ChambersClan. From late night pep talks to home improvement and bike mechanical lessons via facetime, I knew if I needed help they would be there for me. Dad, I'm sorry I won't be able to provide the 'nectar from the gods' (Marsh Island IPAs) anymore, but I'm sure we can find some good brews in Maryland!

A special thanks to my friend Steph for being my adventure buddy, I will forever remember how under prepared we were for our hiking trip and how much fun it was anyways. Thanks for putting up with me and for distracting me with margarita nights.

TABLE OF CONTENTS

Chapter

LIST OF FIGURES

CHAPTER 1

INTRODUCTION

Estuaries are semi-enclosed bodies of water that connect rivers to the ocean and are characterized as being influenced by river discharge, which brings in fresh water, and ocean tides, which bring in salt water (Cameron and Pritchard, 1963; Fischer et al., 1976; Prandle, 2009; Valle-Levinson, 2010). This mix of salt and fresh water is termed 'brackish' and provides a unique ecosystem that many land, air, and aquatic species rely on (Fisher et al., 1976; NOAA, 2005). Some of the more well known estuaries in the United States are the Chesapeake Bay located on the east coast and the San Francisco Bay estuary on the west coast. Estuaries are important because they provide access to the ocean for shipping, transport, and pollutant dispersion, they provide one of the most productive aquatic ecosystems, and they are used for fishing and recreation (Ji, 2008; NOAA, 2005; Statham, 2012).

Many industrial and commercial centers, such as those near Seattle, WA and Houston, TX, rely on estuaries because they provide direct access to the ocean for shipping and transportation. Shipping centers like those in along Puget Sound in Seattle, WA rely on estuaries to provide an enclosed, protected area for cargo and container ships to dock and unload imports from all over the world. Estuaries can act like a buffer from harsh ocean conditions like strong winds and waves, protecting communities from floods and erosion (NOAA, 2005; Prandle, 2009). Humans also rely on estuaries for recreational purposes such as water sports and beaches, and in the US alone coastal tourism generates \$8 to \$12 billion USD annually (NOAA, 2005). Fishing also brings in billions of dollars yearly, with over 95% of the commercial and recreational fishing catch found in estuaries and in coastal areas (Ji, 2008; Walsh, 1988).

Estuaries are important for the environment as well, and are considered one of the most productive aquatic ecosystems (Ji, 2008; NOAA, 2005). The runoff from land and input from rivers brings in nutrients that support aquatic life, which in turn supports the surrounding ecosystems (Dyer, 1997; Ji, 2008; Savenije, 2006; Statham, 2012). Often the runoff includes pollutants as well as nutrients, and many estuaries have concentrations of toxins from industries, farming lands, and transportation emissions (NOAA, 2005). Some estuaries disperse such pollutants to the ocean, where they can be broken down more easily or can disperse. Estuaries can also trap the pollutants, and the concentrations become higher and can threaten aquatic life and even pose a health risk for those relying on estuaries for food and recreation (Ji, 2008; Savenije, 2006; Statham, 2012). The health of an estuary is very dependent its dynamics.

Estuarine dynamics are sensitive to changes in channel geometry and river and tidal inputs (Prandle, 2009), and are therefore constantly changing (NOAA, 2005; Prandle, 2004, 2006). Humans regularly change estuarine channel geometry by adding in ports, man made islands (for lighthouses or bridge piers), protected harbors, or even by changing the medium of the banks (i.e. sandy beaches, rocks, sea walls, etc.) (NOAA, 2005). In addition, many estuaries need to be dredged, or have the channel bottom deepened manually, to keep a navigation passage deep enough for ships to pass through. River discharge varies seasonally, and can be affected long term by precipitation changes or dams upstream and tides are affected by the rise in sea levels (NOAA, 2005). All of these varying factors can change flow patterns, sediment transport, and mixing processes in an estuary, and therefore it is important to understand these processes to better understand how they are impacted by anthropogenic changes. Before these processes are reviewed, a general understanding of estuarine systems is necessary.

1.1 Estuarine Terminology

An overview of an estuarine system is presented in Figure 1.1. The head of the estuary is at the junction with the river and mouth is at the junction with the ocean. The general

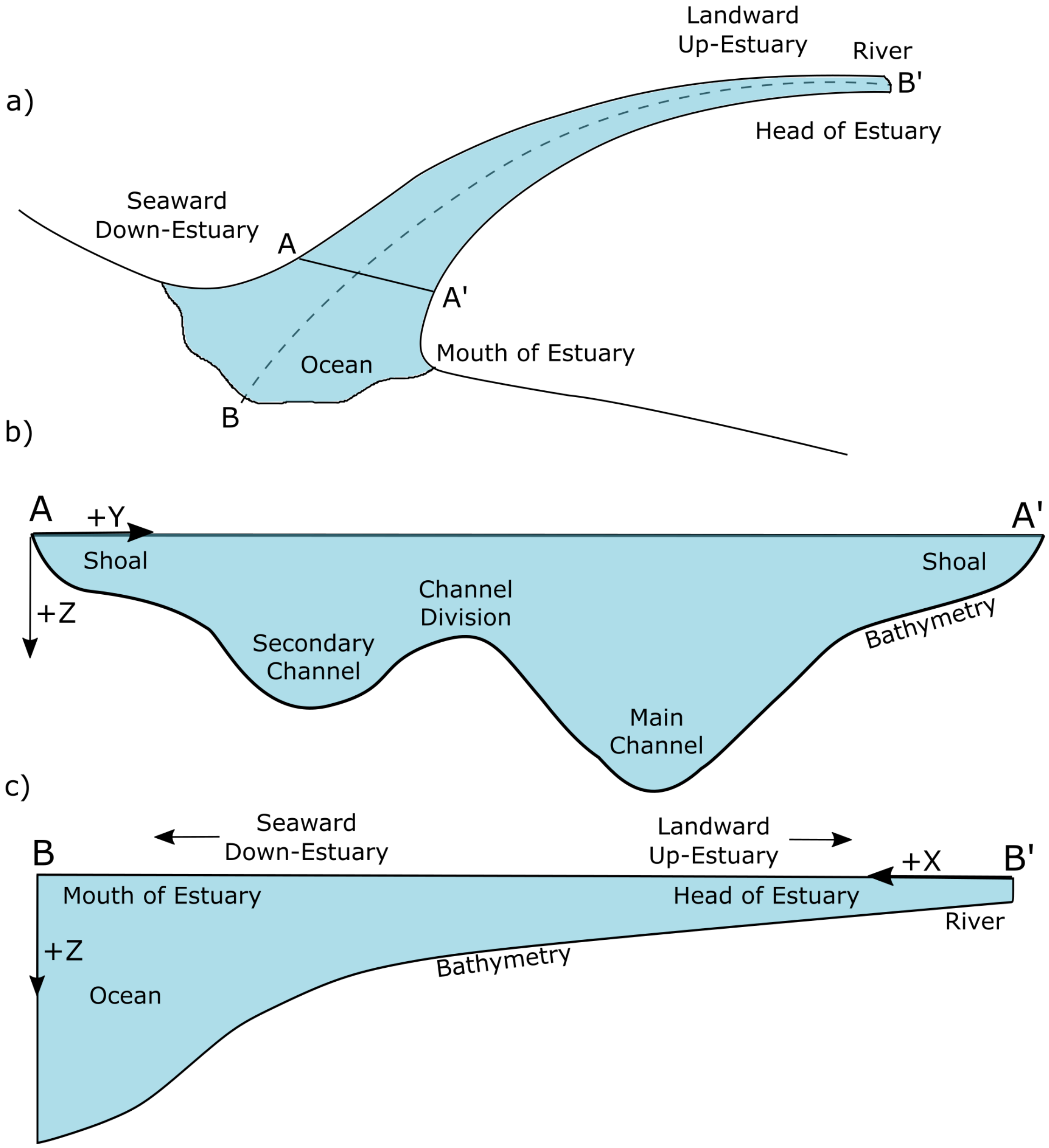

Figure 1.1. Overview of an estuarine system. (a) A plan view of an estuary. (b) A cross section of bathymetry. The y axis direction is the cross-channel and the z axis is the vertical direction. (c) A longitudinal cross section of channel bathymetry from the mouth (at B) to the head (B'). The y axis is the along channel direction and the z axis is the vertical direction.

flow direction is towards the ocean and therefore up-estuary refers to the direction of the head and down-estuary refers to the direction of the mouth. A single cross section taken perpendicular to the channel is called a bathymetric cross section (see Figure 1.1b), which is often used to show the location of bathymetric features such as channels and shoals. In an estuary with one or more channels, the deepest or most prominent channel that is called the main channel and the smaller channels are called secondary channels. In many estuaries the main channel (aka navigation channel or thalweg) stretches from the head to the mouth and is used for navigation. Shallower regions along the shores are called shoals and shallow regions between channels are called channel divisions. Areas that are exposed during low tide and submerged during high tide are called tidal flats, which are prominent in estuaries that feature a large tidal range. The depth of the estuary, or the bottom topography, is called the bathymetry. A longitudinal cross section (Figure 1.1c) shows the bathymetry along the channel.

The geometry of an estuary can change along the channel, and often include inlets, curvature, and headlands (Figure 1.2). Inlets are indentations along the channel. A bend in the along-channel direction alters current velocities and overall estuarine dynamics and is described as curvature effects (Chant, 2010; Geyer, 1993; Nidzieko et al., 2009). Curvature in an estuary can be examined as a piece of a circle. The arc is defined as the path that axial flows take in the region of curvature, and the radius of curvature is the distance between the arc and the imaginary origin. The side of the channel outside the imaginary circle is referred to as the 'outside of the bed' and the inside of the imaginary circle is the 'inside of the bend' (see Figure 1.2). Headlands are land masses, often located at the mouth of an estuary, that intrude on the estuarine channel, restricting the channel width.

Flow traveling parallel to the channel is the along-channel flow, or axial flow, and is often denoted as u and is expressed in m/s. Flow traveling perpendicular to the channel and the axial flow is the across-channel flow, or secondary flow, and is often denoted as v and is expressed in m/s. Both the axial and secondary flows are considered horizontal flows

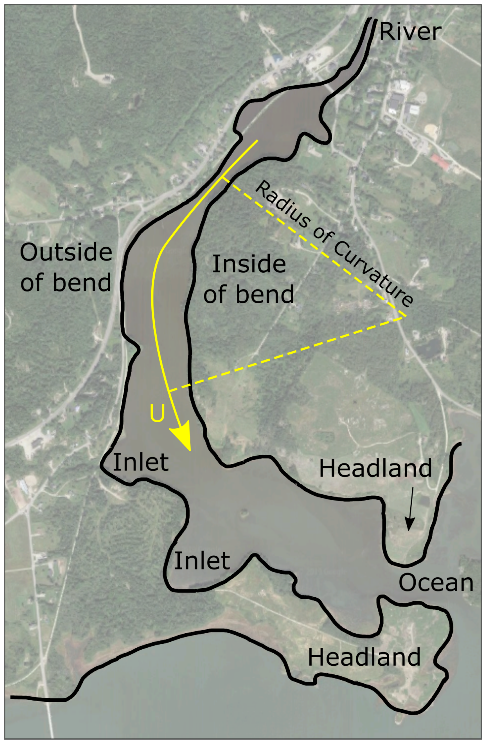

Figure 1.2. Physical features of estuaries. The solid yellow line denotes the path the axial flow takes in a region of curvature, and the dashed yellow lines indicate the radius of curvature. Background satellite image is of the East Machias River estuary on the coast of Maine and is provided by www.google.com/maps.

because they travel in a horizontal plane parallel to the Earth's surface. The secondary flow is typically 10-15% of the strength of the axial flow in straight, idealized estuaries (Chant, 2010; Geyer, 1993). Flow that travels vertically, or perpendicular to the Earth's surface, is called vertical flow and is often denoted as w and is expressed in m/s, but is typically the smaller than axial and secondary flows. In estuaries with curvature the axial flow direction changes along the bend, as seen in Figure 1.2. In these instances the flow directions differ from the $x-y-z$ axes.

There are several different factors that can generate flow in an estuary. Ocean tides generate flows that travel into (flood tide) and out of (ebb tide) the estuary. In addition, river discharge creates a unidirectional flow out of the estuary. The combination of forcing from the ocean and river drives a density gradient along the estuary that induces layered flow, called 'exchange flow', and will be discussed later. Wind can generate surface flows and if it is strong enough can affect flows at mid-depth or deeper (Wong, 1994). Curvature can drive secondary flows through centrifugal forces pushing flows towards the outside of the bend. In the same way, headlands can drive secondary flows because the restriction they create often acts similar to curvature. Secondary flows can also be generated by the Coriolis force. The Coriolis force is the force driven by the rotation of the Earth. In the Northern Hemisphere, Coriolis redirects flows to the right of the initial flow direction and in the Southern Hemisphere Coriolis redirects flows to the left of the initial flow direction. The Coriolis force is dependent on latitude and is stronger at higher latitudes, like Chile and Norway, and weaker near the equator. While every body of water is acted upon by the Coriolis force, only estuaries that have a large enough relative width and depth are significantly influenced by the Coriolis force (Garvine, 1994; Kasai et al., 2000; Winant, 2004). Every estuary has properties that allow for classification by origin, tidal range, and stratification, which will be discussed next.

1.2 Estuarine Classification

Estuaries can be classified by several properties including origin, tidal range, and stratification. Estuaries classified by origin are categorized as fjords, coastal plain estuaries, bar built estuaries, and tectonic estuaries (Pritchard, 1952; Valle-Levinson, 2010). Fjords are estuaries carved out by glaciers and are usually deep (100 - 800 m), have steep banks, and have a relatively shallow ($\sim$ 40 - 150 m) sill at the mouth that restricts flow (Tomczak and Godfrey, 1994). They are typically found at high latitudes such as Scandinavia and Chile, and are characterized by having a fresher surface layer over a distinctly saltier layer that is trapped by the sill. Coastal plain estuaries were formed when the ocean level rises and drowns a river valley, a well known example of a coastal plain estuary is the Chesapeake Bay estuary (Ji, 2008). Bar-built estuaries are enclosed by sand bars or barrier islands, which protect the estuary and ecosystem inside from harsher open-ocean conditions. They are often found in subtropical areas such as near Florida and North

Carolina (Valle-Levinson, 2010). Lastly, tectonic estuaries are formed when a fault in the Earth's crust shifts, sinks, and water fills the area. These estuaries are found in areas with active plate movement such as California.

Estuaries classified by tidal range are categorized as mesotidal, microtidal, macrotidal, and hypertidal. A tidal range is the vertical difference in height between low tide and high tide, and the classifications are typically based on an annual tidal range average. Tides that range from 2 to 4 m are considered mesotidal, or having a moderate tidal range. Tides that have a range less than 2 m are considered microtidal, or having a small tidal range, and tides with a range from 4 to 6 m are macrotidal, or having a large tidal range. Estuaries with a tidal range greater than 6 m are hypertidal (Davies, 1964).

Estuaries classified by stratification are categorized as salt-wedge, partially mixed, and well mixed (Cameron and Pritchard, 1963; Geyer, 2010; Pritchard, 1955; Valle-Levinson, 2010). Salinity is a measure of salt in the water, and the classification system is based off of salinity stratification, which is a measure of the change in salinity between two points. In a salt-wedge estuary (Figure 1.3a) there is a large and sudden change in salinity in the estuary, meaning that the water goes from salty sea water to fresher river water over a short longitudinal distance and there is vertical stratification present. The isopycnals, or interfaces between density layers, are close together and more horizontally aligned, signifying an abrupt vertical change in density. Salt wedge estuaries tend to have a high river discharge to tidal flow ratio, one example of a salt wedge estuary is the Mississippi River estuary (Dyer, 1997). In a partially mixed estuary (Figure 1.3b) there is some vertical stratification, the isopycnals are father apart and steeper, signifying a more gradual longitudinal density change and less vertical stratification than a salt wedge estuary. Partially mixed estuaries typically have a lower river discharge to tidal flow ratio, and most are mesotidal (Dyer, 1997). Well mixed estuaries (Figure 1.3c) have low vertical stratification all the time and are considered vertically homogeneous with vertical isopycnals. Estuaries with a low river discharge to tidal flow ratio are well mixed, and this

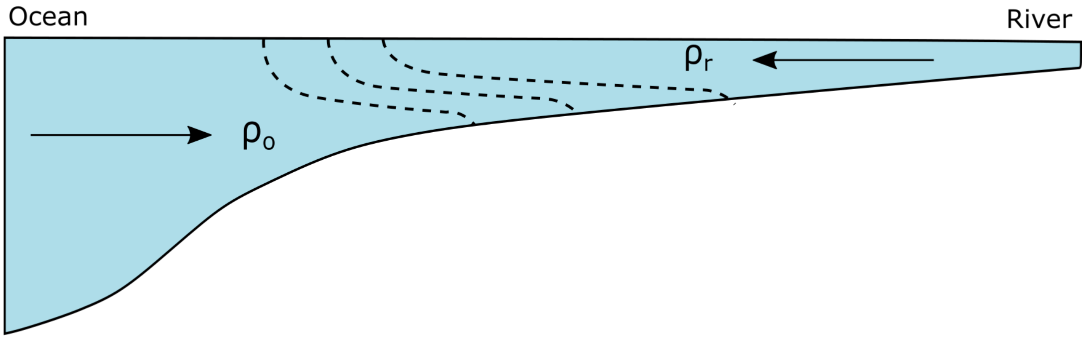

a) Salt Wedge Estuary

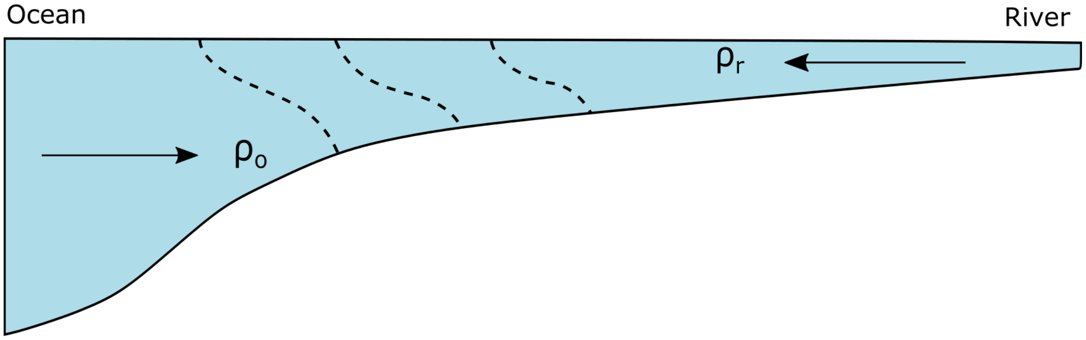

b) Partially Mixed Estuary

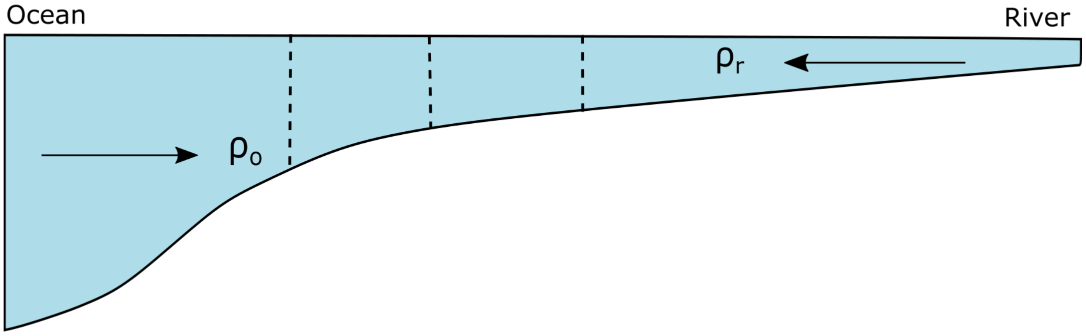

c) Well Mixed Estuary

Figure 1.3. Estuarine classification by salinity. (a) Salt wedge. (b) Partially mixed. (c) Well mixed. The isopycnals (black dashed lines) show the intersection between density layers where ρ_o is the ocean density and ρ_r is the river density and $\rho_o >> \rho_r$.

well mixed environment is more common in macrotidal estuaries (Dyer, 1997). The classification by salinity is especially important because the salinity structure in an estuary can control estuarine circulation (Geyer, 2010). To better understand this process, the affect of salt water brought in by the ocean and fresh water brought in by rivers will be examined, as this creates a longitudinal density gradient that is known to drive long-term circulation in estuaries.

1.3 Ocean and River Influences

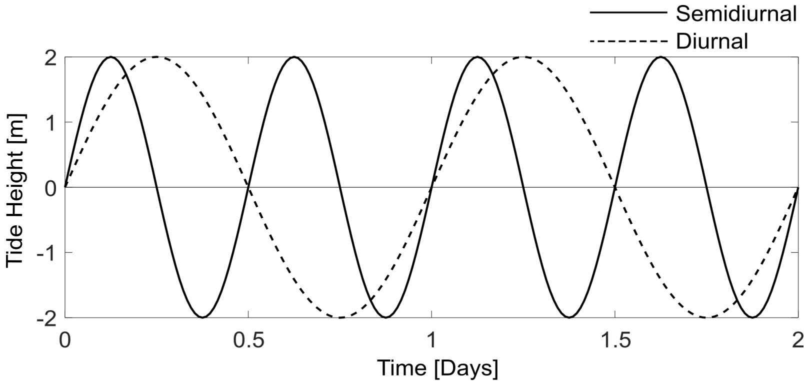

Figure 1.4. Semidiurnal and diurnal tides. A semidiurnal tide (black solid line) and a diurnal tide (black dashed line).

Estuaries are influenced by both the ocean tides, which introduces salt water, and river discharge, which introduces fresh water (Prandle, 2009). The ocean influences estuaries by imposing tides, the most influential of which are either the diurnal tide, with a period of 24.1 hours, or the semidiurnal tide, with a period of 12.42 hours (Figure 1.4). The diurnal tide occurs once a day, meaning there is one high water and one low water per day, and the semidiurnal tide occurs twice daily, or two high waters and two low waters per day. The primary tide is dependent on location, the Gulf of Mexico and the western Alaskan coast both experience diurnal tides, while the east coast of the United States and most estuaries around the world experience semidiurnal tides. Some estuaries are influenced by a combination of diurnal and semidiurnal tides, like the western coast of the United States, which are called mixed tides.

Estuarine processes that occur during periods less than one primary tide in time length are called intratidal processes because they occur during the tidal cycle. An example of an intratidal process is flood and ebb tide, which both occur on a time scale of less than one tidal cycle. In semidiurnal estuaries, flood and ebb tide last ~ 6.2 hours, where flood tide is characterized by water flowing into the estuary, bringing in saltier water from the ocean, and higher water levels. Ebb tide is characterized by water flowing out of the estuary, bringing fresher water from the head to the mouth and lower water levels (Ji, 2008).

Estuaries can also be influenced by longer period tides such as fortnightly tides, also referred to as spring-neap tides. The fortnightly tidal cycle lasts ~15 days and is controlled by the spacial relationship between the Earth, sun, and moon. When the Earth, sun, and moon are aligned spring tide occurs, and when the Earth, sun, and moon are at 90°neap tide occurs. Spring tide brings a larger tidal range than neap tide (Ji, 2008).

Flow induced by semidiurnal, diurnal, or a combination of the two is called intratidal flow because it occurs within the time period of a tide. Flow that is induced by other factors such as a longitudinal density gradient occurs separately from tides and the timescale is referred to as subtidal. One way to think of subtidal flows is to take out the primary tidal components or tidal harmonics. It can also be thought of as a tidal average and what is left over are subtidal flows. Subtidal flows are typically characterized by fresher water near the surface exiting the estuary and saltier water lower in the water column entering the estuary. This distribution is often referred to as the 'exchange flow' because it represents the exchange between ocean water and river/estuarine water, and it is usually driven by the longitudinal density gradient (Geyer, 2010; Pritchard, 1952). The longitudinal density gradient is the change in salinity between sea water (~ 1026 kg/m^3) imposed by the ocean and fresh water (~ 1000 kg/m^3) imposed by rivers (Geyer, 2010; Ji, 2008). The saltier water at the mouth is denser, and sinks below the fresher water at the head, while the less dense fresh water at the head rises until an equilibrium is reached where fresh water forms a layer over the saltier water. The layering of fresher water over saltier water creates a vertical change in density and a sea surface slope that in turn pushes fresh water towards the ocean at the surface and saltier water below the surface towards the head of the estuary, creating the typical subtidal flow pattern (Geyer, 2010).

To gain a better understanding of the factors influencing flows in an estuary it is necessary to look at the governing equations for fluid motion, the Navier-Stokes equations.

1.4 The Navier-Stokes Equations

The Reynolds Averaged Navier-Stokes (RANS) equations are a set of equations that govern fluid motion in three dimensions. They are derived from conservation of momentum and conservation of mass equations and assume that the fluid is incompressible, meaning that density does not change with time. The RANS equations are described as

$$\underbrace{\frac{\partial u}{\partial t}}_{\text{A}} + \underbrace{u\frac{\partial u}{\partial x} + v\frac{\partial u}{\partial y} + w\frac{\partial u}{\partial z}}_{\text{B}} - \underbrace{fv}_{\text{C}} = \underbrace{\frac{1}{\rho}\frac{\partial P}{\partial x}}_{\text{D}} + \underbrace{\frac{\partial}{\partial x}\left[A_x\frac{\partial u}{\partial x}\right] + \frac{\partial}{\partial y}\left[A_y\frac{\partial u}{\partial y}\right] + \frac{\partial}{\partial z}\left[A_z\frac{\partial u}{\partial z}\right]}_{\text{E}} \tag{1.1}$$

for the x-direction flow and

$$\underbrace{\frac{\partial v}{\partial t}}_{\text{A}} + \underbrace{u\frac{\partial v}{\partial x} + v\frac{\partial v}{\partial y} + w\frac{\partial v}{\partial z}}_{\text{B}} + \underbrace{fu}_{\text{C}} = \underbrace{\frac{1}{\rho}\frac{\partial P}{\partial y}}_{\text{D}} + \underbrace{\frac{\partial}{\partial x}[A_x\frac{\partial v}{\partial x}] + \frac{\partial}{\partial y}[A_y\frac{\partial v}{\partial y}] + \frac{\partial}{\partial z}[A_z\frac{\partial v}{\partial z}]}_{\text{E}} \tag{1.2}$$

for the y-direction flow. In these equations u, v, and w are the flow in the x, y, and z direction, respectively. Term A is the local acceleration, or the change in velocity with time t. Term B is the advective accelerations, for example the term $v\frac{\partial u}{\partial y}$ can be expressed as the transport of the along channel flow u in the cross channel direction y by the cross channel flow v. The effect of Coriolis on the flow is expressed in term C, where f is the Coriolis parameter. Term D is the pressure gradient, where P denotes pressure and ρ denotes density, and is a summation of pressures induced by the atmosphere, density, and sea surface slope. Expanded, the pressure gradient term is

$$\frac{1}{\rho}\frac{\partial P}{\partial x} = \frac{1}{\rho}\frac{\partial P_{atm}}{\partial x} - g\frac{\partial \eta}{\partial x} - \frac{g}{\rho}\int_{z}^{\eta}\frac{\partial \rho}{\partial x}dz \tag{1.3}$$

in the x-direction where the first term on the right hand side is the barometric pressure, dependent on the atmospheric pressure P_{atm} and its change along the channel. Typically this term is neglected because of the assumption that P_{atm} is gage pressure since it is constant along the channel. The second term on the right hand side is the barotropic pressure and is the change in sea surface elevation η along the channel. The last term on the right hand side of the pressure gradient equation is the baroclinic pressure gradient, which is the change in density ρ along the channel integrated from the sea surface elevation η to the channel depth z.

The combination of the along channel baroclinic and barotropic pressure gradients control exchange flow (Geyer, 2010). The along channel baroclinic pressure gradient is formed when the salt water at the ocean meets the fresh water from the river (Figure 1.5a) and the difference in density accelerates saltier bottom water up-estuary (Figure 1.5b). This in turn creates a sea surface slope from the mouth to the head, driving a barotropic pressure gradient large enough to overcome the baroclinic pressure gradient and forcing surface water, which is fresher, out of the estuary (Figure 1.5c) (Geyer, 2010; Officer, 1976; Pritchard, 1956). The resulting cross sectional flow pattern exhibits fresh water exiting the estuary at the surface and salt water entering the estuary at depth (Figure 1.5d).

The last term in the RANS equations is term E, which is the friction term where $A_{x,y,z}$ is the eddy viscosity in the x, y, and z direction. Eddy viscosity is a proxy for mixing (Huguenard et al., 2015; Ross et al., 2019), which is the blending of two water masses and will be described in detail later. The A_x and A_y are typically larger than A_z but the changes in the horizontal directions (x and y) are much smaller than the changes in the z direction, and as a result the friction terms are typically simplified to the vertical frictional term, $\frac{\partial}{\partial z}[A_z\frac{\partial u}{\partial z}]$.

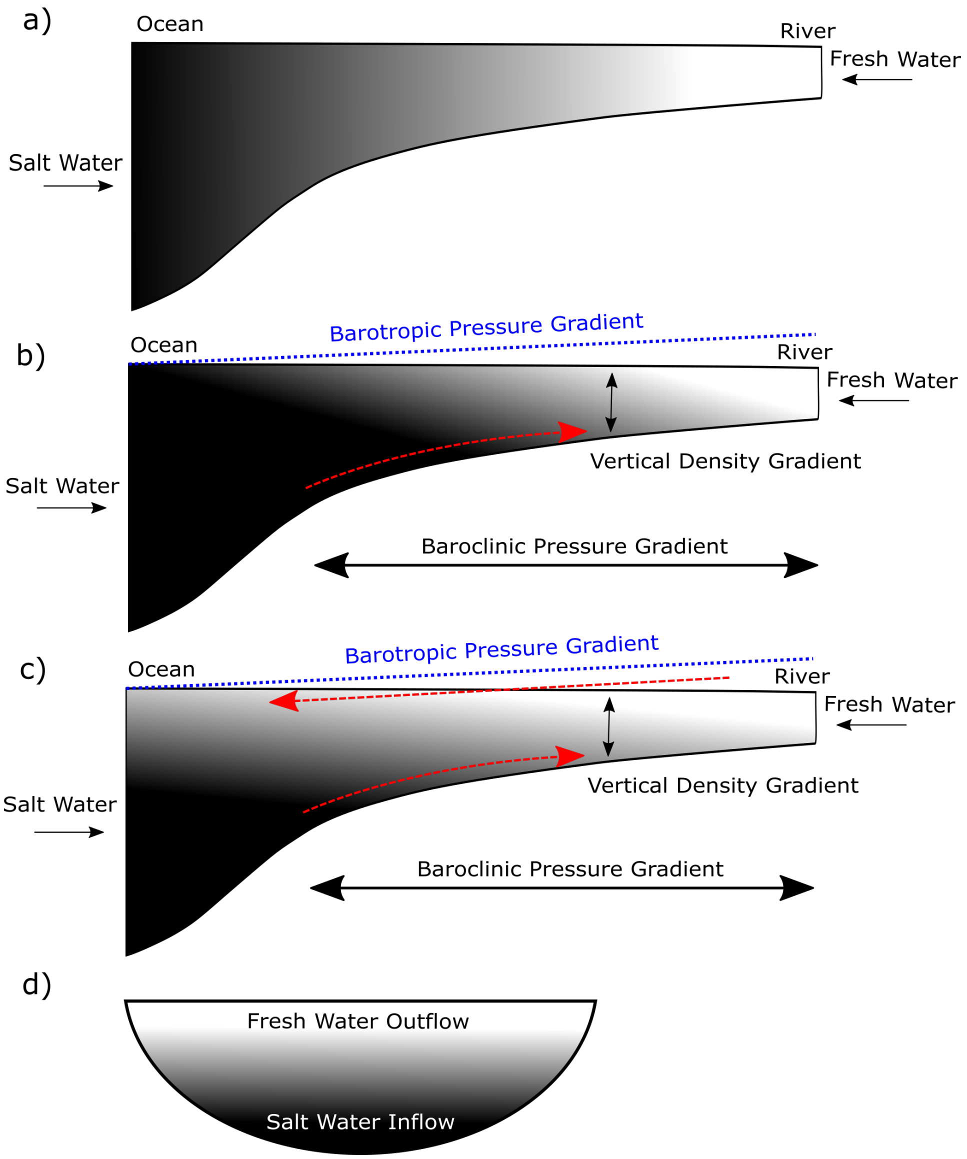

Figure 1.5. Exchange flow driven by barotropic and baroclinic pressure gradients. (a) The horizontal density gradient set up by salt water from the ocean and fresh water from the river. (b) The horizontal density gradient creates a baroclinic pressure gradient as salt water from the ocean accelerates into the estuary (red dashed line). This movement creates a sea surface slope (blue dotted line). (c) The sea surface slope creates a barotropic pressure gradient that drives fresher surface water towards the ocean (red dashed line at surface). (d) The resulting cross section of exchange flows exhibits inflow at the bottom and outflow at the surface.

The RANS equations are used in numerical and analytical models to recreate fluid motion, and they have the ability to be pulled apart so that the influence of each individual mechanism can be examined (see Chant, 2010; Huijts et al., 2009). The mechanisms of along channel flows have been studied extensively as influencing mechanisms of exchange flow (Basdurak & Valle-Levinson, 2013), salt and material transport (Kasai et al., 2000), and tidal straining (Simpson et al., 1990), however their cross channel counterparts have received far less attention. In the last couple decades studies investigating cross channel flows, or secondary flows, have revealed their significance to estuarine systems. The importance of secondary flows and their forcing mechanisms will now be discussed.

1.5 Secondary Flows

The forcing mechanisms of along channel flow have received considerable examination for their influence on estuarine processes. However, recent studies of cross channel flows find that they influence material transport, mixing, exchange flows, and the salinity gradient (e.g. Geyer et al., 1998; Guymer & West; Lerczak & Geyer, 2004; Scully & Geyer, 2012; Smith, 1996; West & Mangat, 1986), which has led to studies of the mechanisms that drive cross channel flows (Buijsman & Ridderinkhof, 2008; Chant, 2010; Li et al., 2014; Pein et al., 2018; Scully et al., 2009). These studies use a secondary flow momentum balance equation, derived from the y-direction RANS by Kalkwijk and Booij (1986), to quantify mechanisms that influence secondary flows. In the secondary flow momentum balance channel curvature is taken into account as a forcing mechanism and the advective terms from the RANS equations are simplified. The resulting secondary flow momentum balance equation is expressed as

$$\frac{\partial u_n}{\partial t} + u_s \frac{\partial u_n}{\partial s} - \frac{u_s^2}{R} + f u_s + g \frac{\partial \eta}{\partial n} + \frac{g}{\rho} \frac{\partial \rho}{\partial n} z - \frac{\partial}{\partial z}(A_z \frac{\partial u_n}{\partial z}) = 0, \tag{1.4}$$

where the coordinate system in a region of curvature is defined as s in the along channel, or streamwise, direction and n in the cross channel, or streamnormal, direction. The first term is local acceleration, followed by the advective acceleration, which is the streamwise advection of the streamnormal flow in the streamwise direction. The third term is curvature, derived from the centrifugal acceleration equation where R is the radius of curvature (see Figure 1.2) (Kalkwijk & Booij, 1986). The fourth term is Coriolis, the fifth and sixth terms are the barotropic and baroclinic pressure gradients, respectively, and the seventh term is friction. Curvature, Coriolis, the pressure gradients, and friction are forcing mechanisms of secondary flow, altering the strength and direction of flow (Chant, 2010; Geyer, 1993).

The intratidal variability of these forcing mechanisms have been studied in mesotidal estuaries and many of these studies concluded that a balance between two or more of these mechanisms is responsible for the observed secondary flow field. Unfortunately, secondary flows in macrotidal estuaries have not been examined and it is unclear how the increased forcing from tides affects secondary flow forcing mechanisms. Additionally, many of the past studies on secondary flows have not investigated lateral variations in forcing mechanisms and how it would affect the lateral secondary flow structure. Consequently, there is a need for further investigation into the lateral variations in forcing mechanisms of secondary flows in a macrotidal estuary.

In addition to lateral variations in secondary flows, lateral variations of estuarine dynamics such as mixing are also often neglected, as they are typically found to be smaller than vertical and temporal variations. However, some studies have shown that lateral variations in mixing, despite often being smaller than vertical and temporal variations, affect residence time, stratification, transport, and exchange flow (Geyer et al., 2008; Huguenard et al., 2015). The properties that influence mixing will now be introduced, along with the energy balance that induces mixing.

1.6 Mixing in Estuaries

Mixing is defined as the blending of two water masses and is an irreversible process (Stacey et al., 2011) that suspends nutrients and sediments in the water column, which if done on moderate scales provides a productive ecosystem (Ji, 2008). However, in estuaries with a high suspended sediment concentration mixing can create cloudy water that inhibits light from permeating and decreases oxygen concentrations in the water, which hinders biological production (de Jong et al., 2014; Statham, 2012; Talke et al., 2009).

Mixing can be analyzed in many ways, the most common method of analyzing mixing is through vertical eddy viscosity A_z, which is a function of axial and secondary flows, density structure, and the turbulent kinetic energy (TKE) dissipation rate. TKE dissipation, ϵ is a physical process that transfers energy to heat and is an energy sink in the TKE equation

$$TKE = T + P + B - \epsilon. \tag{1.5}$$

The transfer of energy from larger scales to smaller scales, T, is typically neglected when discussing TKE in estuaries as it is generally associated with breaking surface waves (Craig & Banner, 1994; Monismith, 2010). The primary source of energy is through production, P, which provides energy to the system via the mean flow. It is quantified by the product of turbulent shear stresses, called Reynolds stresses, and the mean vertical shear (Thorpe, 2007). The potential energy of the system is described through buoyancy flux, B, which can either produce or consume TKE (Monismith, 2010). If the water column is stable, meaning that density is increasing with depth, energy is taken from the system because more energy is required to mix a stable water column than an unstable water column. In most cases the buoyancy flux is an energy sink, with increasing stratification (increase in vertical density changes) taking more energy from the system (Monismith, 2010). Sources and sinks of TKE are related to mixing through A_z, quantified as

$$A_z = \Gamma_m \frac{\epsilon}{S^2}, \tag{1.6}$$

where Γ_m is the mixing efficiency and S^2 is the squared vertical shear. The mixing efficiency is a function of the relationship between buoyancy flux and production via squared buoyancy frequency and squared vertical shear. The squared buoyancy frequency, N^2, describes the stratification in the water column through the vertical density gradient and is expressed as

$$N^2 = -\frac{g}{\rho_0}\frac{\partial \rho}{\partial z}, \tag{1.7}$$

where g is the gravitational constant, ρ_0 is a reference density, and $\partial\rho/\partial z$ is the vertical density gradient. In a stable water column the vertical density gradient is negative because the density is increasing with depth. This means that a positive squared buoyancy frequency describes a stable system while a negative squared buoyancy frequency indicates that there are instabilities in the water column, i.e. there is denser water over fresher water.

The other component of mixing efficiency is square vertical shear, S^2, which is quantified by the summation of axial and secondary squared vertical shear,

$$S^2 = \left\langle \frac{\partial u}{\partial z} \right\rangle^2 + \left\langle \frac{\partial v}{\partial z} \right\rangle^2, \tag{1.8}$$

respectively. Shear is a gradient of velocities and describes how much the velocity changes over a distance. Vertical shear specifically describes the velocity difference throughout the water column. Squared vertical shear and squared buoyancy flux are related through the Richardson number Ri, which is the ratio of buoyancy to production and is expressed as

$$Ri = \frac{N^2}{S^2}. \tag{1.9}$$

At Ri greater than or equal to 0.25 mixing is suppressed by stratification and Ri lower than 0.25 indicate mixing is present (Monismith, 2010; Turner, 1973). The other ratio that controls mixing is the ratio of TKE dissipation to production, which is represented by squared vertical shear. This ratio, ϵ/S^2, describes how much of the energy produced in the system via shear is dissipated, with the dissipation of energy inducing mixing.

As mentioned before, most studies investigating mixing are focused on the vertical and temporal variability of mixing, with cross channel variations largely ignored or averaged out. However, in wide systems or systems with distinct bathymetric features, mixing may show significant lateral asymmetries that could affect the lateral variability of other hydrodynamic processes like the salt and momentum balance, exchange flow, and residence time (Geyer et al., 2000; Hansen and Rattray, 1965; Sanford, 1994).

1.7 Objectives

While providing background information on estuaries and estuarine processes, two research gaps were highlighted. The first was how forcing mechanisms of secondary flows vary laterally and with time in a macrotidal estuary and the second was how mixing varies laterally and with time in a macrotidal estuary. These research gaps provide the motivation for this thesis.

The first objective of this thesis is to examine the generating mechanisms of secondary flows in a macrotidal estuary to determine which are dominant and how they vary across the estuary and with time. To do this, secondary flow forcing mechanisms from the secondary flow momentum equation will be quantified over a semidiurnal tidal cycle and with respect to distance across a macrotidal estuary and compared to observed secondary flows.

The second objective of this thesis is to examine the cross channel and temporal variations in mixing in a macrotidal estuary. This objective will be addressed by quantifying mechanisms that influence mixing and investigating how they change over a semidiurnal tidal scale, with distance across the estuary, and in relation to changes in bathymetry. Through these investigations a better understanding of the lateral variability of key processes in macrotidal estuaries is attained.

1.8 Organization

This thesis is organized as follows.

The second chapter of this thesis examines the generating mechanisms of secondary flows and their spaciotemporal changes in the Gironde, a macrotidal estuary. The third chapter explores the spaciotemporal relationship between hydrographic and hydrodynamic properties in the Gironde, a macrotidal estuary. Following that, the fourth chapter summarizes the conclusions, presents a larger picture of the implications, and discusses potential related work that could expand the understanding of the processes in a macrotidal estuary.

CHAPTER 2

SPACIOTEMPORAL VARIATIONS IN DRIVERS OF SECONDARY FLOW IN A MACROTIDAL ESTUARY[1]

2.1 Chapter Abstract

Observations of current velocity, wind, and river discharge were collected in a macrotidal estuary, the Gironde, located on the southwest coast of France. While many studies have analyzed the forcing mechanisms of secondary flows, none have been carried out in macrotidal estuaries with features such as headlands, channel curvature, and complex bathymetry. To determine the forcing mechanisms of secondary flows, the *in-situ* collected data were complemented by a three-dimensional numerical model to quantify driving mechanisms in the secondary flow momentum balance equation: curvature, Coriolis, and the baroclinic pressure gradient. Current velocity measurements show elevated secondary flows, up to ∼28% of the axial flows, while previous studies have found secondary flows to be 10 - 15% of axial flows in straight channels and 15 - 20% of axial flows in regions of curvature. These elevated secondary flows were accelerated by the baroclinic pressure gradient during ebb tide and the combination of Coriolis and curvature during flood tide. The results show that forcing mechanisms of secondary flows in a macrotidal estuary change over a tidal cycle and with width. Coriolis and curvature have strong intra-tidal variations and change in magnitude across the estuary because of their dependence on axial flows, and the baroclinic pressure gradient is sensitive to the complex bathymetry and changes in magnitude and direction across the estuary.

---

[1] Based on Chambers, R., Ross, L., & Sottolichio, A. (submitted). Spaciotemporal variations in drivers of secondary flow in a macrotidal estuary. *Journal of Geophysical Research.*

2.2 Chapter Introduction

In recent years secondary flows have received increasing attention as an influential force in estuarine dynamics, especially in regions of channel curvature. Secondary flows (also known as cross-channel and lateral flows) are defined as the current velocity normal to the streamwise (along-channel or axial) direction and are typically ∼10% of the magnitude of axial flows (Becherer et al., 2015; Chant, 2012; Lerczak & Geyer, 2004; Pein et al., 2018). Secondary flows have been shown to influence salt and sediment transport (e.g., Geyer et al., 1998; Guymer & West, 1992; Smith, 1996; West & Mangat, 1986; Woodruff et al., 2001), influence vertical mixing (e.g., Lerczak & Geyer, 2004; Seim & Gregg, 1997), contribute to the vertical salinity gradient (Scully & Geyer, 2012), and modify exchange flows (e.g., Becherer et al., 2015; Lerczak & Geyer, 2004). In regions of channel curvature secondary flows can be 15 - 20% of the axial flows (Geyer, 1993), however secondary flows in macrotidal estuaries with curvature have not been studied in detail.

The drivers of secondary flows can be quantified using a simplified secondary flow momentum balance, first presented by Kalkwijk and Booij (1986), to provide insight into what controls the strength, temporal variability, and direction of the flows. The forcing mechanisms of secondary flows and are known to be channel curvature (e.g., Chant, 2010; Geyer, 1993; Kalkwijk & Booij, 1986), rotation (Chant, 2010; Kalkwijk & Booij, 1986), and differential advection due to baroclinic pressure gradients (e.g., Buijsman & Ridderinkhof, 2008; Chant, 2010; Lerczak & Geyer, 2004; Nunes & Simpson, 1985).

Channel curvature or headlands can increase the magnitude of secondary flows and if acting alone can drive a vertical single celled circulation pattern that pushes surface flows away from the bend or headland during both phases of the tide (Geyer, 1993; Lieberthal et al., 2019). Geyer (1993) found that this circulation pattern is created by an imbalance between the centrifugal acceleration and the lateral pressure gradient, which forces surface flows to be directed towards the outside of the bend (or away from the headland) and flows at depth to be directed towards the bend (or towards the headland). This circulation pattern driven by curvature was also observed by Nidzieko et al. (2009) who studied the effect of stratified conditions on curvature driven circulation patterns in a mesotidal salt marsh estuary and Pein et al. (2018) who modeled the flow in idealized mesotidal estuaries. Nidzieko et al. (2009) explored the effect of stratification and tidal asymmetry on lateral flows in a curved channel and found that curvature and stratification competed and created secondary flow patterns that varied from flood to ebb tide as stratification patterns evolved. During flood tide they observed a three dimensional flow pattern from enhanced stratification inducing maximum flows mid water column that were directed towards the outside of the bend. As a result the surface and bottom flows were both directed towards the inside of the bend, creating the three layer flow structure. During ebb tide, if the water column was strongly stratified, the three layer pattern was still present but surface and bottom flows were directed towards the outside of the bend while mid depth flows were directed to the inside. In the case of a well mixed water column during ebb tide, the flow pattern remained a single cell two layer flow pattern similar to that found by Geyer (1993). Nidzieko et al. (2009) shows that the strength of the secondary flow drivers, in this case the baroclinic pressure gradient, can change on an intra-tidal scale. The strong stratification and sharp bends in the estuary created secondary flows that were an order of magnitude larger than the flows generated by Coriolis. While Nidzieko et al.'s (2009) work provides clarity for the relationship between stratification and curvature induced secondary flows, their study was carried out in a mesotidal estuary and may not extend to macrotidal systems.

Another study that investigated the role of the baroclinic pressure gradient is that of Lerczak and Geyer (2004), who studied the roles of secondary flow drivers in idealized straight estuaries that feature vertical density stratification. Under weak stratification they observed a pattern during flood tide where surface flows converged over the thalweg and at depth diverged. During ebb tide surface flows diverged over the thalweg and at depth converged. This vertical two celled secondary flow circulation pattern was driven by density induced differential advection due to a distortion of the along channel density gradient. They found that Coriolis can influence the circulation pattern and create a stronger circulation on one side of the estuary. With strong stratification the lateral flows were weakened substantially compared to well mixed conditions. Because of the correlation with changes in stratification, Lerczak and Geyer (2004) found temporal changes in secondary flows on a fortnightly scale, which have also been observed in other studies such as those by Scully et al. (2009). Scully et al. (2009) found that secondary flows can redistribute momentum, which subsequently alters the axial subtidal momentum balance. Their study investigates secondary flow patterns as a function of depth and time. The secondary flows exhibited a two layer vertical structure during spring tide and a three layer structure during neap tide, a difference which they attributed to a change in the balance of the three driving forces of lateral flows; Coriolis, the barotropic pressure gradient, and the baroclinic pressure gradient. Surface flows were found to be driven by a balance between Coriolis and the barotropic pressure gradient, and flows at depth driven by a balance between the baroclinic and barotropic pressure gradient.

In addition to secondary flow drivers varying with depth, studies have also found that estuary width can influence which drivers control secondary flows. Li et al. (2014) isolated two of the driving forces of secondary circulation, baroclinic forcing and Coriolis, using an idealized numerical model with a straight along-channel section (no curvature) and varying width. They found that without rotation and under weakly stratified conditions, secondary flows formed a two celled convergent pattern during flood and a two celled divergent pattern during ebb. Under strongly stratified conditions without rotation, a two celled convergent pattern was observed during both flood and ebb. When rotation was added there was competition between the baroclinic forcing and Coriolis forcing. At narrow widths, Kelvin numbers below 0.01, the secondary flows formed a two celled convergent pattern and as the width increased (Kelvin numbers from 0.18-1.10) only a single celled circulation pattern was observed, and the direction of rotation switched from flood to ebb.

Pein et al. (2018) observed a similar temporal variation in secondary circulation driven by curvature and the baroclinic pressure gradient in an idealized mesotidal estuary. During flood tides Coriolis opposed the lateral baroclinic pressure gradient, resulting in either a vertical one cell circulation pattern if Coriolis was the dominant force or a convergent two cell circulation pattern if the baroclinic pressure gradient was dominant. During ebb the two forces worked together to create a vertical single cell circulation pattern. Both of these studies shed light on the relationship between Coriolis and the baroclinic pressure gradient, but were done in an idealized straight estuary and an idealized mesotidal estuary, respectively.

Other studies have shown that factors other than curvature, Coriolis, and the baroclinic pressure gradient can affect the formation of secondary flows. Li and O'Donnell (2005) characterized residual flows as a function of channel length, but did so in a straight, narrow channel, neglecting density gradients and Coriolis. They found that in channels with relatively short lengths, with a length parameter of 0.6-0.7, exchange flows at the mouth had inflow over the main channel and outflow over the shoals. In longer channels, with a length parameter <0.7, the exchange flow exhibited the opposite distribution, with inflow over the shoals and outflow in the main channel. Wargula et al. (2018) considered cross-channel wind as a driver of secondary flows in microtidal well mixed estuaries. They found that wind could alter secondary flows in regions of curvature by either enhancing the two layer flow or weakening it. In cases of strong cross channel wind opposing curvature induced two layer flow, the secondary surface flows were driven in the direction of the wind and created three layered secondary flow. Chant (2012) found that tidal range and river discharge can influence the strength and circulation patterns of secondary flow in a mesotidal tidal strait. During low river discharge periods secondary flows were stronger than those during high river discharge, driving single cell circulation patterns. During spring tide single cell circulation patterns were observed, while during neap tide the secondary flows were more complex, resembling a two celled circulation pattern, and the circulation pattern not as prominant as spring tide secondary flow patterns. During neap tides the secondary flows were thought to be shut down by increased stratification, however Chant (2012) did not include salinity data.

These studies have shown the variability in the forcing mechanisms of secondary flow both throughout a tidal cycle and on a fortnightly scale, however have been focused on microtidal or mesotidal estuaries with parabolic cross sections. The goal of this study is to better understand intratidal and lateral variations in the forcing mechanisms of secondary flows in a macrotidal estuary that experiences sharp bathymetric features, curvature, and a headland. In order to reach this goal the following research questions will be addressed: What is the relative role of Coriolis, curvature, and the baroclinic pressure gradient in forcing intratidal variations of secondary flows? And does the strength of the forcing mechanisms responsible for secondary flow generation vary across the estuary? In order to answer the research questions, the secondary flow momentum balance will be quantified, and each of the forcing terms isolated and investigated. This will be accomplished using *in-situ* collected data complemented by three-dimensional numerical model simulations.

In section 2 the Gironde estuary is introduced and described. This is followed by section 3 which describes the methods used to collect and analyze data, including how the secondary flow momentum balance was quantified and the numerical model that was used to supplement *in-situ* collected data. Section 4 presents the results, which highlight the temporal and spacial changes in secondary flow forcing mechanisms by examining slack after ebb, flood, slack after flood, and ebb patterns across the estuary. Additionally, the subtidal secondary flows are presented to show the resulting relationship between the three mechanisms examined on a semi-diurnal scale. The discussion and conclusions follow in sections 5 and 6, respectively.

2.3 Study Area

The Gironde estuary in southwestern France is a convergent, macrotidal estuary that connects the Dordogne and Garonne rivers to the Bay of Biscay on the Atlantic Ocean. It covers a surface area of 635 km^2 (Castaing & Allen, 1981; Jalon-Rojas et al., 2015; Ross et al., 2019) and is approximately 70 km long from the mouth to the confluence of the two rivers (Figure 2.1), with a width ranging from 3 to 10 km. At the mouth the tide ranges from 1.5 m during neap tide to 5.5 m during spring tide (Castaing & Allen, 1981) and is primarily semidiurnal (Ross & Sottolichio, 2016). The average combined river discharge from the Dordogne and Garonne is 760 m^3/s but can reach well above 2000 m^3/s during the wet season (Allen & Castaing, 1973).

The estuary ranges from partially mixed to well mixed due to seasonal variation in river discharge (Allen et al., 1980) and is highly turbid, with suspended sediment concentrations exceeding 10 g/L in the turbidity maximum zone (TMZ), which migrates seasonally between the mid and upper reaches of the estuary (Jalon-Rojas et al., 2015). Increased sediment concentrations have been found to produce hypoxic conditions (de Jong et al., 2014; Talke et al. 2009) especially near the bottom in benthic high concentrations (Abril et al., 1999) or in the upper estuary waters in summer (Lajaunie et al., 2017). Moreover sediment deposits in the Gironde estuary have caused navigational issues that require dredging to maintain a main channel (see Figure 2.1) deep enough for navigation (www.bordeaux-port.fr).

At the southeast bank of the mouth, near Le Verdon, there is a headland that constricts the estuary (Figure 2.1). Outside the estuary, at the opening into the Bay of Biscay, the width is ~23 km across and at the mouth the headland constricts the width to ~5 km. The headland is ~5.7 km long and 5.2 km wide, and upstream of the headland the channel opens up and is ~9 km wide. The northeastern side of the estuary at the mouth exhibits curvature and small inlets and tidal flats, and another smaller headland is seen north of the

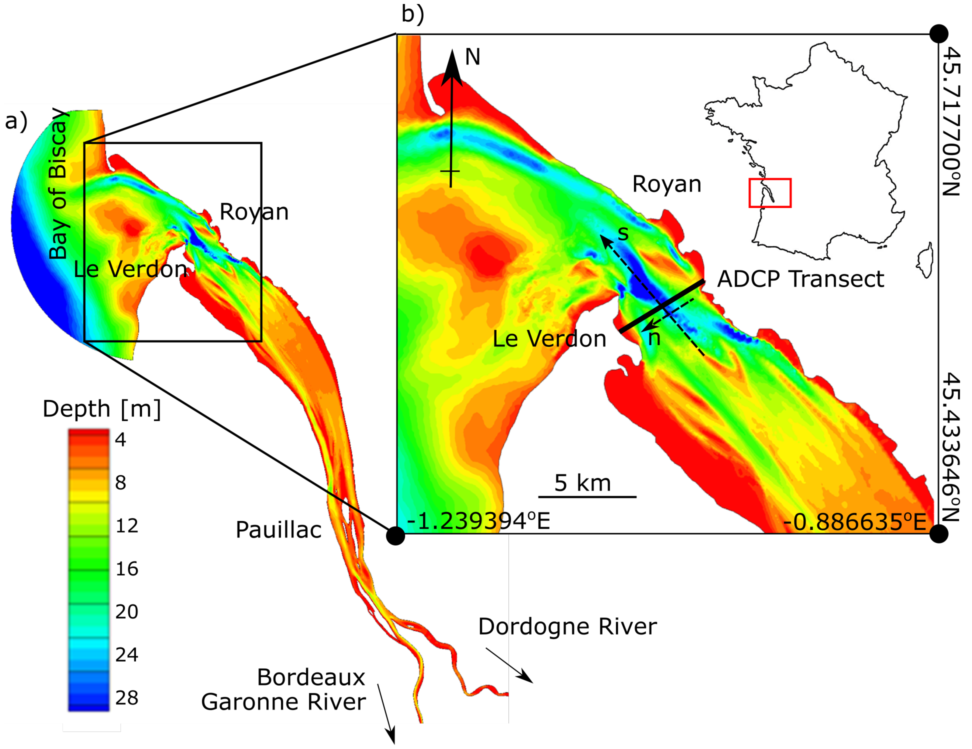

Figure 2.1. Gironde estuary study site with ADCP transect path. The Gironde estuary (a) and a close up of the study site (b). The location within France is shown by the outline of France in the upper right corner, with the estuary boxed in red. The ADCP transects were taken at the mouth of the estuary and are marked by the black line across the estuary at the headland. The dashed arrows indicate the s (streamnormal) and n (streamwise) axis. The contours represent the depth. The navigation channel can be seen in subplot (a) by the yellow contours (∼10 m depth) from the mouth to the confluence of the two rivers, the Garonne and the Dordogne.

mouth in the Bay of Biscay. The constriction and the channel curvature both affect axial and secondary flows, creating high velocities and affecting circulation patterns.

The unique dynamics of the Gironde has made it the centerpoint of many studies (e.g., Jalon-Rojas et al., 2015; Ross et al., 2017; Ross et al., 2019; Ross & Sottolichio, 2016; van Maanen & Sottolichio, 2018), however these studies were completed in the mid to upper reaches of the estuary or during low river discharge and focused on axial flows and/or turbidity and sediment transport, neglecting secondary flows which have been shown to influence both axial flows and sediment transport.

2.4 Methods

2.4.1 Data Collection

Velocity and salinity data were collected on 3 February 2016 during neap tide. The data collection site is shown in Figure 2.1b. On the day of the data collection the combined river discharge was 921 m^3/s and the tidal range was ∼2 m.

Horizontal velocity (axial and secondary flows) and bathymetric data were collected by a vessel-towed 600 kHz Teledyne RDI Workhorse Acoustic Doppler Current Profiler (ADCP) for a full semidiurnal tidal cycle (12.42 h). Data were collected in 50 cm vertical bins at 120 pings per ensemble, and a Garmin GPS was used for navigation. The ADCP transect, shown in Figure 2.1, started at Port Medoc in Le Verdon on the southwestern side of the mouth and ended at Royan, a total transect distance of ∼5.2 km. Each transect took ∼45 minutes to complete, allowing for 16 full transects throughout the tidal cycle. The start of the transect, closest to Le Verdon, will be referred to as the 'left' side and the side of the transect closest to Royan will be referred to as the 'right' side for the remainder of the text.

A second vessel was used to collect cross-channel variations of salinity and temperature with a SeaBird 19Plus Conductivity, Temperature, and Depth (CTD) profiler at five stations across the estuary. The CTD drifted while it was being cast, and after post processing the salinity data exhibited unusual patterns (increasing salinity over the entire tidal cycle, with minimum salinity values of 7 psu, much lower than expected at the mouth) and only collected data within 5 m of the surface. After extensive scrutiny the data were deemed compromised and will not be considered in this study. Density data were provided by a three-dimensional numerical model that will be discussed below in Section 3.3.

In addition to the *in-situ* collected data, river discharge measurements were available by French governmental agencies (data.eaufrance.fr) for the Garonne and Dordogne rivers, which was combined to calculate the total river discharge entering the estuary. Tide heights were collected from a tidal gauge at the mouth of the estuary by the Bordeaux Port

Authority (GPMB). To provide a general idea of the wind conditions in the region, wind speed and direction was collected at Bordeaux Airport.

2.4.2 Data Analysis

The raw data from the ADCP were filtered to remove data with error more than 10% of the maximal flow, less than a signal return of 90% good data, and any velocities less than the ADCP limit of 0.1 cm/s. The velocity and time data were then ensemble averaged and interpolated onto a grid with a horizontal resolution of 10.4 m (creating 500 grid points) and vertical resolution of 0.5 m (creating 74 grid points). The data were rotated to fit the primary axis of flow using a regression analysis (Thompson & Emery, 2014) and the bottom 10% of the data were masked to eliminate side lobe effects.

At the estuary mouth there is a slight curve to the channel as well as a headland that could affect overall flow structure (Figure 2.1). To quantify how curvature affects the flows, a radius of curvature must be defined. The radius of curvature is a function of axial flows and is defined by the curve of the path that the axial flows take (Kalkwijk & Booij, 1986).

The horizontal velocities, radius of curvature, and density data (provided by the numerical model, discussed in section 3.3) were used as inputs into the secondary flow momentum balance equation, which isolates forcing mechanisms of secondary flows. Through this analysis the affects of Coriolis, curvature, and the baroclinic pressure gradient on secondary flow patterns are understood.

2.4.2.1 Secondary Flow Momentum Balance

For this study, a curvilinear coordinate system is used where s denotes the streamwise flow direction, parallel to the channel, and n denotes the streamnormal direction, perpendicular to the channel. Therefore flow in the streamwise direction (axial flows) will be denoted u_s, and flows in the streamnormal direction (secondary flows) will be denoted, u_n. The formation and alteration of secondary flows can be described by the secondary momentum equation derived by Kalkwijk and Booij (1986),

$$\frac{\partial u_n}{\partial t} + u_s \frac{\partial u_n}{\partial s} - \frac{u_s^2}{R} + f u_s + g\frac{\partial \eta}{\partial n} + \frac{g}{\rho}\frac{\partial \rho}{\partial n} z - \frac{\partial}{\partial z}(A_z \frac{\partial u_n}{\partial z}) = 0. \tag{2.1}$$

The first term in the momentum equation is the local acceleration of streamnormal flows and the second term is the streamwise advection of streamwise gradients in the secondary flow (Chant 2010). The third term is the centrifugal acceleration driven by channel curvature, where R is the radius of curvature. The fourth term is Coriolis acceleration, where f is the Coriolis parameter. The fifth and sixth terms are the barotropic and baroclinic pressure gradients, respectively, where η is sea surface elevation, ρ is density, and g is gravitational acceleration. The seventh term is stress divergence, where A_z is vertical eddy viscosity. The first two terms alter the secondary flow after it is generated. Curvature, Coriolis, and the baroclinic pressure gradient are forcing mechanisms of secondary flows (Chant, 2010; Geyer, 1993) and will be the focus of this study. The barotropic pressure gradient and friction are considered both forcing mechanisms of secondary flows as well as products of secondary flows already generated, and therefore will not be considered in this study as primary forcing mechanisms but will be discussed briefly in the discussion.

To better understand the impact the forcing mechanisms, they will each be isolated and quantified. The first forcing mechanism of secondary flows is curvature,

$$\frac{u_s^2}{R}. \tag{2.2}$$

Curvature drives surface secondary flows away from the bend or headland and secondary flows at depth flow towards the bend or headland to satisfy conservation of mass. This single cell vertical circulation pattern is independent of time, although the strength is dependent on both the radius of curvature and the strength of the axial flows (Chant, 2010; Geyer, 1993). The second forcing mechanism of secondary flows is Coriolis,

$$f u_s, \tag{2.3}$$

where the Coriolis parameter is equal to 1.03×10^{-4} s^{-1}, at a latitude of 45°. The circulation pattern driven by Coriolis varies with time because it drives surface secondary flows to the right of the direction of flow in the Northern Hemisphere (Chant, 2010) and is therefore dependent on the temporal variability of flow. In the Gironde, this means that during flood the surface secondary flows are expected to travel to the Le Verdon bank, or to the left side of the cross section looking seaward. During ebb the surface secondary flows are expected to travel to the Royan bank, or to the right side of the cross section. At depth is a return flow satisfying the conservation of mass. The third forcing mechanism of secondary flows is the baroclinic pressure gradient,

$$\frac{g}{\rho}\frac{\partial\rho}{\partial n}z. \tag{2.4}$$

Since the CTD data were compromised, a numerical model was used to attain density values and will be discussed in the following section. The baroclinic pressure gradient, which will be referred to as BCPG, is not dependent on the strength of the axial flows but is dependent on the density changes over the cross section as a result of lateral changes in axial flow. BCPGs drive flows from areas of low density over areas of high density, often creating two-celled vertical circulation patterns due to the transport of less dense surface flows on shoals over denser surface flows in a channel (Chant, 2010; Lerczak & Geyer, 2004).

Each of the secondary flow forcing mechanisms indicates if the secondary flows are being accelerated or decelerated with respect to their direction of motion. If the acceleration and direction of motion are both positive or negative in the reference frame, the secondary flows are being accelerated with respect to the direction they are traveling. If the acceleration and direction of motion have opposite signs the secondary flows are being decelerated with respect to the direction they are traveling.

The secondary flow forcing mechanisms were quantified over one tidal cycle (~12.42h) across the estuary. Because each mechanism induces both a surface flow and an opposing flow at depth, only the surface flows and mechanisms were considered. This was done by taking a depth average of the top 5 m for each of the mechanisms. This simplification helps isolate which mechanisms are driving surface secondary flows without masking them by a depth-average.

2.4.3 Numerical Model

A 3D numerical model was used to simulate hydrodynamics and salinity fields of the Gironde estuary for the specific purpose of providing more complete density data at the sampled cross-section. The finite difference SiAM3D model (Brenon & Le Hir, 1999; Cugier & Le Hir, 2002) used in this study was implemented in the Gironde estuary by Sottolicho et al., (2001). It solves the Navier-Stokes equations with a free surface boundary condition, under the Boussinesq approximation and the hydrostatic assumption in the vertical direction. The turbulence closure uses the eddy viscosity concept based on mixing length theory. An empirical function based on a local Richardson number is added to account for turbulence damping by density stratification (Cugier & Le Hir, 2002). The computational grid covers the Gironde estuary and extends out into the continental shelf of the Bay of Biscay, for a total area of 232 x 326 km. An irregular grid was implemented, with finer resolution in the estuary. In the mouth and in the lower estuary, sourrounding the study area, cell sizes are of 500 x 500 m. The vertical axis is split into 12 layers bounded by fixed horizontal levels with progressively finer resolution from the bottom to the free surface (Lajaunie-Salla et al., 2017). The model is forced with tidal elevation at the shelf, which is calculated from a 21-harmonic composition (Le Cann, 1990). At the upstream limit of the Garonne and Dordogne Rivers, a daily river flow is imposed.

Recent applications by Lajaunie-Salla et al. (2017) and van Maanen and Sottolichio (2018) give detailed updated validation of the model in terms of tidal levels, currents, and salinity. In this study, the model was forced with realistic tides and river discharge to simulate conditions of salinity for a period starting on 1 February 2016 to 9 February 2016.

From this simulation, salinity values of 3 February were hourly sampled and used to support the field data collected for this study.

2.5 Results

Intratidal variability of axial and secondary currents along with wind velocities, river discharge, and water level are presented from observations collected during the high river flow season (February) of 2016 at the mouth of the Gironde estuary. The intratidal flows indicate that the maximum axial flow migrates from the channel during flood to the right shoal during ebb, a transition caused by curvature, Coriolis, and the lateral straining of cross-channel variations in axial flows. The secondary flows show vertical single cell circulation patterns that switch rotational direction from flood to ebb tide.

In addition, the intratidal variation of forcing mechanisms of secondary flows are investigated. Results show that the BCPG is the strongest forcing mechanism during flood and slack tides, and during ebb tides Coriolis is the strongest forcing mechanisms. Typically, looking out of an estuary in the Northern hemisphere, Coriolis creates a counterclockwise vertical circulation pattern during flood tide and clockwise vertical circulation pattern during ebb tide. These patterns are seen over the main channel at the mouth of the Gironde, however they are created not only by Coriolis but by the combination of Coriolis, curvature, and the BCPG. During flood tide curvature and Coriolis oppose each other, allowing the BCPG to influence a vertical counterclockwise circulation pattern. During ebb tide Coriolis and curvature work together, opposing the BCPG and influencing a vertical clockwise circulation pattern.

In the results figures, cross sections of the transect are shown looking seaward, where Le Verdon is on the left side of the cross section and Royan is on the right side of the cross section (see Figure 2.1). Axial flows traveling out of the estuary during flood tide are negative and axial flows traveling into the estuary during ebb tide are positive. Positive secondary flows are traveling to the right, or the Royan bank, and negative secondary flows are traveling to the left, or the Le Verdon bank. The main channel (at ∼3 km across) is the deeper channel (∼27 m depth) near the center of the cross section and the secondary channel (at ∼1.5 km across) is the shallow channel (∼20 m depth) on the left side of the cross section (Figure 2.1b).

2.5.1 Wind, River and Tidal Characteristics

Wind data was collected for 9 days (1 February to 9 February) around the field campaign date (3 February 2016). Winds were strongest in the East-West direction, reaching a maximum of 12 m/s on 7 February 2016. On the day of the field campaign wind speeds reached ∼8 m/s at the end of the day between 18h00 and 23h30, however for the majority of the collection period wind speeds stayed below 5 m/s (Figure 3.2a).

Tides ranged from ∼2 m during neap to ∼5 m during spring, and the mean water level at the mouth was ∼3 m above sea level (Figure 3.2b). Data were collected during maximum neap tide on Feb 3rd when the tidal range was 2 m.

The average river discharge from the combined Garonne and Dordogne rivers is 760 m^3/s (Allen & Castaing, 1973) and maximum discharge during the wet season (late winter through spring) can exceed 2000 m^3/s. Data were collected during the high river discharge season, and on the day of the field campaign the combined river discharge from the Garonne and Dordogne rivers was 921 m^3/s (Figure 3.2c), which is higher than the annual average but is considered low discharge for the wet season.

2.5.2 Intratidal Flows

Cross sections of density, axial flows, and secondary flows are plotted at five time steps during flood and ebb tide. The phase of the tide is determined by a depth and distance averaged axial flow, where negative axial flows denote flood tide (7h00 to 11h30) and positive axial flows denote ebb tide (13h00 to 18h00) as shown in Figure 2.3a. The water level is plotted against the averaged axial flows and is ∼45°out of phase, making it a partially standing wave. Flood tide density and horizontal flows are presented first,

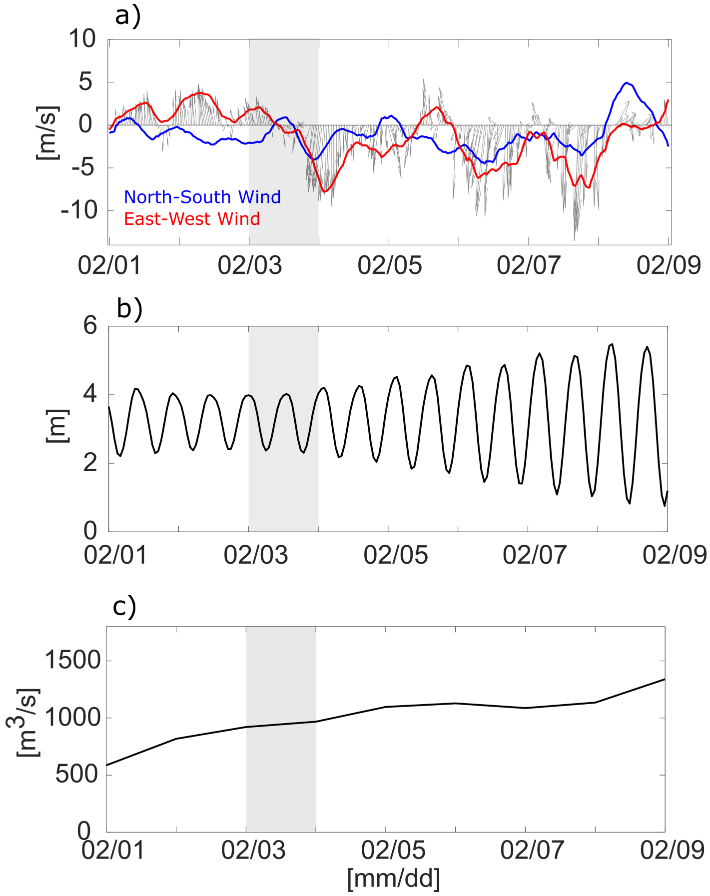

Figure 2.2. Wind, River, and Tide Characteristics. (a) Wind velocity at Bordeaux Airport. North-South winds are in blue with positive values indicating northerly winds, and East-West winds are in red with positive values indicating easterly winds. (b) Width-averaged water surface elevation. (c) Combined river discharge from Garonne and Dordogne Rivers. The discharge rate for the field campaign day was 921 m^3/s. The shaded area in all plots indicates the field campaign day, 3 February 2016.

followed by ebb tide density and horizontal flows. Slack tide density and horizontal flows are presented afterwards and include an analysis of the phase lags in slack tide across the estuary.

2.5.2.1 Flood Tide

At the beginning of flood (8h00) the density cross section (Figure 2.3b1) shows a concentration of less dense water, ~1012 kg/m^3, at the surface on the right side of the estuary while denser flows, ~1019 kg/m^3, are concentrated along the bottom and in the channels, where axial flows (Figure 2.3b2) are bringing in salt water from the Bay of

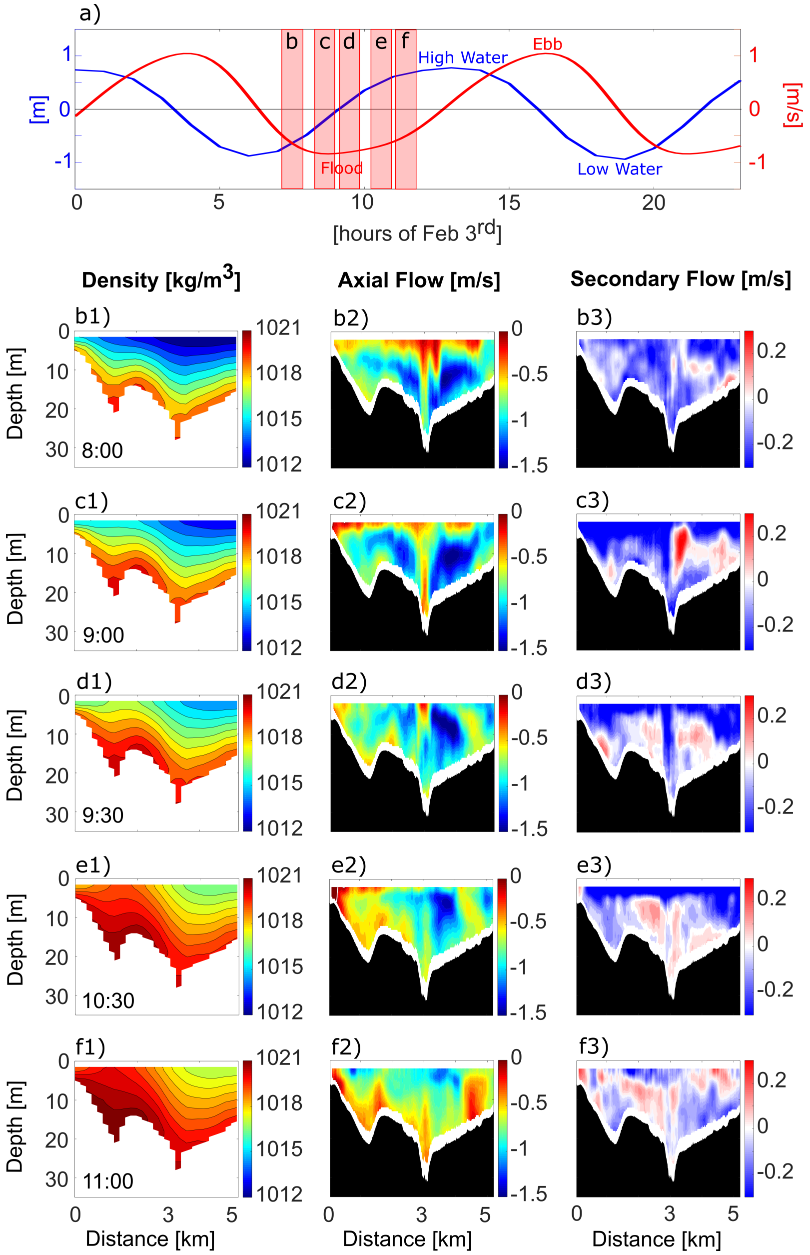

Figure 2.3. Density and intratidal flows during flood tide. (a) Axial velocities and water surface varying with time. The left axis is the water surface (blue line) in meters and the right axis is the depth and distance averaged velocity (red line) in m/s. The red shaded areas indicate the times at which the cross sections of density, axial flows, and secondary flows (plots b through f) were taken. The cross sections vary with depth (y axis) and distance (x axis). All cross sections are looking seaward. (b1), (b2), and (b3) are density (kg/m^3), axial flows (m/s), and secondary flows (m/s), respectively. Each subsequent column represents a new time period during flood tide. Density is shown varying with depth and distance across the channel, with fresher water indicated in blue and saltier water indicated in red. Secondary flows (m/s) traveling left (negative values) are indicated by blue contours and secondary flows traveling right (positive values) are indicated by red contours.

Biscay. The maximum flood tide axial flows (∼1.8 m/s) at 8h00 are concentrated between 10 and 20 m depth and are centered around the main channel and at the surface axial flows are weakest, near zero. Secondary flows (Figure 2.3b3) are traveling between 0 and -0.2 m/s and are directed to the left throughout most of the cross section, with pockets of rightward traveling flows on the right side of the main channel.

The same distribution of density and flows are seen as flood progresses. At 9h00 the flows through the cross section are more dense, with densities of ∼1014 kg/m^3 near the surface on the right and densities of ∼1020 kg/m^3 at the bottom (Figure 2.3c1), retaining the same distribution of fresher and denser water as the cross section at 8h00. Axial flows become stronger and reach ∼ -1.9 m/s (Figure 2.3c2), with a shift in the location of weaker flows from the surface over the main channel (between 2.5 and 4 km, 0 and 10 m depth) to the surface over the left side of the cross section (between 0 and 2 km, 0 to 5 m depth). This migration is driven by the lateral straining of axial flows by the stronger secondary flows (exceeding -0.3 m/s), which push surface axial flows to the left (Figure 2.3c3). The pockets of rightward flows from the previous time step have become stronger as well, exceeding 0.2 m/s over the main channel and stretching from near surface, ∼ 5m, to 20 m depth, indicating the beginning of a circulation cell.

At mid flood (9h30) there is a change in the density, axial flow, and secondary flow patterns. The cross section of density (Figure 2.3d1) exhibits a more distinct lateral change, with a steep isopycnal slope between the secondary and main channels creating a concentration of dense waters on the left side of the estuary between 0 and 2.5 km. At the surface two local minima exist, one on the right side where the fresher water was located during early ebb, between 0 and 5 m depth and 3.5 and 5 km across, and one on the far left side between 0 and 5 m depth and 0 and 1 km across. The maximum axial flows (∼ -1.9 m/s) are now concentrated on the right side of the main channel (between 3 and 4 km) and have shifted up in the water column, between 5 and 15 m depth (Figure 2.3d2). The weakest flows (0 to -0.4 m/s) are found on the far right side and over the main channel at the surface, and on the right side of the cross section another region of weaker flows ($\sim$ -0.7 m/s) forms between 5 and 20 m depth. The secondary flows are traveling to the left at the surface, with flows greater than -0.3 m/s, and are traveling to the right at depth, between 10 and 25 m, with flows $\sim$ 0.1 m/s (Figure 2.3d3). Leftward traveling surface flows and rightward traveling flows at depth create a vertical counterclockwise single cell circulation pattern. The strong secondary flows at the surface transport the weak axial surface flows from the channel to the left shoal, and therefore contribute to the region of fresher water on the left side.

At 10h30 (Figure 2.3e1) and 11h00 (Figure 2.3f1) the cross sections of density retain the same structure as the density at 9h30 (Figure 2.3d1), but have increased maximum densities of 1021 kg/m^3 and 1022 kg/m^3, respectively. Regions of maximum axial flows continue to migrate to the surface and are weakening compared to flows at 9h30 (Figure 2.3d2). Maximum axial flows at 10h30, $\sim$ -1.7 m/s, are located between 5 and 15 m depth and 3.5 and 4 km across (Figure 2.3e2) and maximum axial flows at 11h00, $\sim$1.3 m/s, are located between 0 and 5 m depth and 3.5 and 4 km across. The area of weak flows on the right that were seen at 9h30 (Figure2.3d2) become weaker at 10h30 (Figure 2.3e2) and 11h00 (Figure 2.3f2), reaching near zero between 4.5 and 5 km across.

Secondary flows at 10h30 (Figure 2.3e3) have the same vertical counterclockwise single cell circulation pattern as flows at 9h30 (Figure 2.3d3) where surface flows travel to the left and flows at depth travel to the right. The surface flows are greater than -0.3 m/s and the return flows at depth are less than 0.1 m/s. During late flood, at 11h00, the secondary flows are between -0.2 and 0.2 m/s and the flow structure changes. Surface secondary flows travel to the left in the center of the channel between 2 and 3.5 km, and surface secondary flows over the shoals (between 0 and 2 km and 3.5 and 5 km) are traveling to the right. At depth the secondary flows are traveling to the left over the shoals and to the right in the center of the cross section.

Sharp bathymetric features at the mouth (Figure 2.1) create local effects in axial and secondary flows, which can be seen by abrupt changes in flow over the center of the main channel at the mouth, from 2.9 to 3.2 km across where the bathymetry deepens, but will not be discussed as the focus is on the overall velocity structure and how it varies across the channel. The flow patterns during the ebb phase of the tide will now be presented.

2.5.2.2 Ebb Tide

During early ebb at 14h00 (Figure 2.4a) the cross section of density shows denser water (1019 to 1022 kg/m^3) on the left side of the estuary, concentrated in the secondary channel, and fresher water (1017 to 1019 kg/m^3) at the surface on the right side (Figure 2.4b1). The abrupt changes in density (∼3 kg/m^3) between the secondary channel and the main channel (between 1 and 3 km across) indicate an elevated lateral density gradient. The axial flows (Figure 2.4b2) show inflow at the far left of the cross section between 0 and 0.5 km across and 0 and 5 m depth from the previous flood tide, and outflow over the rest of the cross section, progressively getting stronger toward the right side of the estuary (reaching ∼1.1 m/s between 4 and 5 km). The patch of inflow on the left between 0 and 0.5 km across at the surface could be responsible for the high densities (∼1020 kg/m^3) on the left side. The secondary flows during early ebb are primarily traveling to the right with magnitudes of 0 to 0.2 m/s (Figure 2.4b3), with strongest flows at the surface.

At 15h00 the cross section of density shows the fresher water (∼1017 kg/m^3) moving from the surface at right side of the estuary (Figure 2.4b1, between 3.5 and 5 km, 0 and 5 m depth) to the surface over the main channel (Figure 2.4c1, between 2.5 and 4 km, 0 and 5 m depth). The density change between the secondary channel and the main channel is not as drastic (∼2 kg/m^3) as those at 14h00 (∼3 kg/m^3), reducing the lateral BCPG. The axial flows (Figure 2.4c2) increase in strength from 14h00 to 15h00, reaching ∼ 1.3 m/s, and are concentrated at the surface between 0 and 10 m across the channel section. The weakest flows, near zero, are at depth in the secondary channel. The secondary flows at

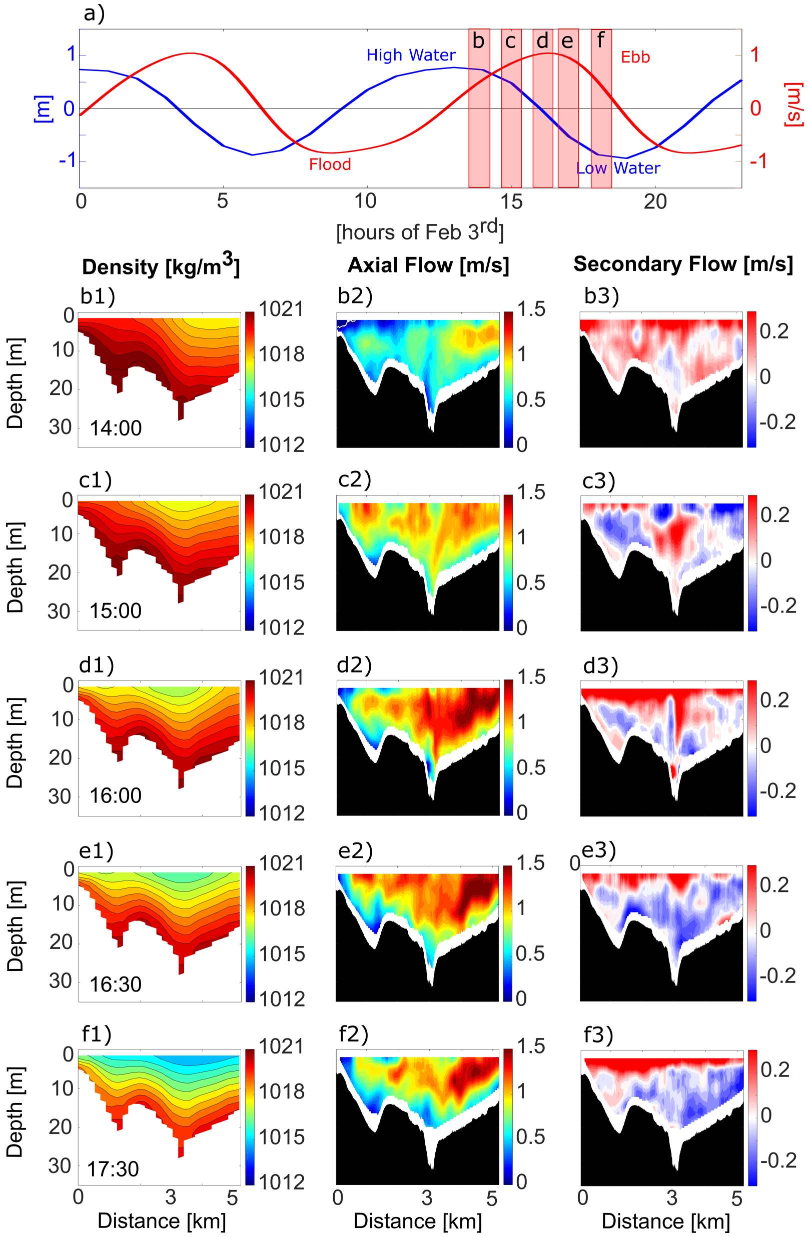

Figure 2.4. Density and intratidal flows during ebb tide. (a) Axial velocities and water surface varying with time. The left axis is the water surface (blue line) in meters and the right axis is the depth and distance averaged velocity (red line) in m/s. The red shaded areas indicate the times at which the cross sections of density, axial flows, and secondary flows (plots b through f) were taken. The cross sections vary with depth (y axis) and distance (x axis). All cross sections are looking seaward. (b1), (b2), and (b3) are density (kg/m^3), axial flows (m/s), and secondary flows (m/s), respectively. Each subsequent column represents a new time period during ebb tide. Density is shown varying with depth and distance across the channel, with fresher water indicated in blue and saltier water indicated in red. Secondary flows (m/s) traveling left (negative values) are indicated by blue contours and secondary flows traveling right (positive values) are indicated by red contours.

15h00 differ in spacial distribution compared to those at 14h00. On the left side of the cross section from 0 to 2.5 km the surface secondary flows are traveling to the right, and at depth travel to the left (Figure 2.4c3). On the right side of the estuary from 2.5 to 5 km the surface flows are generally traveling to the left, and flows at depth are traveling to the right. The overall flow structure can be described as convergent counter-rotating cells. This pattern has been found when the shoals are less dense than the main channel (Lerczak & Geyer, 2004), however the density cross section shows the opposite effect. This unexpected pattern is thought to be due to the barotropic pressure gradient and will be explored further in the discussion section.

During mid ebb (16h00) the density decreases (Figure 2.4d1), with surface densities of 1016 kg/m^3 that stretch over both the main and secondary channels (between 1 and 4.5 km across) and saltier water (1020 kg/m^3) concentrated at depth in the channels, indicating that the density gradient is more pronounced vertically than laterally. The axial flows reach 2.1 m/s and are concentrated on the right side of the cross section from 3 to 5 km and between 0 and 15 m depth (Figure 2.4d2). The flows on the far left and at depth in the channels are near zero. The secondary flows (Figure 2.4d3) at the surface are traveling to the right and exceed 0.3 m/s, and at depth the secondary flows are traveling to the left, ∼0.1m/s, creating a vertical single cell clockwise circulation pattern.

The density and flow patterns at 16h30 and 17h30 are very similar to those during mid ebb. The cross sections of density retain the same distribution as those during mid ebb, but become less dense with surface values of 1015 kg/m^3 at 16h30 and 1014 kg/m^3 at 17h30.

The axial flow structure at 16h30 and 17h30 also remains the same as the flow structure at 16h00, with axial flows at 16h30 reaching 2.1 m/s, and axial flows at 17h30 reaching 1.8 m/s. The secondary flow patterns at 16h30 and 17h30 are both vertical single cell clockwise circulation patterns, with surface flows more than twice as strong (>0.3 m/s) as flows at depth (∼0.1 m/s) (Figures 2.4e3 and 2.4f3).

The transition of axial flows from the center of the channel during flood (Figure 2.3c2) to the right shoal during ebb (Figure 2.4e2) could be a result of the interaction between axial and secondary flows. In typical open channel flow, maximum flows are located over the main channel near the surface and weaker flows are located over the shoals where friction is dominant. The change in axial flow concentration could be due to advection and Coriolis forcing. During ebb the lateral gradient of axial flows could be strained by the secondary flow field, as they are primarily directed to the right side of the estuary. Coriolis directs flows to the right of the direction of flow in the Northern hemisphere (Valle-Levinson et al., 2003), and could also be responsible for the axial flow distribution during ebb.

There is a common density pattern seen during both flood and ebb where the fresher water in the cross section is located at the surface on the right side and the denser water in the cross section is located at depth in the channels. Axial flows exhibit flood-ebb asymmetry in both magnitude and distribution across the cross section. Axial flows are stronger during ebb (max flows ∼2.1 m/s, Figure 2.4d2) than flood (max flows ∼1.9 m/s, Figure 2.3d2), and a calculation of the velocity phase of M_4 relative to M_2 reveals that the tide is ebb dominant at the mouth (Friedrichs & Aubrey, 1988). Ebb dominance could be a result of Coriolis and curvature working together during ebb tide and producing a concentrated axial maximum on the right side of the cross section. Previous studies of tidal velocity asymmetry carried out farther up estuary have found flood dominant velocity asymmetry (Ross et al., 2017), suggesting that flows at the mouth are unique and differ from those upstream. The spaciotemporal averaged axial flow is 0.64 m/s, and the spaciotemporal averaged secondary flow is 0.18 m/s, or ∼28% of the axial flows. The secondary to axial flow ratio is higher than other studies have found. Typically, straight estuaries have secondary flows ∼10% of the axial flows (Chant, 2010; Lerczak & Geyer, 2004) and Geyer (1993) found secondary flows between 15-20% of the axial flows around a headland in Vineyard Sound off of the state of Massachusetts.

The asymmetry between axial flood and ebb flows affects the radius of curvature at the mouth of the Gironde, which will now be quantified.

2.5.2.3 Radius of Curvature

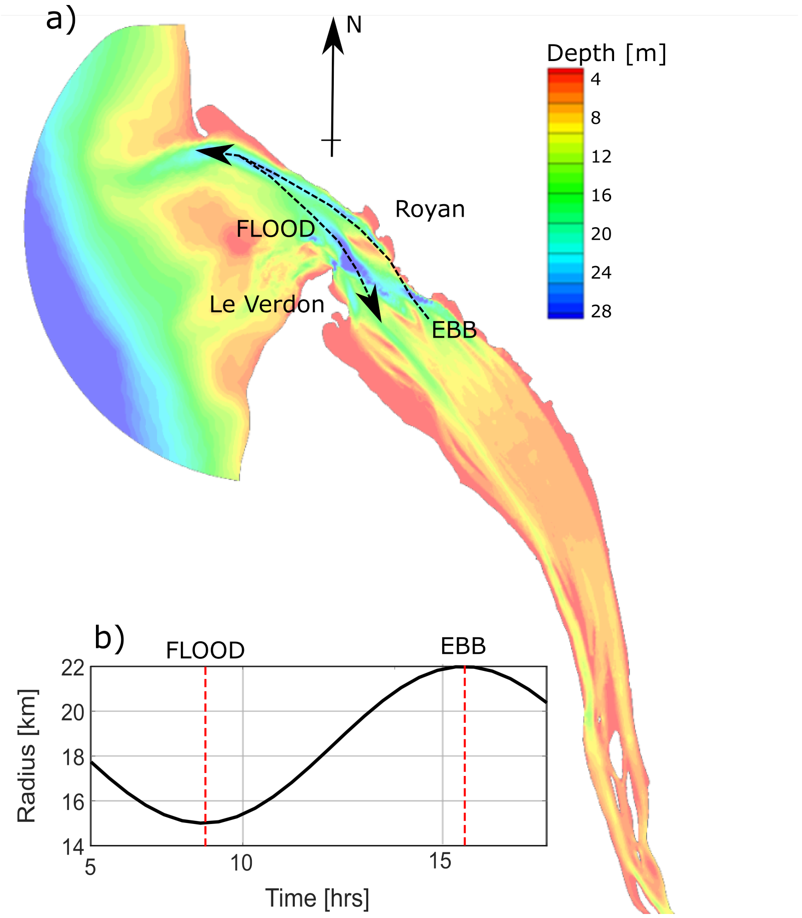

Figure 2.5. Radius of curvature. (a) The proposed radii of curvature with respect to the estuary. The dashed lines show the natural path of the axial flow during flood and ebb. This variability translates into two radii of curvature, a 15.5 km radius curve for flood and a 22 km radius curve for ebb. (b) Variabile radius of curvature throughout the tidal cycle.

The radius of curvature is dependent on the axial flow path (Kalkwijk & Booij, 1986), and at the mouth of the Gironde this path differs during the flood and ebb phases of the tide. Because of this, two radii of curvature can be defined. At the mouth of the estuary (Figure 2.5a) the approximate paths of maximum flood and ebb axial flows are depicted, where maximum flood flows are located in the middle of the channel and maximum ebb flows are located on the right side of the estuary. The associated radii of curvature can be estimated as 15 km during flood and 22 km during ebb. To satisfy both radii, a variable radius of curvature for R in the curvature term is used (Figure 2.5b).

2.5.2.4 Slack Tides

The location of maximum axial flows during flood (Figure 2.3) and ebb (Figure 2.4) affects the distribution of axial flows across the cross section during slack tides. Stronger axial flows carry more momentum than weaker axial flows and therefore tend to take longer to change direction during slack tides than slower axial flows. This implies that axial flows switch from ebb to flood or flood to ebb across the channel at different times, creating a cross-channel phase lag between slack tide axial flows.

Ebb tide depth-averaged axial flows on the right side of the cross section are traveling faster (~1.3 m/s) than flows on the left side (~0.7 m/s) during max ebb (Figure 2.6a from 4h00 to 5h00 and from 16h00 to 18h00). The faster moving flows take more time to slow and switch direction with the tidal phase than the slower flows, creating a time lag between flows on the left of the cross section switching to flood (Figure 2.6a at 5h45) and flows on the right of the cross section switching to flood (Figure 2.6a at 7h00), creating a phase lag of ~1.2 hours. In the cross section of axial flows at the start of slack after ebb (Figure 2.6b) the left side of the estuary (between 0 and 1 km) has started flooding while the center and right side of the estuary (between 1 and 5 km) continues to ebb. The density contours correlate to this axial flow pattern. For example, at depth between 0 and 2 km denser water is found where axial flows are directed in-estuary, while at the surface on the right side of the estuary (between 2.5 and 5 km), there is a pocket of fresher water where axial flows are directed out-estuary.

During flood tide depth averaged axial flows are strongest over the main channel (-1.1 m/s) compared to the left (-0.6 m/s) and right (-0.9 m/s) sides of the estuary (Figure 2.6a from 7h00 to 12h00). Flows on the left switch from flood to ebb first (Figure 2.6a at 12h00)

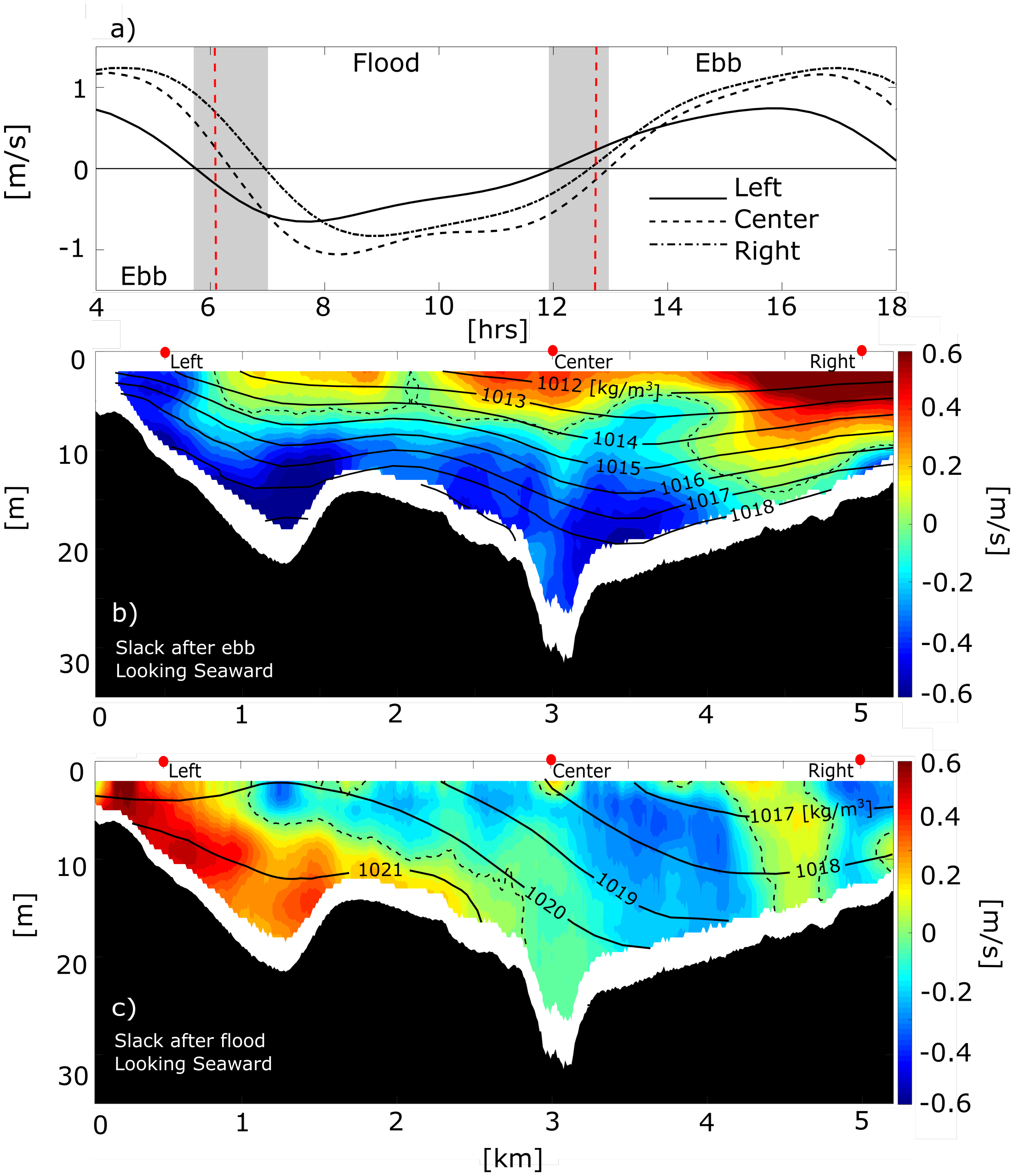

Figure 2.6. Axial flows and density during slack tides. (a) Depth-averaged axial flows taken at the left (0.5 km), center (3 km), and right (5 km) side of the estuary. Slack tides are highlighted in gray. Cross sections of axial velocities (background filled contours, indicated by the colorbars) in m/s are shown for slack after ebb (b) and slack after flood (c), indicated by the vertical red dashed lines in (a). Zero velocities are indicated by the black dashed line and the black contour lines represent density in kg/m^3. The cross sections are looking seaward with depth on the y axis and distance across the estuary on the x axis. In (b) and (c) the three locations (left, center, right) depicted in (a) are marked by a red dot at the surface of each cross section.

and flows in the center switch from flood to ebb last (Figure 2.6a at 13h00), creating a phase lag between the left and center flows of ∼1 hour. The phase lag is seen in the cross section of axial flows during slack tide after flood (Figure 2.6c), where flows on the left side of the estuary (between 0 and 1 km) show out-estuary directed velocities, flows in the center (between 1 and 4 km) are directed in-estuary, and flows on the right (between 4 and 5 km) are directed out-estuary.

Now that axial flows are understood, the mechanisms that generate secondary flows will be investigated in an effort to identify what drives secondary flows and how these mechanisms change with time and with distance across the estuary.

2.5.3 Forcing Mechanisms of Secondary Flows

Three forcing mechanisms of secondary flows, Coriolis, curvature, and the BCPG, were quantified across the channel during slack after ebb, flood tide, slack after flood and ebb tide. The forcing mechanisms reflect the acceleration or deceleration of surface secondary flows from 0 to 5 m depth (quantified as an average over those depths), with the respective cross sectional values of the secondary flows displayed to give a better understanding of the depth-dependent flow structure (Figure 2.7).

Coriolis forcing is dependent on the direction and strength of the axial flow. In the Northern Hemisphere Coriolis accelerates flow to the right, and with respect to the Gironde, Coriolis forces axial landward flows to the left and axial seaward flows to the right from the vantage point looking out-estuary. Coriolis-forced secondary flows create a large single cell vertical circulation pattern (Chant, 2010) where, in the Northern Hemisphere, surface secondary flows travel to the right during ebb, with a return flow at depth traveling to the left, and during ebb travel to the left at the surface with a return flow to the right at depth.

Curvature is dependent on the strength of the axial flows and the radius of curvature, which changes with tidal phase. Surface secondary flows forced by curvature are expected

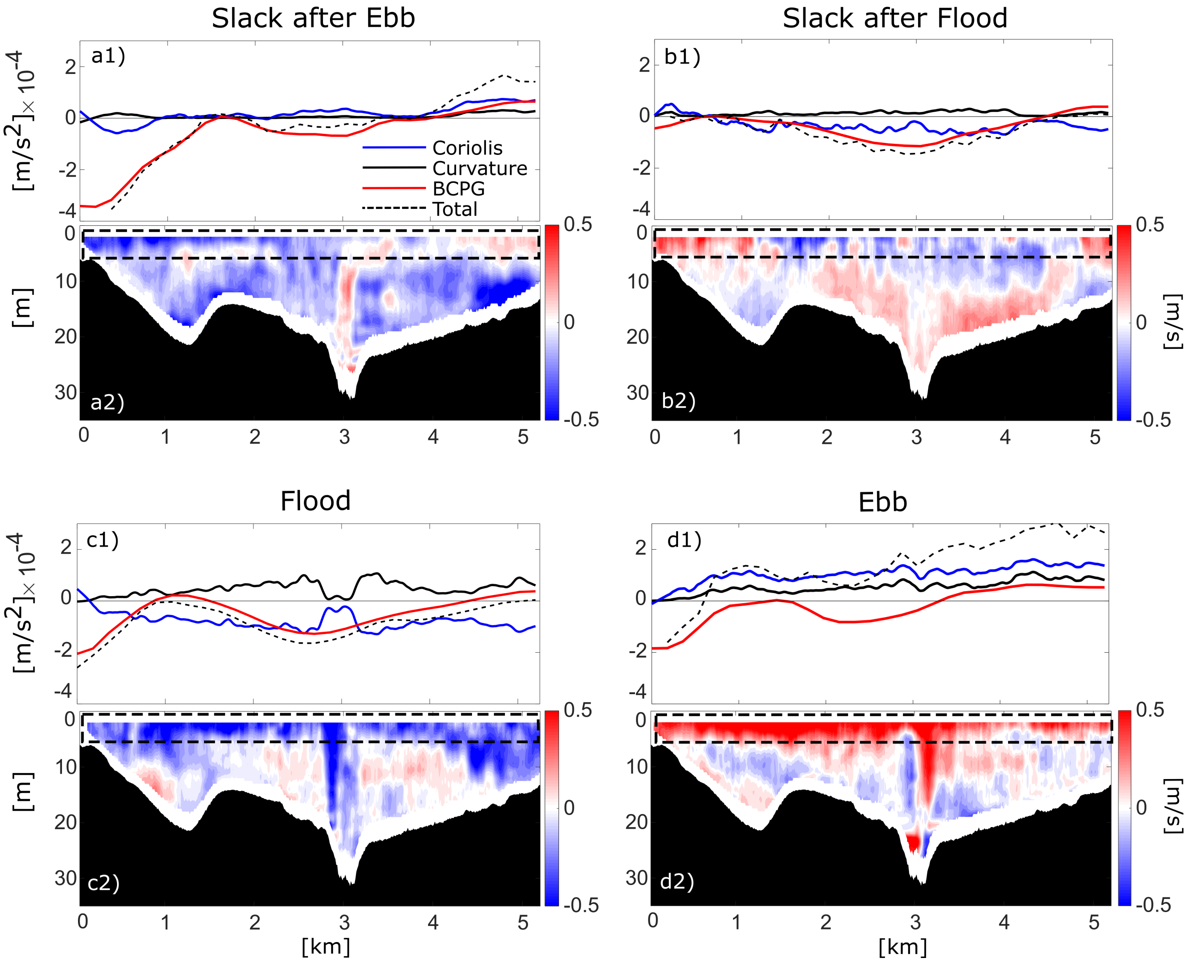

Figure 2.7. Secondary flow generating mechanisms. Secondary flow generators and secondary flows for slack after ebb (a1, a2), slack after flood (b1, b2), flood (c1, c2), and ebb (d1, d2). Curvature is denoted by the solid black line, Coriolis is denoted by the blue line, and the baroclinic pressure gradient is denoted by the red line. The sum of the three is denoted by the dashed black line. The y-axis indicates the strength and of the forcing mechanisms in m^2/s and the x-axis is distance across the estuary. In the cross sections of secondary flows (a2, b2, c2, d2) positive (red) values are to the right and negative (blue) values are to the left. The cross section from the vantage point is looking seaward. The forcing mechanisms reflect the top 5 m of secondary flows, which are boxed in by a dashed black line.

to travel towards the bend (to the right at the mouth of the Gironde) regardless of tidal phase because the curvature of the estuary remains the same with time (Chant, 2010). At depth a return flow to the left is expected, creating a clockwise single cell vertical circulation pattern.

The BCPG is dependent on lateral variations in density. The dominant density pattern found at the mouth of Gironde during high river discharge is fresher water on the right side of the channel at the surface and saltier water on the left at depth (Figures 2.3 and 2.4). This creates a negative pressure gradient that forces secondary flows from the right to the left side of the channel. In response to surface flows traveling to the left, a return flow traveling to the right at depth is expected.

2.5.3.1 Slack Tides

Slack tides are characterized by a change in direction of the axial flow, and exhibit axial flows less than half of the magnitude of the axial flows during maximum flood and ebb tide (Figure 2.6). As a result, the strength of Coriolis and curvature are small ($<1\times10^{-4}$ m/s^2) during slack tide because of their dependence on the strength of the axial flow. The BCPG is not dependent on the strength of the flow but is affected by the lateral changes in density that occur during slack tides as a result of two-directional axial flows.

At slack after ebb the change in density is $\sim$4 kg/m^3 with width and $\sim$6 kg/m^3 with depth (see Figure 2.6b), creating a maximum BCPG of -4×10^{-4} m/s^2 between 0 and 0.5 km (Figure 2.7a1). This spike in the BCPG occurs where there is a change in axial flow direction on the left side of the cross section between 0 and 1.5 km across and is caused by the phase lag across the cross section (Figure 2.6b). The density gradient is negative, and as a result fresher water is being transported over saltier water as secondary flows at the surface are being transported to the left side of the estuary. Because the BCPG is more than four times the strength (-4×10^{-4} m/s^2) of Coriolis and curvature (both are less than 1×10^{-4} m/s^2), it is the dominating forcing mechanism. Coriolis and curvature are weak because the axial flows are weaker during slack tide (~ ± 0.6 m/s maximum) compared to the axial flows during flood and ebb (~ ± 2.0 m/s maximum) (Figures 2.3, 2.4 and 2.6).

The BCPG accelerates leftward-directed surface secondary flows between 0 and 4 km across the estuary (Figure 2.7a2) and the combination of the BCPG, Coriolis, and curvature accelerate rightward-directed surface secondary flows between 4 and 5 km. At depth on the right side there are a leftward-directed return flows (~ -0.4 m/s between 4.5 and 5 km, Figure 2.7a2), indicating the presence of one clockwise circulation cell on the right side of the estuary with the start of a second counter-clockwise circulation cell on the left side of the estuary (looking seaward). As it took ~1 h to transverse the width of the estuary during data collection, the circulation cell on the right of the estuary had more time to become fully developed as compared to the left.

Slack after flood experiences a more consistent lateral density gradient than slack after ebb because the isopycnals are more evenly spaced across the cross section and therefore do not result in a sharp lateral change in density that can be seen in slack after ebb on the left side of the cross section (Figures 2.6b and 2.6c). As a result, the BCPG during slack after flood has no sharp peaks and is of competing magnitude with Coriolis and curvature (Figure 2.7b1). The weaker BCPG ($<-1\times10^{-4}$ m/s^2) can be attributed to a smaller difference in density (~4 kg/m^3) between the inflows and the outflows (Figure 2.6c). Coriolis is briefly positive on the far left of the estuary (from 0 to 0.5 km) where axial flows have switched direction and are directed out-estuary (Figure 2.6c).

In the center and right side of the cross section axial flows are still entering the estuary and as a result Coriolis is negative. Curvature is less than half of the magnitude of Coriolis and is positive, as expected, competing against Coriolis and the BCPG in the center of the cross section (Figure 2.7b1). The cross section of secondary flows shows surface flows traveling to the right between 0 and 1.5 km (Figure 2.7b2) which are accelerated by Coriolis and curvature working together against a weaker BCPG (Figure 2.7b1). From 1.5 to 4.75 km, secondary flows are directed to the left of the estuary (Figure 2.7b2) and are accelerated by Coriolis and the BCPG working in concert (Figure 2.7b1). At the far right side of the estuary (from 4.75 to 5.25 km) the surface flows are once more traveling to the right (Figure 2.7c2) and are accelerated by the BCPG and curvature working together (Figure 2.7b1). The secondary flows at depth are very sensitive to the surface flows. Return flows at depth are opposing the surface flows, and create three separate vertical circulation cells across the estuary (Figure 2.7b2).

During slack tides the weaker axial flows produce weak Coriolis and curvature forcing mechanisms that are often overshadowed by the BCPG. During flood and ebb tides the axial flows are more than twice as strong and are largely unidirectional, and as a result weaker BCPGs and stronger Coriolis and curvature are expected.

2.5.3.2 Flood

During flood tide axial flows reach 1.9 m/s and are concentrated over the main channel below the surface (Figure 2.3d2). This axial flow pattern produces a cross sectional density pattern with fresher water at the surface on the right side of the estuary and saltier water at depth on the left side of the estuary (Figure 2.3 column 1). The resulting BCPG is negative on the left side of the estuary (between 0 and 1 km) and center (between 1.5 and 4.5 km) of the cross section (Figure 2.7c1). On the right side of the estuary over the secondary channel (at 1.25 km across) the BCPG is positive. Coriolis is expected to be negative over the whole cross section but on the far left it is positive from 0 to 0.5 km across, indicating that there is outflow on the far right of the estuary, which is seen in Figure 2.3e2. This is most likely due to an eddy generated by inflow moving around the headland and is seen in other studies such as Geyer (1993) and Lieberthal et al. (2019). However, this warrants further investigation.

Curvature remains positive and is approximately half of the strength of Coriolis, with curvature averaging $\sim 0.5 \times 10^{-4}$ m/s^2 and Coriolis averaging $\sim -0.75 \times 10^{-4}$ m/s^2 (Figure 2.7c1). The summation of all three driving terms is negative from 0 to 5 km, and at 5 km is positive but very weak. The cross section of secondary flows shows surface flows traveling to the left over the entire cross section (Figure 2.7c2). With Coriolis and curvature competing over the majority of the cross section, the BCPG becomes the influential forcing mechanism even though it is of the same magnitude as the other driving forces, $\sim$ -0.75 $\times 10^{-4}$ m/s^2.

2.5.3.3 Ebb

Axial flows are strongest during ebb tide, reaching over 2.1 m/s near the surface on the right side of the cross section (Figure 2.4e2). As a result, both Coriolis and curvature are strongest at this time ($>1\times10^{-4}$ m/s^2) than at any other time throughout the tidal cycle (Figure 2.7d2). Coriolis accelerates rightward-directed secondary flows during ebb and is augmented by curvature forcing (Figure 2.7d1). The combination of Coriolis and curvature is strong enough to overpower the BCPG, which is $\sim \pm$ 0.75 $\times10^{-4}$ m/s^2 and is negative over the two channels (from 0 to 1.5 and 2 to 3.5 km), decelerating rightward-directed flows, and is positive briefly over the division between the two channels (from 1.5 to 2 km) and again on the right side of the cross section (from 2.5 to 5 km), accelerating the rightward-directed flows. On the left side of the cross section, between 0 and 0.5 km, both Coriolis and curvature are close to zero, a result of weak axial flows on the far left side of the estuary (Figure 2.4 column 2). At this location the BCPG is dominating and is -2 $\times10^{-4}$ m/s^2 (Figure 2.7d1). The rightward-directed surface secondary flows are decelerated by the combination of forcing mechanisms, but the strength of the surface secondary flows ($>$0.5 m/s) indicates that another forcing mechanism, such as the barotropic pressure gradient (BTPG), which will be discussed in the discussion, is counteracting the BCPG. The resulting summation of the generators forces a single cell vertical clockwise circulation pattern, with surface flows directed to the right and return flows at depth directed to the left.

2.6 Discussion

This study aims to determine the relative role of Coriolis, curvature, and the BCPG in driving secondary flows at the mouth of a macrotidal estuary and to further determine the intratidal and spatial variability of these forcing mechanisms. Results show that the forcing mechanisms of secondary flows vary over the tidal cycle and with location across the estuary. In this section wind will be ruled out as a potential mechanism augmenting or opposing the secondary flow structure. This is followed by a look into the limitations of this study, as well as the uncertainty around the estimated radius of curvature. Next, the findings from the intratidal flow structure and forcing mechanisms will be extrapolated to understand subtidal flows, including an investigation into the BTPG. The BTPG will be examined since during certain phases of the tide, it is enhanced by the combination of curvature, Coriolis, and the BCPG and therefore could produce a tidally-averaged surface slope that would produce subtidal secondary flows.

2.6.1 Wind

Many studies have found that wind can generate secondary flows in estuaries (Chen et al., 2009; Li & Li, 2011; Wargula et al., 2018). On the day of the field campaign, wind velocities reached a maximum of 4 m/s in the North-South direction and a maximum of 2 m/s in the East-West direction near the study site location. To determine the relative contribution of wind compared to density as an influencing generator of secondary flows, an estimation of the axial and lateral Wedderburn number was calculated. This approach was taken since density was found to be a influential generator of secondary flows. The Wedderburn number (W) is defined as

$$W = \frac{\tau_w L}{\Delta\rho g H^2}, \tag{2.5}$$

where L is the length of the estuary, $\Delta\rho$ is the along channel density gradient, g is the gravitational constant, and H is the average depth (Chen et al., 2009; Geyer, 1997; Li &

Li, 2011; Monismith, 1986). The wind stress, τ_w is defined by $C_D \rho_a |V| \vec{V}$, where ρ_a is the density of air, 1.2 kg/m^3, V is the wind velocity, and C_D is the drag coefficient, of which a typical value of 1.2×10^{-3} is assumed (Chant, 2010). The Wedderburn number represents the importance of the wind stress with respect to the baroclinic pressure gradient force (Chen et al., 2009; Monismith, 1986). If the Wedderburn number is greater than 1, wind stress plays an role in generating surface flows, and if the Wedderburn number is less than 1 wind stress can be neglected as a generator of surface flows (Tenorio-Fernandez et al., 2018). To estimate the impact of wind across the channel, the Wedderburn number was recalculated using $\Delta\rho$ across the channel and L=5000 m, the distance across the channel. The axial Wedderburn number was less than 0.16 and the lateral Wedderburn number was less than 0.13 for the field campaign day. Since wind is considered influential only if the Wedderburn number is greater than 1 (Tenorio-Fernandez et al., 2018), both the along and across channel forcing due to wind can be neglected.

Now that wind has been ruled out as a generating mechanism of secondary flows, the findings can be extrapolated to subtidal flows. Coriolis is expected to play a small role as a subtidal secondary flow forcing mechanism because the magnitude of the Coriolis term should be the same, but in opposite directions, during flood and ebb tide, essentially canceling in a tidal average. Curvature acts in the same direction during flood and ebb and is expected to be positive but weak. The BCPG varies from laterally sheared during flood tide to vertically sheared during ebb tide, a difference that results in a subtidal density pattern indicating that the BCPG is likely a dominating mechanism producing subtidal secondary flows.

2.6.2 Limitations

The model provided salinity data at the surface and at the bottom of the channel for 10 evenly spaced stations across the channel. The salinity was interpolated with depth to provide a two-dimensional cross section of density, as seen in Figures 2.3 and 2.4, which was only used for visual observations. The forcing mechanisms represented surface conditions, and therefore only the surface salinity values across the estuary provided by the model were utilized.

An additional limitation is the estimate of the variable radius of curvature. The radius of curvature for flood and ebb tide were estimated by looking at the location of the maximum axial flows during flood and ebb and their location across the estuary at the mouth, and estimating the path that the axial flows took further downstream at the opening to the Bay of Biscay by looking at the deepest channel. From these two flow paths, radii of curvature were estimated.

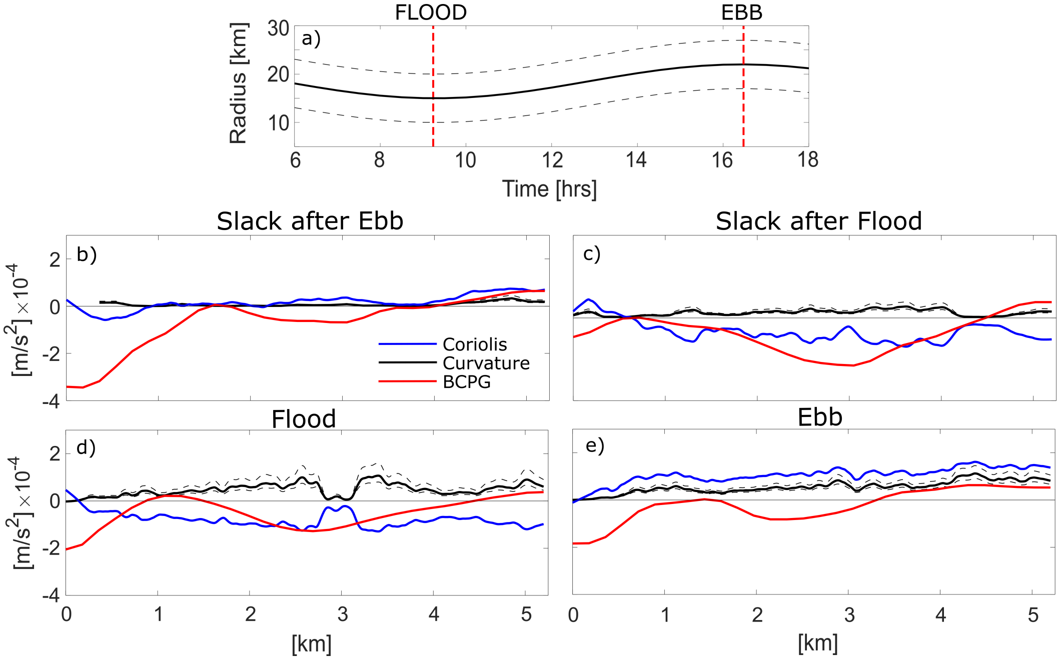

Figure 2.8. Uncertainty in variable radius of curvature. (a)The radius of curvature used for quantifying the curvature forcing mechanism is the solid black line, and the uncertainty, ± 5 km, is denoted by the dashed black lines, with the dashed red lines indicating maximum flood and ebb. (b-e) The forcing mechanisms during slacks, flood, and ebb with the uncertainty lines for the curvature term denoted by the dashed black lines,

The uncertainty in the variable radius of curvature is ± 5 km, as seen in Figure 2.8a. The curvature forcing mechanism does not vary significantly with the uncertainty of the radius of curvature taken into account (see Figure 2.8b-e). This also suggests that the varying radius of curvature does not alter the curvature forcing mechanism significantly and a constant radius throughout the tidal cycle would suffice.

2.6.3 Subtidal Flows

Subtidal flows were calculated using a least squares fit regression analysis (Lwiza et al., 1991) to the main tidal harmonic species, D2 (semi-diurnal), D4 (quarter diurnal), and D6 (sixth-diurnal) after Jay and Kukulka (2003). The analysis was applied to the axial flows, secondary flows, and density to attain the subtidal velocity and density structure. To quantify the subtidal affect of curvature, the time average of the radii of curvature was used.

Axial subtidal flows show outflow concentrated at the surface on the right side of the cross section and inflow concentrated at depth over the two channels (Figure 2.9a), a direct reflection of the location of the maximum axial flows during flood and ebb tides (Figures 2.3 and 2.4). The secondary subtidal flows show surface flows directed to the left of the estuary, with the exception of a small region of surface flows over the main channel, directed to the right of the estuary (Figure 2.9b), which is expected to be a result of the rapid change in depth over the main channel, yet this warrants further investigation.

As expected, subtidal Coriolis acceleration was close to zero and subtidal curvature was positive, indicating flow acceleration toward the outside of the channel bend. However, subtidal curvature acceleration is weak compared to the subtidal BCPG (Figure 2.9c), which is decelerating leftward-directed subtidal secondary flows between 0 and 3.5 km across the estuary (Figure 2.9c). On the right side of the cross section (between 3.5 amd 5 km), the summation of subtidal Coriolis, curvature, and BCPG indicates an acceleration of rightward-directed subtidal secondary flows (Figure 2.9c), however, the subtidal secondary flows are directed to the left of the estuary (Figure 2.9b). This could be the result of the BTPG, which is discussed in the following section.

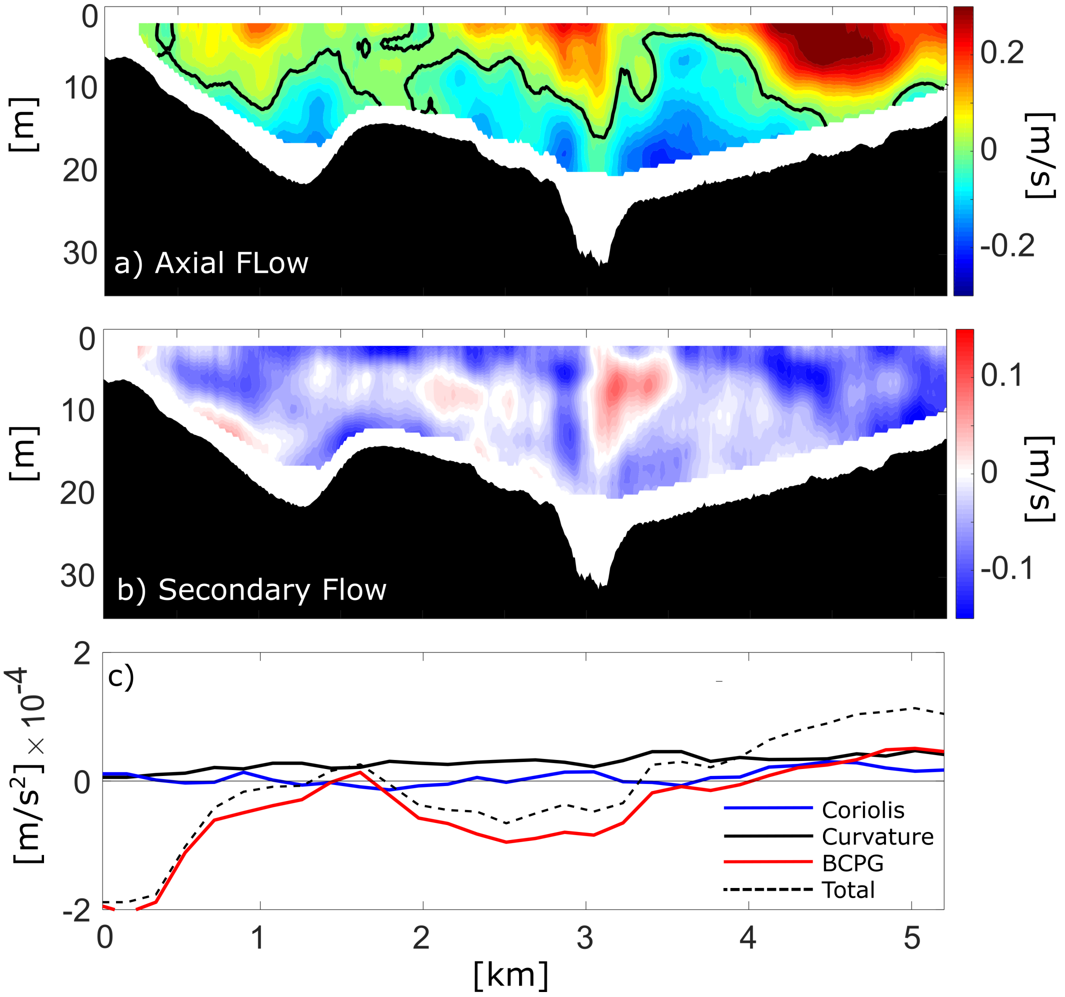

Figure 2.9. Subitdal flows and subtidal forcing mechanisms. Cross sections of subtidal axial (a) and secondary (b) flows and the secondary flow drivers across the estuary (c). Cross sections from the vantage point are looking seaward. Flows are represented by contours and are in m/s. (a) Positive axial subtidal flows (red) are traveling seaward and negative axial flows (blue) are traveling landward, with zero velocities indicated by the black line. (b) Secondary flows traveling to the right are positive (in red) and secondary flows traveling to the left are negative (in blue), with zero velocities in white. (c) Curvature is indicated by the solid black line, Coriolis is indicated by the blue line, the baroclinic pressure gradient is indicated by the red line, and the sum of the three generating terms is indicated by the dashed black line.

2.6.3.1 Barotropic Pressure Gradient

The BTPG is considered to both generate secondary flows and be generated by secondary flows (Chant, 2010). Studies have found that curvature and Coriolis can create a 'pile-up' of axial flows against the outside of a bend in regions of curvature and to the right of the flow direction due to Coriolis in the Northern Hemisphere (Chant, 2010; Valle-Levinson, 2008). This indicates that during a specific tidal phase, Coriolis and curvature work together and subsequently produce a BTPG.

Scully et al. (2009) found intratidal forcing mechanisms of secondary flows in an idealized, straight estuary on the order of 10^{-4}m/s^2, and found that the BTPG balances Coriolis. In their study, the BCPG was smaller than both the BTPG and Coriolis. They observed secondary flows that were 20% of the axial flows. The forcing mechanisms of secondary flows in the Gironde were of the same order of magnitude, but the axial flows were larger ($\sim \pm$ 1.5 m/s) than those seen in Scully et al. (2009) ($\sim \pm$ 1.0 m/s) resulting in secondary flows that were ~28% of the axial flows. Lerczak and Geyer (2004) found that the total lateral pressure gradient (barotropic and baroclinic) was the dominating mechanism forcing secondary flows in stratified or partially mixed idealized estuaries. The elevated secondary flows (~28% of the axial flows) found in the Gironde are produced by elevated axial flows ($\sim \pm$ 1.5 m/s) being modified by the existence of curvature, a cross-channel BCPG and Coriolis working together during certain phases of the tidal cycle. However, the complex bathymetric and topographic features of the Gironde produce tidal asymmetries in secondary secondary flow forcing mechanisms and cross-channel structure, which ultimately contributes to subtidal secondary flows that would not be present in idealized estuary domains.

The tidal asymmetry in secondary flow forcing mechanisms becomes apparent when comparing ebb to flood tide. During ebb tide on the left side of the estuary (between 0 and 1 km), the sum of Coriolis, curvature, and the BCPG in the secondary flow momentum balance is negative ($\sim -2\times10^{-4}$ m/s^2), indicating that rightward-directed secondary surface flows are decelerating (Figure 2.7d). The BTPG at the same cross-channel location (not shown) is $\sim$1.5$\times$10^{-4} m/s^2, accelerating leftward-directed surface secondary flows in opposition to those produced by the other forcing mechanisms in an attempt to balance their effects. During flood tide, Coriolis and curvature are competing and therefore the 'pile-up' of axial flows on the left side of the estuary producing a BTPG is not as pronounced as during ebb tide. This produces a subtidal BTPG that forces subtidal secondary flows.

Therefore, the BTPG is responsible for forcing the leftward directed subtidal secondary flows on the right side of the cross section (between 3.5 amd 5 km), where the combination of Coriolis, curvature, and BCPG do not explain the subtidal secondary flow pattern (Figure 2.9b). In fact, the subtidal BTPG term is negative at this cross-estuary location and reaches ($\sim$ -0.2 $\times$10^{-4} m/s^2), which is nearly as strong as the combination of subtidal Coriolis, curvature, and BCPG ($\sim$0.4 $\times$10^{-4} m/s^2). The small difference in the terms could be explained by friction, which may be counteracting the affects of subtidal Coriolis, curvature, or the BCPG, but could not be resolved in this study.

The distribution of subtidal flow patterns and forcing mechanisms at the mouth of this macrotidal estuary can be explained by the intratidal flow and density patterns combined with lateral variations in water levels (Figure 2.10). Intratidal secondary flows create a build up of water on either side of the estuary, creating lateral sea surface slopes. During flood the lateral sea surface slope is negative due to secondary flows piling up on the left side of the estuary from Coriolis (Figure 2.10 Flood). During ebb the sea surface slope is positive due to the combination of Coriolis and curvature augmenting each other (Figure 2.10 Ebb), producing a larger water level slope than that of flood. The subtidal sea surface slope is a direct result of the variation between intratidal flows, and the resulting subtidal BTPG forces subtidal secondary flows to the left. However, the affects of cross channel bathymetry can alter unidirectional flows driven by the BTPG and BCPG but this warrants further investigation.

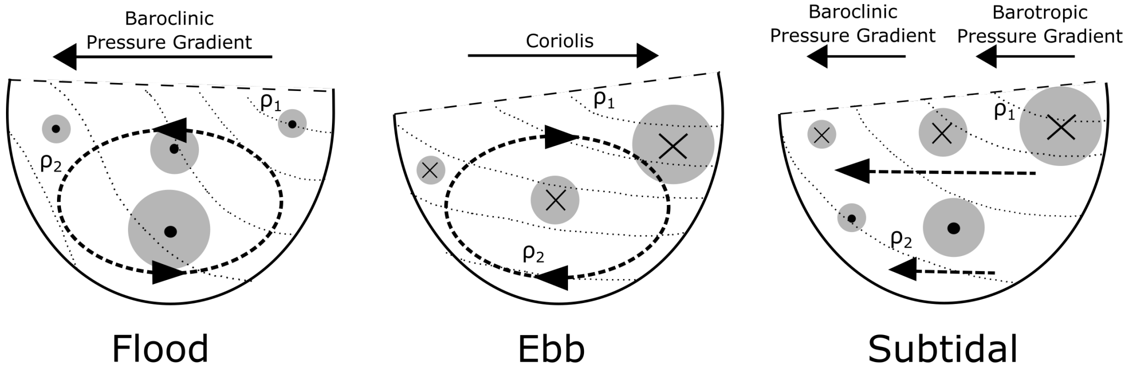

Figure 2.10. Cartoon of intratidal and subtidal flows and density structure. Schematic showing the cross sections, looking seaward, of (a) flood, (b) ebb, and (c) subtidal currents and density structure across the estuary. Axial flows are denoted by the shaded circles, a dot indicates landward flows and a cross indicates seaward flows. The size of the circle indicates the strength of the axial flows, with the largest circles indicating maximum axial flows in the cross section and the smallest circles indicating near-zero flows. The dashed ellipses show the secondary flow circulation patterns with the direction denoted by the arrows, and the lateral sea surface slope is shown by the dashed lines at the surface of the cross sections. The dotted lines within the cross section are isopycnals, where ρ_1 and ρ_1 denote the local densities and $\rho_1 < \rho_2$. The dominant drivers of intratidal and subtidal secondary flows are labeled above each cross section along with the direction that they drive secondary surface flows.

2.7 Chapter Conclusions

This study investigated intratidal variations in the lateral structure and forcing mechanisms of secondary flows in a macrotidal estuary with complex topographic features such as curvature, headlands, and non-idealized bathymetry. The results conclude that the dominant secondary flow forcing mechanisms vary throughout the tidal cycle and with distance across the estuary, which had direct influence on subtidal flow strength and structure. During ebb tide the baroclinic pressure gradient was responsible for forcing secondary flows while during flood tide Coriolis dominated. The intratidal variation in secondary flow drivers produced tidal asymmetries in cross-channel, lateral flow structure, thus producing secondary subtidal flows. Subtidal current velocities were a reflection of the intratidal processes. In particular, Coriolis and curvature produced a surface slope during ebb tide which was not as pronounced during flood, resulting in subtidal secondary flows forced by a combination of the baroclinic and barotropic pressure gradients.

Understanding the forcing mechanisms of secondary flows allows for the identification of processes responsible for salt and sediment transport, vertical mixing, the vertical salinity gradient, and the exchange flow. This study emphasizes that intratidal and subtidal forcing mechanisms of secondary flows must be taken into account when evaluating material and sediment transport in macrotidal estuaries with sharp bathymetric and topographic features. Future research on secondary flow structure in macrotidal estuaries would benefit from investigating the role of friction in augmenting or inhibiting the influence of Coriolis, curvature, and the baroclinic pressure gradient. In addition, more research is needed on the the along-channel variability of the axial and secondary flow structure and drivers to fully understand the inter-connectivity of secondary flow generating mechanisms.

2.8 Chapter Acknowledgements

Authors would like to thank Guillaume Detandt (EPOC), Energie de la Lune (EDL), and Jean-Philippe Mauros for their help with the data collection, and Pascal Brunet (Bertin Technologies) for his support. This work is a contribution to the URABAILA Project, financially sponsored by Bpifrance in collaboration with the University of Bordeaux. Data are available through http://dataverse.acg.maine.edu/dvn/dv/chambers.

CHAPTER 3

INVESTIGATION OF TIDAL ASYMMETRIES AND CROSS CHANNEL VARIABILITY OF MIXING IN A MACROTIDAL ESTUARY

3.1 Chapter Abstract

Intratidal and cross channel variability of mixing in a macrotidal estuary is explored in this study using observations of current velocity, TKE dissipation, wind, and river discharge from the Gironde estuary in southwestern France. While intratidal asymmetries in influencing mechanisms of mixing such as shear, stratification, and TKE dissipation have been studied extensively, investigations into the lateral variability of these properties and their reaction to bathymetric effects are lacking. To determine the temporal and cross channel variability of mixing, the mechanisms that influence mixing are investigated. Intratidal flows collected by a vessel-mounted Acoustic Doppler Current Profiler (ADCP) traversing the estuary, and revealed secondary flows exhibiting dependency on bathymetry. Squared vertical shear and squared buoyancy frequency exhibited tidal asymmetry and reliance on depth, with elevated values corresponding to shallower sections of bathymetry. The resulting Richardson number also varied with time and bathymetry, with values below the critical Richardson number of 0.25. TKE dissipation was calculated from shear measurements from a Vertical Microstructure Profiler (VMP) at three stations across the estuary and displayed variation with time and distance across the channel. The vertical eddy viscosity was calculated as a proxy for mixing and exhibited dependency on axial flow strength and variation in distance across the estuary, showing elevated mixing in locations of peak axial flows. The vertical eddy viscosity values were several magnitudes lower than a similar study in the Gironde estuary, which was attributed to a low TKE dissipation to TKE production ratio induced by elevated shear.

3.2 Chapter Introduction

Turbulence mixing in estuaries is an essential process that impacts the momentum balance, the salt balance (Geyer et al., 2000; Hansen and Rattray, 1965; Peters, 1999; Pritchard, 1952), exchange flow, residence time, particle distribution (Brand et al., 2010; Geyer et al., 2008; Sanford, 1994), and biological dynamics (Cloern, 1991; Koseff et al., 1993). In past decades, studies investigating mixing have been primarily focused on variations with depth and time (eg. Geyer et al., 2008; Li et al., 2008; Peters, 1997; Peters, 1999; Peters & Bokhorst, 1999; Pieterse et al., 2015; Scully & Geyer, 2012; Ross et al., 2019), with less focus on lateral asymmetries in mixing and the effect of bathymetric changes. Studies that have examined cross channel variations in mixing have found that it affects stratification, residence time, exchange flow, and scalar transport in estuaries (Geyer et al., 2008; Huguenard et al., 2015). An investigation of the mechanisms instigating these cross sectional and temporal variabilities in mixing would expand the understanding of how these variabilities influence estuarine dynamics.

Lateral variations in mixing are often attributed to lateral variations in hydrodynamic properties such as horizontal currents, shear, and stratification. Axial (along-channel) and secondary (cross-channel) flows can change laterally as a result of forcing mechanisms such as Coriolis, curvature, pressure gradients, and friction (Buijsman & Ridderinkhof, 2008; Chant, 2010; Chambers et al., submitted; Geyer 1993; Kalkwijk & Booij, 1986; Lerczak & Geyer, 2004; Nunes & Simpson, 1985) and have also been found to change in response to bathymetry, often as a result of bathymetric-induced changes in density gradients (Friedrichs & Hamrick, 1996; Kasai et al., 2000; Valle-Levinson et al. 2003; Wong, 1994). Huijts et al. (2009) found cross channel asymmetries in residual flows and concluded that they were a result of tidal rectification processes, specifically advection of along channel momentum and secondary flows induced by Coriolis.

While a direct link between lateral variability in axial and secondary flows to lateral variability in mixing is not often analyzed, several studies have connected peak axial flows with high turbulence (Ralston and Stacy, 2006; Rippeth et al., 2001, 2002; Wiles et al., 2006), indicating that lateral variations in these peak flows can induce lateral variations in mixing. The affect of tidal asymmetries in mixing on exchange flows has received considerable attention, and investigations have found that tidal asymmetries in mixing can induce residual currents of equal magnitude as baroclinicly driven residual flows (Basdurak et al., 2013; Burchard & Hetland, 2010; Cheng et al., 2010; Geyer et al., 2010; Huijts et al., 2009; Jay & Musiak, 1994; Stacey et al., 2001; Scully & Friedrichs, 2007). Scully and Friedrichs (2007) and Huijts et al. (2009) show that lateral asymmetries can reverse the typical exchange flow pattern, modifying the residual circulation to exhibit landward flow over shoals and seaward flow in the channel. In addition to connections between mixing and horizontal flows, past research has linked lateral asymmetries in shear to asymmetries in mixing, as mixing is promoted by vertical shear (Turner, 1973). One such relationship is between bed shear stress and water depth. French and Clifford (1992) and Traynum and Styles (2007) found that larger vertical shear stress values occur at relatively shallow depths (i.e. over the shoals) and with larger velocities. The relationship between shear and mixing indicates that if vertical shear is spatially variable with respect to depth, or bathymetry, mixing will also vary over bathymetry and exhibit increases over shallow depths.

Another hydrodynamic property that influences mixing is vertical stratification, which acts to shut down mixing (Turner, 1973). Stacey et al. (2011) linked stratification to changes in bathymetry, with less stratification over shoals and increased stratification over channels. Since stratification is indirectly proportional to mixing, decreased mixing is expected over channels and increased mixing is expected over shoals. This relationship is explored by Scully and Friedrichs (2007) who found that decreased stratification over shoals led to increases in mixing throughout the tidal cycle, and in the channel temporal asymmetries in stratification led to intratidal variations in mixing. There are several other studies that have examined the temporal relationship between stratification and turbulence and found the same inverse relationship where increased stratification leads to decreased turbulent mixing (eg. Chant et al., 2007; Geyer et al., 2010; Jay & Smith, 1990; Nepf & Geyer, 1996; Simpson et al., 2005; Stacey et al., 1999; Stacey & Ralston, 2005; Rippeth et al., 2002). Temporal changes in other hydrodynamic properties have also been investigated for their affects on turbulence and mixing.

In a study of turbulence on a shoal-channel interface in a straight, partially stratified estuary, Collignon and Stacey (2013) found that bed friction generated turbulence over the majority of the tidal cycle, from slack after ebb through mid ebb, and during late ebb lateral circulation generated elevated turbulence. Huguenard et al. (2015) found that in a microtidal estuary near surface Coriolis-induced lateral changes in density led to straining of the lateral density gradient, which, coupled with straining of the velocity shear, produced spacial and temporal variations in mixing that was located near the surface and detached from bottom generated turbulence. In a similar study, Basdurak et al. (2017) examined the relationship between mixing and the Richardson number and found bathymetric-driven lateral variations in density and flow fields induced both spacial and temporal asymmetries in the Richardson number, which instigated spacial and temporal asymmetries in mixing. Ross et al. (2019) explored intratidal and fortnightly variations in mixing in a macrotidal estuary and found that during neap tide mixing was inhibited by increased stratification, and at the end of flood and ebb tide there was increased near-surface mixing, decoupled from the bottom boundary layer, due to Coriolis forcing enhancing vertical shear. But their study did not investigate lateral variations in turbulence to determine if the near surface mixing was maintained along-channel.

Several studies have explored how tidal flows interact with changes in bathymetry (Kasai et al., 2010; Valle-Levinson et al., 2003; Wei et al., 2017; Wong, 1994). In an investigation of how changes in bathymetry, Coriolis, and friction alter exchange flows, Valle-Levinson et al. (2003) found that in low friction scenarios and depending on the location of the thalweg, Coriolis and density induced flows either coincide and create a concentrated inflow over the thalweg or they conflict and the inflow is laterally spread. Wei et al. (2017) found that changes in bathymetry can alter salt transport and the density distribution in a well mixed convergent estuary and reinforced conclusions made by Wong (1994) where denser water settles in the channel and drives an exchange flow pattern with landward flow concentrated in the channel.

These studies have shown temporal and cross channel variability in mixing and have linked this variability to one or more hydrodynamic properties that influence mixing, however these investigations were typically done in mesotidal, straight estuaries with parabolic cross sections or during low river discharge periods. The goal of this study is to better understand cross channel and intratidal variations in mixing in a macrotidal estuary with complex bathymetry during high river discharge season. The following research questions will be addressed to reach this goal: How do mechanisms that influence mixing change over a semidiurnal tidal cycle? What is the relationship between bathymetric features and lateral changes in mechanisms that influence mixing? In order to answer these research questions each process that influences mixing will be quantified and depth averaged, and then investigated for temporal and cross channel variability with a concentration on how the cross channel variability links to bathymetric changes. This will be accomplished using *in-situ* collected horizontal velocities and TKE dissipation data and complemented by salinity data provided by a three-dimensional numerical model simulation.

The study area, the Gironde estuary, is introduced in section 2. The methods are then described in section 3, including data collection, a description of the numerical model, and data analysis. This is followed by the results in section 4, which highlight the spacial and temporal variations in hydrodynamic properties by presenting each process varying with time and distance, and then time and distance averages for more precise investigation. The discussion in section 4 summarizes the results and presents other factors that may be influencing turbulence and mixing, and is followed by the conclusions in section 5.

3.3 Study Area

The Gironde estuary is located in southwestern France, connecting the Bay of Biscay to the Garonne and Dordogne rivers (Figure 3.1a). The estuary is ∼70 km in length and the tidal affects are felt ∼160 km from the mouth. The Gironde is convergent, with a maximum width of 10 km near the mouth and a minimum width of 3 km near the head. At the mouth there is a headland constricting the estuary to a width of 5 km before the channel opens up again and is ∼10 km wide (see Figure 3.1b). The depth ranges from 5 to 30 m, with a main channel (seen in Figure 3.1a,c) stretching from the mouth, where it is ∼30 m in depth, to the Garonne river, ∼8 m in depth.

The estuary is primarily semidiurnal and is considered macrotidal, with a tidal range of 1.5 m during neap tide and 5.5 m during spring tide (Allen & Castaing, 1973; Castaing & Allen, 1981; Ross & Sottolichio, 2016). The annual average river discharge from the combined Garonne and Dodogne rivers is 760 m^3/s (Allen & Castaing, 1973), but during the wet season, between November and May, discharge rates as high as 3000 m^3/s have been observed (Castaing & Allen, 1981). The discharge rate influences the salinity pattern and as a result the estuary ranges from partially mixed to well mixed.

The Garonne and Dordogne rivers input 2.5 to 3 million tons of suspended sediments into the estuary (Migniot, 1971) that produce a turbidity maximum zone (TMZ) with suspended sediment concentrations exceeding 10 g/L (Jalon-Rojas et al., 2015). The high discharge rate causes the TMZ to migrate from the upper reaches of the estuary during the dry season to the mid reaches of the estuary during the wet season (Jalon-Rojas et al., 2015). The sediment concentrations have caused navigation issues in the Gironde and as a result dredging is used to maintain a navigable main channel (see Figure 2.1) (www.bordeaux-port.fr).

Past studies on the Gironde have investigated sediment transport, turbidity, and axial flows, but most studies were done in the mid to upper reaches of the estuary. Ross et al.

(2019) analyzed vertical and temporal variations in mixing at the mouth of the Gironde, but with data collected during the low river discharge season.

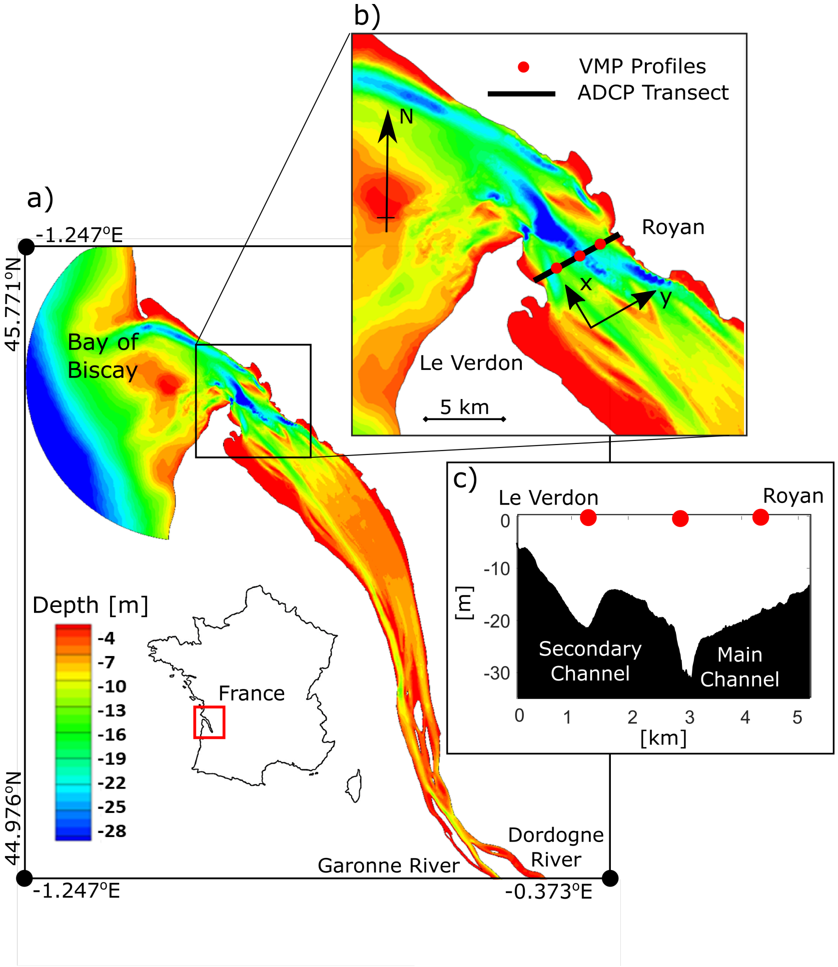

Figure 3.1. Study site bathymetry of the Gironde estuary. (a) The Gironde estuary. The location within France is boxed in red. The contours represent depth. (b) The close up of the study site, where x is along channel, positive seaward, and y is across channel, positive to the northeast. The ADCP transect is denoted by the black line and the VMP profile stations are denoted by the red dots. (c) The cross section of the transect displaying bathymetry, looking seaward, with the VMP profile stations denoted by the red dots. The secondary and main channel are labeled. The main channel can be seen in subplot (a) by the yellow contours (∼8 m depth) traveling from the mouth to the confluence of the two rivers, the Garonne and the Dordogne. The secondary channel exists only at the mouth.

3.4 Methods

3.4.1 Data Collection

Velocity, TKE dissipation, and salinity data were collected at the mouth of the Gironde (see Figure 2.1) on 3 February 2016 during maximum neap tide. On the data collection day the tidal range was 2 m and the combined river discharge was 921 m^3/s. A vessel-towed 600 kHz Teledyne RDI Workhorse Acoustic Doppler Current Profiler (ADCP) collected horizontal velocities throughout depth (axial and secondary flows) and bathymetric data. The data were collected for a full semidiurnal cycle (12.42 hr) in transects of ∼5 km wide, from Port Medoc in Le Verdon to Royan, that took ∼45 minutes each, for a total of 16 transects (see Figure 2.1). A Garmin GPS was used for navigation and the ADCP data were collected at 120 pings per ensemble in 50 cm vertical bins.

A SeaBird 19Plus Conductivity, Temperature, and Depth (CTD) profiler collected profiles of salinity and temperature at five stations across the estuary. The strength of the axial flow and insufficient weight on the CTD caused it to drift during casts. After extensive post-processing and comparison with salinity structures from other studies, the data were considered compromised with will not be used in this study. To provide salinity measurements a three-dimensional numerical model is utilized and will be discussed below.

Turbulent kinetic energy (TKE) dissipation data were collected by a Rockland Scientific Vertical Microstructure Profiler (VMP-250) at 1024 Hz at three stations across the estuary. The VMP measures orthogonal shear using two mounted shear probes as well as temperature. A weighted collar was utilized to ensure that the profiler remained as vertically aligned as possible and that the descent speed was ~ 1.5 m/s, which is the modified descent speed for tidal channel turbulence collection (Lueck, 2013). The appropriate descent speed was reached close to 2 m depth, limiting surface measurements. The VMP was lowered to ~ 16 m during each cast to avoid collisions with the bottom of the channel. At each station the VMP was cast three times, and during each cast two probes on the VMP collected velocity shear measurements for a total of two profiles per cast, or six profiles per station.

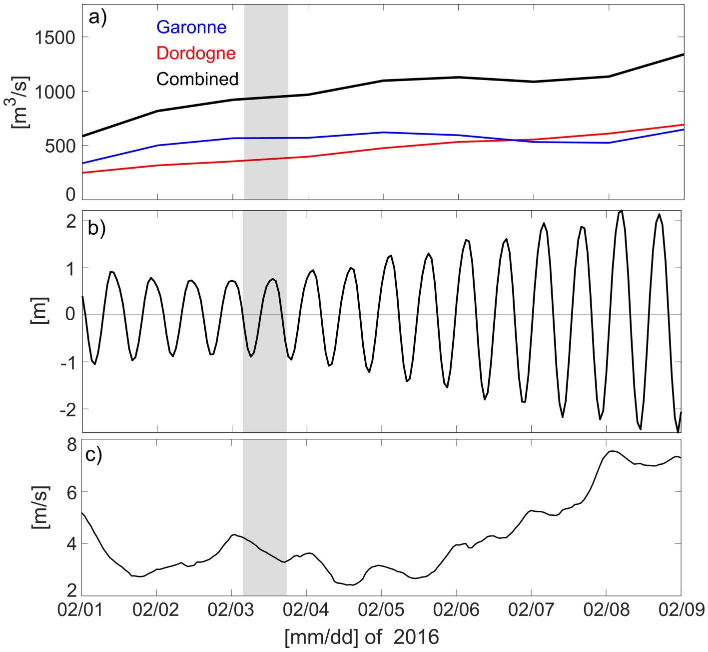

Figure 3.2. River discharge, water elevation, and wind. (a) River discharge from Garonne (blue line) and Dordogne (red line) Rivers, and their combined discharge (black line). (b) Water surface elevation, with respect to the mean water level. (c) Wind magnitude taken at Bordeaux airport. The highlighted sections represent the time period when data was collected and the complete time series represents the numerical model run.

The *in-situ* collected data were complimented by river discharge measurements from the Garonne and Dordogne rivers (Figure 3.2a) made available by French governmental agencies (data.eaufrance.fr). On the day of the field campaign, 3 February 2016, the combined river discharge was 921 m^3/s, which is higher than the annual average (760 m^3/s) but is considered low for the wet season. A tidal gauge station at the mouth of the Gironde collected tide heights (Figure 3.2b) and were made available by the Bordeaux Port Authority (GPMB). The tidal range on the field campaign day was ~2 m. Wind speed and direction (Figure 3.2c) was collected at Bordeaux Airport to provide a general sense of the regional wind conditions. Wind speeds were lower than 5 m/s during the collection period (~6h00 to 17h30 on 3 February 2016), but increased at the end of the day and exceeded 8 m/s between 18h00 and 23h30 (see Figure 3.2c).

3.4.2 Numerical Model

To attain salinity data, a 3D finite difference numerical model, SiAM3D (Brenon & Le Hir, 1999; Cugier & Le Hir, 2002) was used to simulate hydrodynamic conditions of the Gironde estuary. The model was implemented in the Gironde estuary by Sottolicho et al., (2001) and used in recent applications by Lajaunie-Salla et al. (2017), van Maanen and Sottolichio (2018), and Chambers et al., (submitted). Details on the governing equations and model assumptions can be found in Brenon and Le Hir (1999) and Cugier and Le Hir (2002). River discharge was imposed at the upstream limits of the Garonne and Dordogne rivers, and the tidal elevation, calculated from a 21-harmonic composition (Le Cann, 1990), was forced at the shelf. Lajaunie-Salla et al. (2017) and van Maanen and Sottolichio (2018) present the model validation using currents, tidal levels, and salinity.

The model was run from 1 February to 9 February 2016 and provided hourly salinity and sea surface elevation values.

3.4.3 Data Analysis

Analysis of horizontal velocities are presented first, along with the calculation of squared vertical shear. The salinity data provided by the numerical model will be presented next and includes the conversion from salinity to density, the calculation of stratification, and the calculation of squared buoyancy frequency. The calculations of the Richardson number, TKE dissipation, and vertical eddy viscosity will follow.

3.4.3.1 Horizontal Velocities and Shear

ADCP data that had a return signal of less than 90% good data or errors more than 10% of the maximum flow were excluded. To eliminate possible interference while the vessel was turning or stopped, data taken while the boat was traveling at speeds lower than 30 cm/s were also excluded. The data were further corrected using a comparison of the ADCP measured bottom track velocity and the velocity derived from the GPS data (Joyce, 1989). The corrected data were then interpolated onto a uniform grid of 500 distance points of 10.4 m and 74 depth points of 0.5 m. A regression analysis was used to rotate data to the primary local axis of the estuary (Thompson & Emery, 2014), with positive axial velocities traveling seaward and positive secondary velocities traveling towards the northeast bank. Bottom boundary data were collected for each transect and averaged to provide a bathymetric profile. Velocity data within 10% of the bottom were eliminated to exclude side lobe effects.

The coordinate system denotes x as the along-channel direction, where positive is out of the estuary, and the corresponding axial flows are denoted by u. The across channel direction is denoted by y, where positive is directed to the Royan bank (see Figure 3.1), and the corresponding secondary flows are denoted by v. The vertical direction is denoted by z and is positive up from the mean water level. The axial and secondary velocities are presented in Hovmoller plots where the velocities are depth averaged, denoted by $\overline{u}$ and $\overline{v}$, respectively.

Squared vertical axial and secondary shear were calculated using $\left(\partial u/\partial z\right)^2$ and $\left(\partial v/\partial z\right)^2$, respectively. Shear values $\partial u/\partial z$ and $\partial v/\partial z$ less than the noise limit for the ADCP, 0.04 cm/s, were excluded. The total squared vertical shear, S^2, was calculated by a summation of the squared vertical axial and secondary shear,

$$S^2 = \left\langle \frac{\partial u}{\partial z} \right\rangle^2 + \left\langle \frac{\partial v}{\partial z} \right\rangle^2 . \tag{3.1}$$

All shear are presented as depth averages, denoted by $\overline{\left(\partial u/\partial z\right)^2}$ for depth averaged squared axial shear, $\overline{\left(\partial v/\partial z\right)^2}$ for depth averaged squared secondary shear, and $\overline{S^2}$ for depth averaged total squared shear. The depth averaging was done after the calculation of the shears.

3.4.3.2 Density, Stratification, and Buoyancy Frequency

Density, ρ, was calculated using the salinity measurements from the numerical model and an assigned constant pressure, P, of 10.13 dbar and constant temperature, T, of 9. Depth-averaged density is denoted as $\overline{\rho}$.

Percent stratification, S, was calculated using the equation

$$S = \frac{\rho_2 - \rho_1}{\rho_2} \times 100\%, \tag{3.2}$$

where ρ_1 is the surface density and ρ_2 is the bottom density. Buoyancy frequency, N^2, was calculated and used as an additional measure of the vertical salinity gradient and is an input to the Richardson number, which will be discussed later. Squared buoyancy frequency, a characterization of the local density stratification, can be described as

$$N^2 = -\frac{g}{\rho_o}\frac{\partial \rho}{\partial z}, \tag{3.3}$$

where g is gravitational acceleration, rho_o is a reference density, and $\frac{\partial \rho}{\partial z}$ is the vertical density gradient (Thorpe, 2007). The depth-averaged squared buoyancy frequency is denoted $\overline{N^2}$.

3.4.3.3 Richardson Number

The Richardson number is a non dimensional ratio of squared buoyancy frequency to squared vertical shear,

$$Ri = \frac{N^2}{S^2} = \frac{\frac{g}{\rho_o}\frac{\partial \rho}{\partial z}}{\frac{\partial u}{\partial z}^2 + \frac{\partial v}{\partial z}^2}. \tag{3.4}$$

The Richardson number indicates if stratification is strong enough to inhibit mixing. Richardson numbers of 0.25 or higher indicate that stratification shuts down mixing, and Richardson numbers lower that 0.25 indicate that there is mixing in the water column (Miles, 1961; Galperin et al., 2007). The depth-averaged Richardson number is denoted by $\overline{Ri}$ with the averaging taking place after computation.

3.4.3.4 TKE Dissipation

The turbulent kinetic energy (TKE) equation describes the relationship between sources, sinks, transfers, and dissipation of TKE (Thorpe, 2007),

$$\frac{DE}{Dt} = T + P + B - \epsilon, \tag{3.5}$$

where $\frac{DE}{Dt}$ is the rate of change TKE, T is the transfer of TKE, P is the production of TKE, B is the buoyancy flux, and ϵ is dissipation. The transfer term T redistributes TKE, often through the breaking of surface waves and is typically neglected in the TKE balance for the consideration of internal energies (Craig and Banner, 1994; Davidson, 2015; Thorpe, 2007). The production term P represents the creation of TKE by the mean flow, and is a function of the mean shear (Thorpe, 2007). The buoyancy flux B is representative of the potential energy and is a function of the squared buoyancy frequency and diffusivity. It has the ability to increase TKE if there are instabilities in the water column and the buoyancy frequency is negative, providing the system with potential energy, and also has the ability to decrease TKE if the water column is stable and therefore provides no potential energy to the system (Thorpe, 2007). The final term in the TKE equation is ϵ, the rate of kinetic energy dissipation, which is the rate of loss of TKE through viscous effects, and works by transferring TKE to heat (Thorpe, 2007).

The TKE equation can be simplified by assuming that production, buoyancy flux, and dissipation are the dominant terms in the TKE equation (Thorpe, 2007), and by assuming steady state conditions where there is no net gain or loss of TKE with time. The simplified TKE equation is

$$0 = P + B - \epsilon, \tag{3.6}$$

indicating that ϵ is equal to the sum of the production and buoyancy flux. If the system is well mixed and there is little to no stratification, the buoyancy flux term becomes negligible and ϵ is equal to the production rate. If buoyancy flux cannot be considered negligible, ϵ is calculated from the spacial gradients of the velocity components and can be defined as

$$\epsilon = 2\nu S_{ij} S_{ij}, \tag{3.7}$$

where ν is the kinematic viscosity of a fluid, which is a function of the dynamic viscosity and the mass density of the fluid, and S_{ij} is the strain rate tensor, described as $0.5(\partial u_i/\partial x_j + \partial u_j/\partial x_i)$ which can be approximated by $0.5(\partial u/\partial y + \partial v/\partial x)$ and physically describes the rate of change of deformation of a fluid (Davidson, 2015; Thorpe, 2007).

As mentioned before, the VMP measures shear in two orthogonal directions and calculates dissipation assuming isotropic turbulence, thus simplifying the TKE dissipation equation to

$$\epsilon = 7.5\nu \left\langle \frac{\partial u}{\partial z} \right\rangle^2 . \tag{3.8}$$

The VMP data were processed using Matlab by eliminating anomalies and providing an extended bootstrapped data set (Figure 3.3). As mentioned above, at each station the VMP was cast three times. During those casts the two shear probes collected shear profiles for a total of 6 profiles per station. The VMP was weighted to keep the instrument as vertically aligned as possible, and profiles that had more than a 5% inclination rate were excluded. The profiles were interpolated onto the same depth grid for uniformity and ease of computation. To eliminate outlier data, the maximum and minimum measurements at each station were isolated, and if the ratio of maximum to minimum was greater than 2, the maximum value was excluded and a new ratio with the new maximum measurement was tested. Once the ratio was less than 2, the remaining good profiles, ~88% of the data, were averaged together to create one profile per station with time (personal communication with Rockland Scientific). Next, the data was resampled using a bootstrapping method that provided 6000 samples to narrow the confidence interval (Efron and Gong, 1983; Ross et al, 2019). The processed TKE dissipation, denoted by ϵ, varied with time and depth at

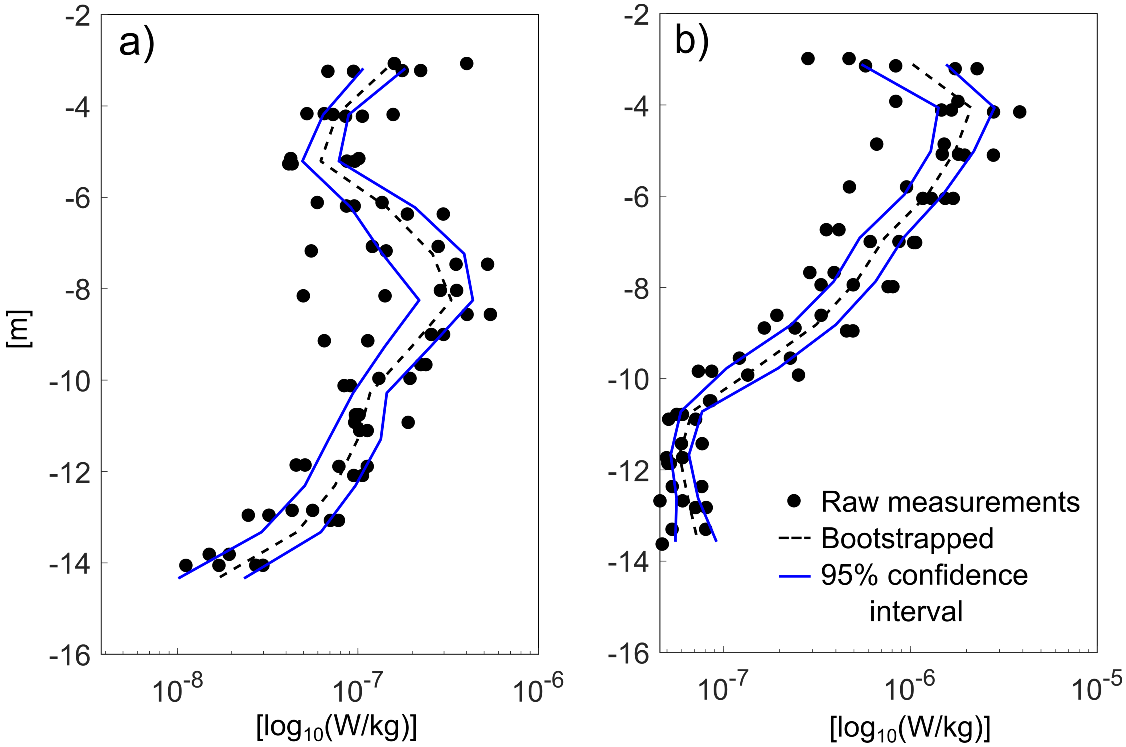

Figure 3.3. Bootstrapped TKE dissipation. (a,b) Examples of TKE dissipation dissipation rate (black dotted line) after bootstrapping the raw measurements (black dots). The blue lines indicate 95% confidence intervals.

the three sampling stations. For analysis it was depth averaged, denoted by $\bar{\epsilon}$, and interpolated over time (from 12 data points to 16 data points) to allow for uniformity when calculating the vertical eddy viscosity, which will be discussed next.

3.4.4 Eddy Viscosity

The turbulent mixing of momentum is quantified by eddy viscosity, specifically the vertical eddy viscosity, A_z, which is often dominant compared to horizontal eddy viscosity (Monismith, 2010), and is defined as

$$A_z = \Gamma_m \frac{\epsilon}{S^2}, \tag{3.9}$$

where Γ_m is the mixing efficiency of momentum (Kay and Jay, 2003; Huguenard et al., 2015). The mixing efficiency is dependent on the flux Richardson number, Rf, and is quantified as

$$\Gamma_m = \frac{1}{1 - Rf}. \tag{3.10}$$

The flux Richardson number is the amount of kinetic energy generated by shear converted from buoyancy to potential energy (Ross et al., 2019) and represents a buoyancy to production kinetic energy ratio (Huguenard et al., 2015; Ross et al., 2019),

$$Rf = \frac{Ri}{Pr}. \tag{3.11}$$

The forced maximum Rf is ∼0.2 since at higher values steady state is not maintained and the simplified TKE equation does not hold (Dunckley et al., 2012; Thorpe, 2007). In the Rf equation buoyancy is represented by the Richardson number, Ri, and production is represented by the Prandtl number, Pr. The Prandtl number, quantified as

$$Pr = (1 + 4.47Ri)^{0.5}, \tag{3.12}$$

is a non-dimensional number that is a function of the Richardson number (Tjernstrom, 1993; Huguenard et al., 2015) and compares diffusion of salt and momentum (Ross et al., 2019). Through quantification of the Prandtl number, Richardson number, and flux Richardson number, the mixing efficiency can be determined. Through this process Az is indirectly proportional to the Richardson number, and is expected to be higher at lower Richardson numbers. When Richardson numbers are close to or exceeding the critical Richardson number, 0.25, mixing is reduced as a result of increased stratification (Galperin et al., 2007; Miles, 1961). Additionally, Az is directly proportional to the ratio of ϵ to S^2, or the dissipation to production of TKE (Monismith, 2010). This means that mixing is elevated when a higher proportion of the energy created is destroyed.

To investigate the temporal and spacial variations in mixing, the mechanisms that influence mixing are quantified in order to demonstrate a more complete analysis of what causes these temporal and cross channel variations.

3.5 Results

Intratidal current velocities and TKE dissipation data collected at the mouth of the Gironde estuary on 3 February 2016 are presented alongside density data provided by the numerical model simulation. These data are used to quantify the influencing mechanisms of mixing. Intratidal flows and squared vertical shear show temporal variability and variation with cross channel distance, with squared vertical shear displaying distinct correlation with bathymetric changes. Density and stratification show intratidal and cross channel variability, but do not exhibit interactions with cross channel bathymetric changes. Similar to squared vertical shear, the buoyancy frequency shows intratidal and cross channel variability with dependency on bathymetry, and the ratio of the two create a time varying Richardson number that is sensitive to bathymetric changes. The TKE dissipation exhibits temporal and cross channel variations, and despite the limited cross channel resolution a connection to bathymetry can still be made. The vertical eddy viscosity reflects the time and cross channel variation of the influencing mechanisms of mixing and displays a strong correlation with TKE dissipation and squared vertical shear. In addition, a link to secondary influencing mechanisms is also present, with peaks in axial flows during peaks in mixing. Again, the limited cross channel resolution limits the extent to which a dependency on bathymetry can be identified, however the combination of cross channel variations in influencing mechanisms of mixing provides a general depth-dependency in mixing.

3.5.1 Intratidal Flows

Depth averaged intratidal flows (axial and secondary) are examined for variability with time and cross channel distance. Axial velocities are greater than secondary velocities, with secondary velocities on average $\sim 28\%$ of the axial velocities. Previous studies at the mouth of the Gironde have shown that Coriolis, curvature, and a lateral baroclinic pressure gradient influence axial flows and drive secondary flows (Chambers et al., submitted). Peak axial flows have been linked to elevated mixing on a temporal scale (Ralston & Stacey,

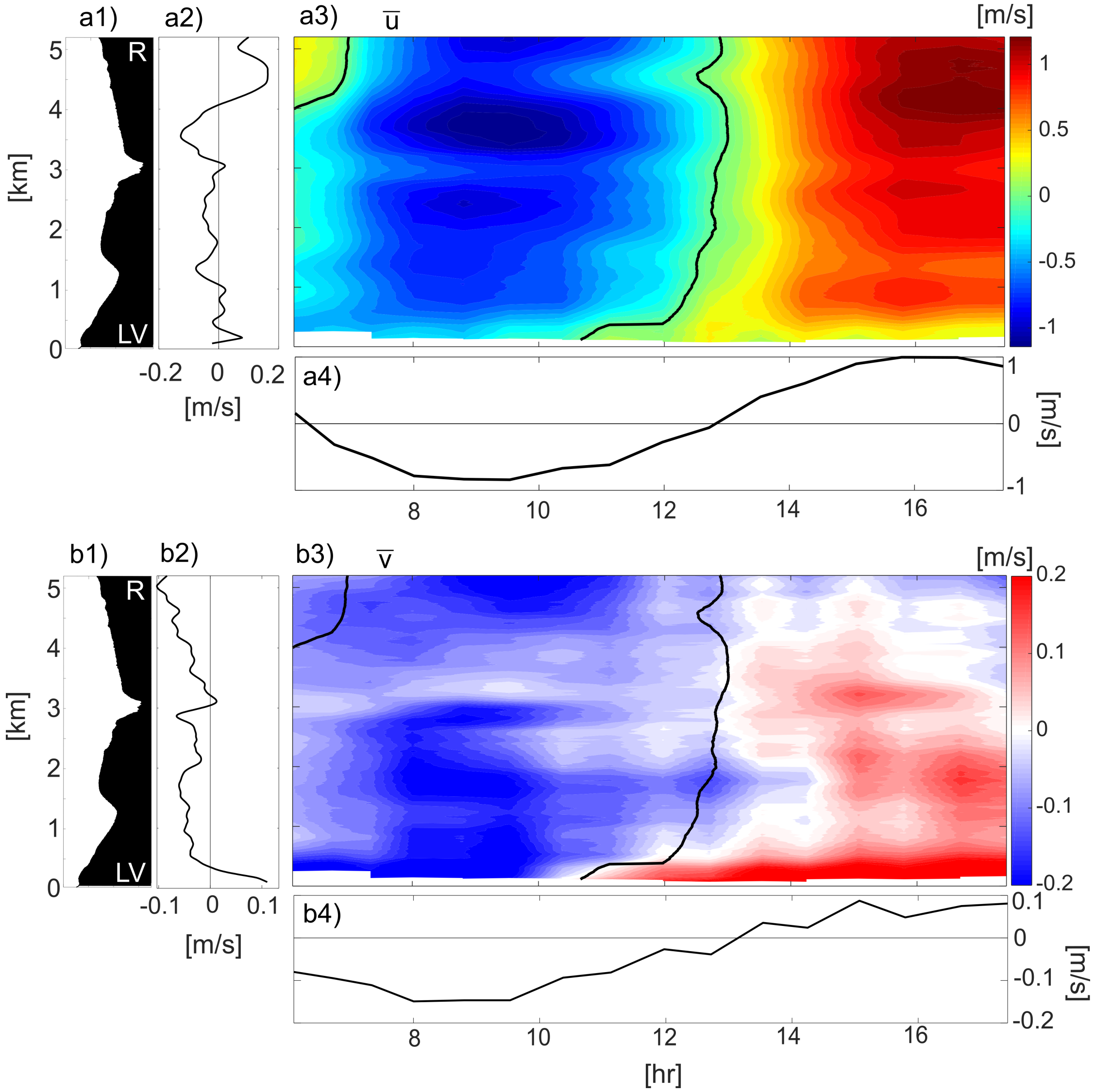

Figure 3.4. Intratidal flow variation with time and cross channel distance. (a1,b1) The bathymetry with the Royan bank is indicated by 'R' at 5 km across and the Le Verdon bank is indicated by 'LV' at 0 km across. (a2, b2) Depth and time averaged axial and secondary flows, respectively. (a3,b3) Depth averaged axial and secondary flows, respectively, varying with time (x-axis) and distance across the estuary (y-axis). (a4,b4) Depth and distance averaged axial and secondary flows, respectively. Positive axial flows are traveling seaward and positive secondary flows are traveling towards the Royan bank. The black lines on the contour indicates the time of axial flow slack tide, with flood tide from 6h00 to 12h00 and ebb tide from 12h30 to 17h30.

2006; Rippeth et al., 2001, 2002; Wiles et al., 2006), but there have been no links between cross channel variability in peak flows and cross channel variability in mixing.

3.5.1.1 Axial Flows

During flood tide, depth averaged axial flows $\overline{u}$ reach a maximum, ~1.1 m/s, between 3 and 4 km across the estuary from 8h00 to 10h00 (Figure 3.4a3). The location of maximum flows changes during ebb tide, where $\overline{u}$ reach a maximum, ~1.6 m/s, between 4 and 5 km across estuary from 16h00 to 17h30. Chambers et al. (submitted) recently showed with the same data set that maximum axial flows migrate from over the main channel during ebb tide (~3 to 4 km across) to over the Royan shoal during flood tide (~4 to 5 km across) (Figure 3.4a1,a3) due to intratidal variations in Coriolis and curvature forcing. On a temporal scale, mixing is expected to be elevated during maximum flood (~9h00) and maximum ebb (~16h30)(Ralston & Stacey, 2006; Rippeth et al., 2001, 2002; Wiles et al., 2006), and if this theory extends to cross channel variability, elevated mixing is also expected to migrate along with axial flows.

At slack after flood there is a phase lag across the estuary where $\overline{u}$ at 0 km across switch to ebb first, at ~10h45, and $\overline{u}$ between 2 and 4 km across switch to ebb ~1.5 hours later, at ~13h00 (Figure 3.4a3). Slack after ebb experiences a phase lag across the estuary as well, and is indicated by $\overline{u}$ transitioning from ebb to flood between 4 and 5 km at 6h00 to 7h00 while flows between 0 and 4 km have already started flooding. A least squares fit of $\overline{u}$ shows a phase lag of > 1 hr between the flows at 0 km across and 5 km across. This phase lag was examined by Chambers et al. (submitted) and was attributed to differences in flow magnitude between the shoals and the main channel, with the weakest flows switching direction first and the strongest flows switching last. A time-average of $\overline{u}$ shows this variability in flow magnitude across the estuary.

The time averaged $\overline{u}$ (Figure 3.4a2) illustrates the lateral movement of peak flows between flood (3 to 4 km across) and ebb (4 to 5 km across). In addition, the time average reveals that flows on the Le Verdon side are primarily directed landward, and over the secondary channel, between 1 and 1.5 km, a local maxima of -0.07 m/s is seen. During flood Coriolis forcing works against curvature forcing, distributing elevated flows across the estuary. During flood Coriolis and curvature work together and create a ‘pile up’ of axial flows on the Royan side, as described in Chambers et al. (submitted). This difference in axial flow distribution creates a time averaged $\overline{u}$ that shows stronger ebb velocities but a wider distribution of flood velocities.

To get a better visual of how $\overline{u}$ changes with time, a distance average is taken (Figure 3.4a4). Distance averaged $\overline{u}$ show a weaker flood tide maximum, $\sim$ -0.8 m/s at 9h00, than ebb tide maximum, $\sim$1 m/s at 16h00. A calculation of the M_4 velocity phase relative to the M_2 velocity phase affirms that there is ebb dominance at the mouth (Friedrichs & Aubrey, 1988). This ebb dominance is unique to the mouth of the estuary, as previous studies conducted in the mid to lower reaches of the Gironde show flood dominance (Ross et al., 2017), suggesting that hydrodynamic processes at the mouth differ from those found upstream.

Secondary flows are investigated next to determine their relationship to axial flows and to identify cross channel and temporal variability.

3.5.1.2 Secondary Flows

During flood tide depth averaged secondary flows, $\overline{v}$, are directed towards the Le Verdon bank (Figure 3.4b3), the result of a lateral circulation pattern driven by the lateral baroclinic pressure gradient (Chambers et al., submitted). Maximum flood values of $\overline{v}$ ($\sim$ -0.2 m/s) are located between 0 and 3 km, and again between 4.5 and 5 km across the estuary from 8h00 to 10h00. About 0.5 h after slack after flood, $\overline{v}$ is directed towards the Royan bank. The switch in secondary flow direction aligns with the phase lag in slack tide across the estuary, with $\overline{v}$ near the Le Verdon bank switching first. Secondary flows near Royan, between 4.5 and 5 km across, do not switch direction and continue to travel towards the Le Verdon bank. This is explained in Chambers et al. (submitted) by a water level set-up on the Royan side of the estuary that drives secondary flows towards Le Verdon.

Secondary flows directed towards Royan during ebb show flows > 0.2 m/s over the shoal near Le Verdon between 13h00 and 17h30 and a minimum, near zero, between 4 and 5 km. For both flood and ebb $\overline{v}$, the strongest flows align with the strongest $\overline{u}$ with relation to time (see Figures 3.4a4,b4) but not distance across the cross section. At the location of the strongest $\overline{u}$ (3 to 4 km across during flood, 4 to 5 km across during ebb, see Figure 3.4a3), weaker $\overline{v}$ are found ($<$ -0.1 m/s during flood, $<$ 0.05 m/s during ebb, see Figure 3.4b3). This is because stronger axial flows at these locations drive a vertical circulation pattern (seen in Chambers et al., submitted) that, when depth averaged, produces near-zero secondary flows.

Over the main channel, at 3 km across, there is an abrupt change in magnitude ($\sim$0.07 m/s in $<$0.25 km) of secondary flows which is attributed to the sharp change in bathymetry at that location (see Figure 3.1c) and is considered to be outside the scope of this study and will not be discussed. Time averaged $\overline{v}$ from 0.5 to 3 km across show flows directed towards Le Verdon, a result of stronger $\overline{v}$ during flood tide (see Figure 3.4b1). Closer to the Le Verdon bank, between 0 and 0.5 km across, strong $\overline{v}$ (> 0.2 m/s) during ebb tide (see Figure 3.4b1) dominate over the weaker $\overline{v}$ during flood tide and drive time averaged $\overline{v}$ towards the Royan bank (Figure 3.4b2).

Additionally, there is a correlation between changes in depth across the estuary and local maxima in $\overline{v}$. There are four local maxima in the time average $\overline{v}$, at 0 km, 1.75 km, 2.75 km, and 5 km. The local maxima at 2.75 km across is attributed to the sharp change in bathymetry over the main channel, as previously discussed, and is not considered. The other three maxima occur at shallow parts in the cross section where surface secondary flows observed by Chambers et al. (submitted) are not balanced by the return flow, and therefore the depth average of secondary flows appears stronger than their counterparts over the channel.

Both axial flows and secondary flows (a more in depth analysis of secondary flows and their forcing mechanisms is found in Chambers et al. (submitted)) exhibit variation with time and cross channel distance. Squared vertical shear will now be investigated to determine if these variabilities are sustained.

3.5.2 Squared Vertical Shear

Squared vertical shear represents the vertical changes in velocity magnitude throughout the water column, and is therefore expected to show a connection to bathymetric changes (French & Clifford, 1992; Traynum & Styles, 2007). With respect to time, shear is expected to be decreased during flood when tidal flows and river discharge oppose each other (Peters, 1999; Whitney et al., 2012). The total squared vertical shear (Figure 3.5c) is a summation of the squared axial and secondary vertical shear (Figure 3.5a and b, respectively) and therefore depicts whether the axial or lateral shear dominates the total squared vertical shear.

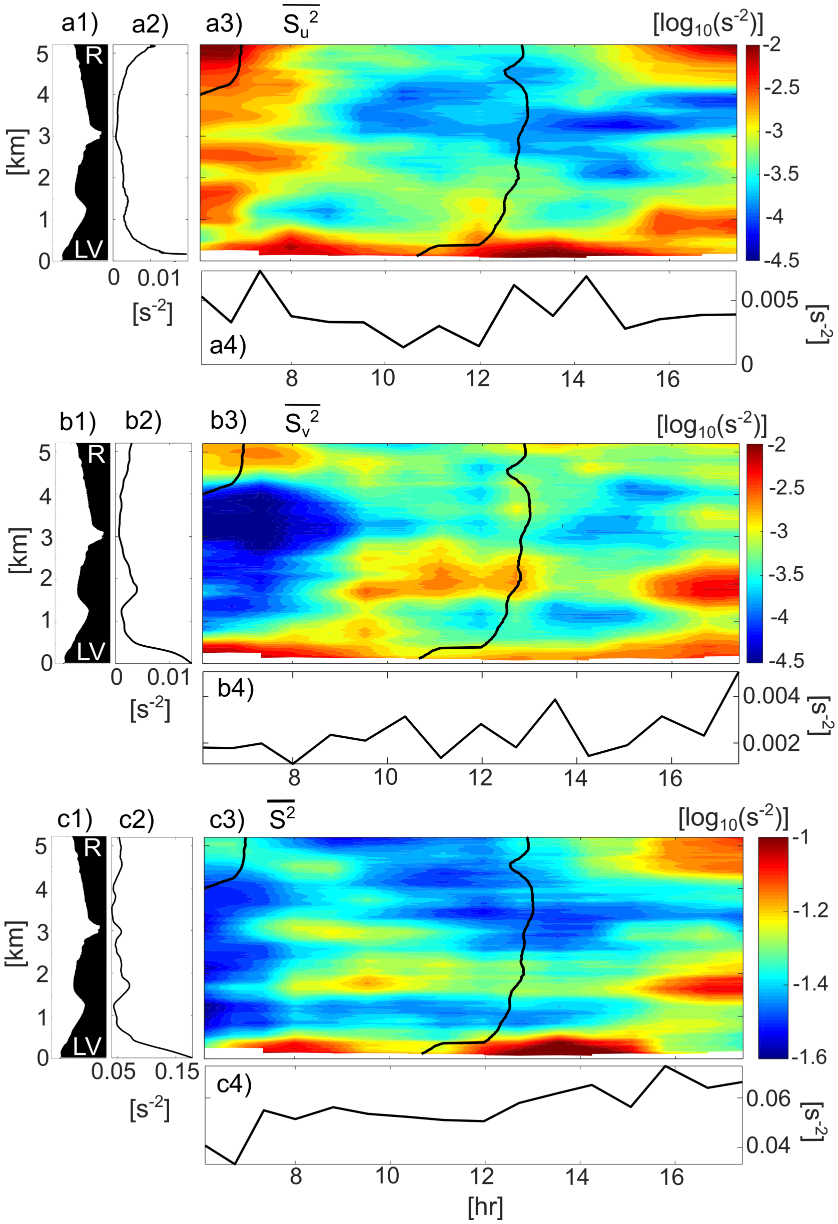

Figure 3.5. Squared vertical shear with time and cross channel distance. (a1,b1,c1) The bathymetry with the Royan bank is indicated by ‘R’ at 5 km across and the Le Verdon bank is indicated by ‘LV’ at 0 km across. (a2,b2,c2) Depth and time averaged squared vertical axial, secondary, and total shear, respectively, plotted on a non log scale. (a3,b3,c3) Depth averaged squared vertical axial, secondary, and total shear, respectively, varying with time (x-axis) and distance across the estuary (y-axis) plotted on a log 10 scale. (a4, b4,c4) Depth and distance averaged squared vertical axial, secondary, and total shear, respectively, plotted on a non log scale. The black lines on the contour indicates the time of axial flow slack tide, with flood tide from 6h00 to 12h00 and ebb tide from 12h30 to 17h30.

Depth averaged squared vertical axial shear, denoted by $\overline{S_u^2}$, shows variation with both time and distance across the estuary (Figure 3.5a). During slack after ebb $\overline{S_u^2}$ is largest (Figure 3.5a3) and a distance average reveals that $\overline{S_u^2}$ is maximum during slack tides (Figure 3.5a4). On the Le Verdon side of the estuary, during late ebb between 0 and 0.5 km across, and on the Royan side of the estuary, between 4.5 and 5 km across, elevated $\overline{S_u^2}$ ($> 10^{-2.75}$ s^{-2}) is found (Figure 3.5a3). These maxima are seen in the time averaged $\overline{S_u^2}$ (Figure 3.5a2) and occur over the shoals.

The depth averaged squared vertical secondary shear (Figure 3.5b3), $\overline{S_v^2}$, reveals maxima ($> 10^{-2.5}$) along the Le Verdon side of the cross section, between 0 and 0.5 km, throughout the tidal cycle as well as during slack after ebb (7h00) on the Royan side of the cross section between 4.5 and 5 km. Additional maxima exist between 1.5 and 2 km across from 9h00 to 12h00 and 16h00 to 17h30. These maxima align with the location of the shoals and channel division (Figure 3.5b2), demonstrating a link between elevated $\overline{S_v^2}$ and bathymetric changes. Additionally, temporal variations in $\overline{S_v^2}$ show increases from flood to ebb, with maximum $\overline{S_v^2}$ at the end of ebb (Figure 3.5b4), supporting the typical flood-ebb shear asymmetry (Geyer et al., 2000; Stacey et al., 1999; Whitney et al., 2012).

Total vertical squared shear exhibits both variability with time and distance across the estuary. Maximum squared vertical shear ($\overline{S^2} > 10^{-1}$ s^{-2}) is located near the Le Verdon bank, between 0 and 0.5 km across, during slack after flood (12h00 to 15h00, Figure 3.5c3). This is a direct result of elevated $\overline{S_u^2}$ at the same location and time (Figure 3.5a3). Other local maxima, $>10^{-1.2}$ s^{-2}, are seen towards the end of ebb tide (16h00 and 17h30) at 1.75 and 5 km across the estuary as well as during flood tide (from 7h00 to 9h00) at the Le Verdon bank (0 to 0.5 km across). These maxima are all located at shallow regions in the bathymetry and can be seen in the time average $\overline{S^2}$ (Figure 3.5c2). This reflects the cross channel patterns for axial and secondary shear, where at shallow depths elevated shear is found. Similar observations were seen in a study by Huguenard et al. (2015), where increased squared vertical shear was observed over the shoals in a partially mixed microtidal estuary.

A distance average $\overline{S^2}$ demonstrates the temporal variation in total shear (Figure 3.5c4). There is an increase in shear from flood to ebb (Figure 3.5b4), consistent with findings from Peters (1999) and Whitney et al. (2012) who attributed this increase in shear during ebb to tidal straining and gravitational circulation. Several studies have confirmed a direct relationship between increases in shear and increases in mixing (Geyer et al., 2008; Prandle, 2009; Stacey et al., 2011; Turner 1973) and therefore elevated mixing over the shoals and channel division are expected, as well as a increased mixing during ebb tide. On the other hand, stratification is known to inhibit mixing (Stacey et al., 2011; Turner, 1973) and could oppose elevated shear, subsequently suppressing mixing. An analysis of density, stratification, and the squared buoyancy frequency is presented next to explore this possibility.

3.5.3 Density, Stratification, and Squared Buoyancy Frequency

The density regime in an estuary influences mixing (Scully and Geyer, 2012) and is typically characterized by increased stratification during ebb tides and decreased stratification during flood tides as a result of along-channel straining of the density field (Scully & Geyer, 2012; Simpson et al., 1990). Many studies have found that this flood-ebb stratification pattern induces tidal asymmetries in mixing (Geyer et al., 2000; Jay & Smith; 1990; Nepf & Geyer, 1996; Simpson et al., 2005; Stacey et al., 1999; Stacey & Ralston, 2005). To investigate this in the Gironde, the depth averaged density, $\overline{\rho}$, stratification, S, and squared buoyancy frequency, $\overline{N^2}$, are displayed to analyze variability with time and distance across the estuary.

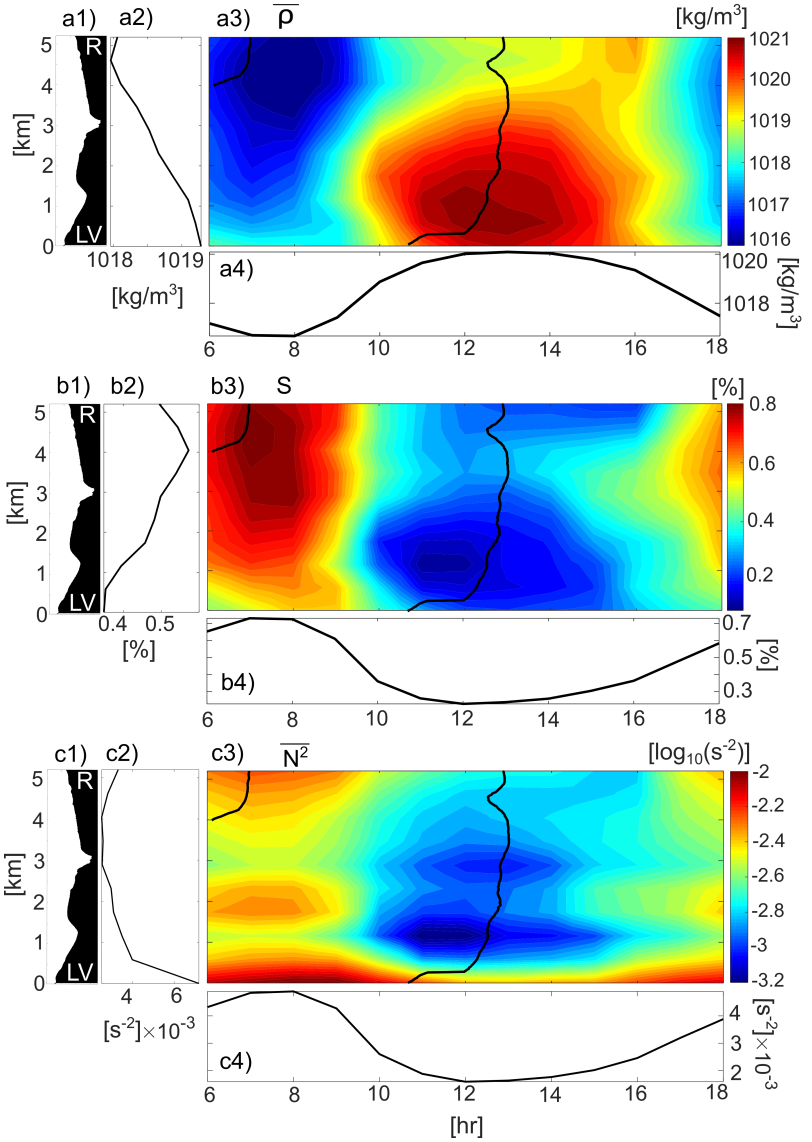

Figure 3.6. Density, stratification, and squared buoyancy frequency with time and cross channel distance. (a1,b1,c1) The bathymetry with the Royan bank is indicated by 'R' at 5 km across and the Le Verdon bank is indicated by 'LV' at 0 km across. (a2,b2,c2) Depth and time averaged density, stratification, and buoyancy flux, respectively. (a3,b3,c3) Depth averaged density, stratification, and buoyancy flux, respectively, varying with time (x-axis) and distance across the estuary (y-axis). (a4,b4,c4) Depth and distance averaged density, stratification, and buoyancy flux, respectively. Buoyancy flux is plotted on a log 10 scale in plot (a3), and for plots (a2,a4) is plotted on a non log scale. The black lines on the contour indicates the time of axial flow slack tide, with flood tide from 6h00 to 12h00 and ebb tide from 12h30 to 17h30.

Depth averaged density, $\overline{\rho}$, shows a maximum of 1021 kg/m^3 over the secondary channel between 0.5 and 1.5 km from 11h30 to 13h00, during slack after flood (Figure 3.6a3). The minimum $\overline{\rho}$ occurs during early flood tide, from 7h00 to 8h30, between 4 and 5 km across. The switch in location across the estuary drives time averaged cross channel variations, seen in the time averaged $\overline{\rho}$ in Figure 3.6a2. The resulting lateral pattern shows a maximum $\overline{\rho}$ of 1019 kg/m^3 at 0 km across and a minimum $\overline{\rho}$ of 1018 kg/m^3 at 4.5 km across. While the time averaged $\overline{\rho}$ shows variations across the estuary, these variations do not coincide with bathymetric changes, indicating that density is not responsive to bathymetric changes. The temporal variation in density is a result of tidal straining, which is the interaction between longitudinal density gradients and vertical tidal shear (Scully & Friedrichs, 2007; Simpson et al., 1990) and is expected to translate into higher stratification during ebb tide and lower stratification during flood tide.

Stratification, S, provides a measure of the vertical change in density. The maximum S, 0.8%, occurs during early flood, just after slack after ebb (7h00 to 8h00) near the Royan bank, between 4 and 5 km (Figure 3.6b3). The minimum S occurs during late ebb over the secondary channel, from 11h00 to 12h00 between 1 and 1.5 km across. The time averaged S shows maximum stratification of ∼0.6% located over the channel slope near Royan at 4 km across (Figure 3.6b2). This is the location of the maximum axial flows during ebb tide (Figure 3.4a3) which are generally more stratified than flood tide. The time averaged S decreases to 0.4% at the Le Verdon bank, showing variability with distance but no reliance on bathymetry. The distance averaged S shows variability over the tidal cycle, with decreasing S over flood tide and increasing S over ebb tide (Figure 3.6b4), a pattern typical of tidal straining (Scully & Friedrichs, 2007; Simpson et al., 1990). Another way to quantify vertical changes in density is with the squared buoyancy frequency, which is dependent on depth, suggesting that it will also be dependent on bathymetry.

Depth averaged squared buoyancy frequency, $\overline{N^2}$, exhibits a maximum (10^{-2} s^{-2}) during early flood tide (7h00 to 8h00) at 0 km across. There are other local maxima at 0 km across from 16h00 to 18h00 and from 6h00 to 8h00 at 2 km and 5 km across. This pattern is very similar to squared axial shear, where maxima exist near Le Verdon and during early flood tide (see FIgure 3.5a3). These maxima also coordinate with bathymetry, with maxima during early flood located near the two shoals and over the channel division, the three shallowest parts of the cross section. This is opposite of findings from studies like Scully and Friedrichs (2007) where density stratification ($\partial\rho/\partial z$) is greater over the channel than the shoal. This difference in spacial distribution of density stratification could be due to the elevated lateral baroclinic pressure gradient and secondary flows, seen in Chambers et al. (submitted) which may be shifting denser water up the channel slopes, therefore tilting the isopycnals and creating vertical density gradients on channel slopes and shoals.

The time averaged $\overline{N^2}$ further demonstrates the interaction with bathymetry (see Figure 3.6c2), where there are maxima over the two shoals, at 0 and 5 km with $\overline{N^2}$ values of 0.007 and 0.0035 s^{-2} respectively. The local maxima over the channel division, seen in Figure 3.6c1 from 6h00 to 8h00, is not obvious in the time averaged plot (Figure 3.6c2). This is most likely due to the decrease in $\overline{N^2}$ during late ebb between 0.5 and 4 km across that cancels out the local maxima over the channel division when a time average is taken.

The distance averaged $\overline{N^2}$ decreases over flood tide and increases over ebb tide (Figure 3.6c3), the same temporal variation that S shows in Figure 3.6b3 (Figure 3.6b3). This temporal pattern is typical of strain-induced periodic stratification (SIPS) and is common in estuaries with moderate to low mixing levels (Jay & Musiak; Peters, 1999; Simpson et al., 1990). The cross channel and temporal variations in $\overline{S^2}$ and $\overline{N^2}$ are expected to appear in the Richardson number, which is a ratio of $\overline{N^2}$ to $\overline{S^2}$. A comparison of the magnitudes of shear ($10^{-1.6}$ to 10^{-1} s^{-2}) and buoyancy frequency ($10^{-3.2}$ to 10^{-2} s^{-2}) predicts that shear will dominate over buoyancy frequency and create a Richardson number that promotes mixing.

3.5.4 Richardson Number

The Richardson number, Ri, determines whether stratification is large enough to inhibit mixing. Richardson numbers of 0.25 ($\log_{10}(0.25) = 10^{-0.6}$) or greater indicate that stratification is significant enough to inhibit mixing (Miles, 1961; Galperin et al., 2007).

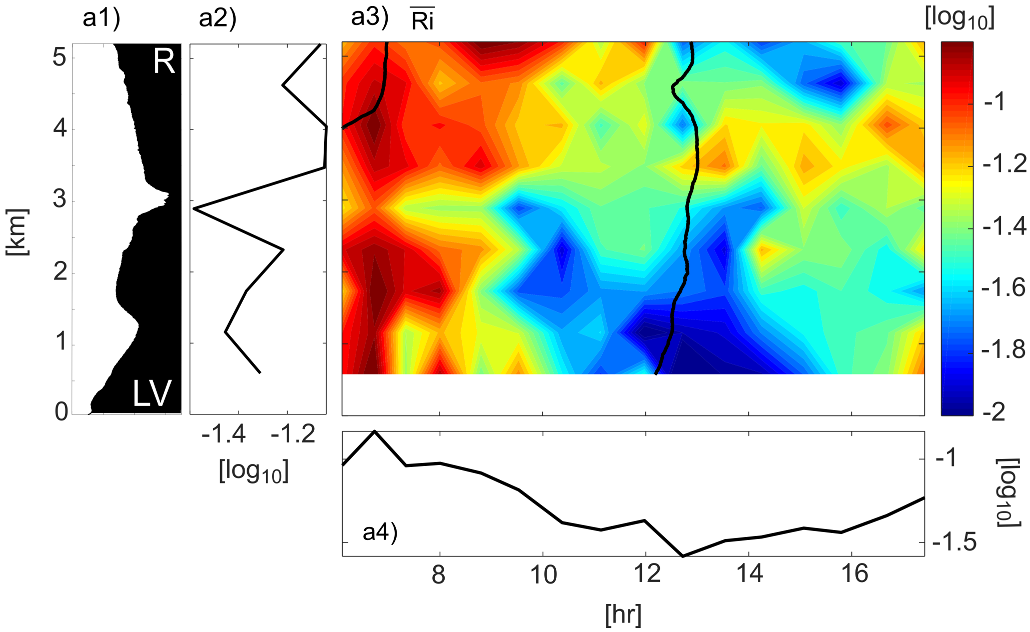

Figure 3.7. Richardson number with time and cross channel distance. (a1) The bathymetry is shown with the Royan bank is indicated by 'R' at 5 km across and the Le Verdon bank is indicated by 'LV' at 0 km across. (a2) Depth and time averaged Richardson number. (a3) Depth averaged Richardson number, varying with time (x-axis) and distance across the estuary (y-axis). (a4) Depth and distance averaged Richardson number. All subplots are plotted on a log scale. The black lines on the contour indicates the time of axial flow slack tide, with flood tide from 6h00 to 12h00 and ebb tide from 12h30 to 17h30.

The depth averaged Richardson number, $\overline{Ri}$, is below the critical limit of 0.25 ($10^{-0.6}$) for all times and distances across the estuary (Figure 3.7a1), signifying that the water column is never stratified enough to shut down mixing (Miles, 1961; Galperin et al., 2007). Elevated $\overline{Ri}$, $>10^{-1}$, occurs during early flood (between 6h00 and 8h00) across the estuary. The heightened $\overline{Ri}$ is a result of elevated $\overline{N^2}$ (Figure 3.6c1) and decreased $\overline{S^2}$(Figure 3.5c1) during early flood. Minimum values of $\overline{Ri}$, 10^{-2}, occur near the Le Verdon bank (0.5 and 1.5 km) during slack after flood (12h00 to 14h00), and at this location mixing is expected to be enhanced.

A time average of $\overline{Ri}$ confirms that there is not only variation with distance across the estuary but there is dependency on bathymetry. The time dependency of the $\overline{Ri}$ corresponds to the time dependency of $\overline{N^2}$. During flood $\overline{Ri}$ decreases, reaching a minimum of $10^{-1.4}$ at slack after flood. During ebb $\overline{Ri}$ increases, reaching a maximum at slack after ebb of $10^{-0.8}$. The distance averaged $\overline{N^2}$ follows this same pattern with decreasing values over flood and increasing values over ebb, indicating mixing should be elevated more so during ebb tide than flood in this macrotidal estuary. The final influencing mechanism of mixing, the TKE dissipation rate, will now be examined.

3.5.5 TKE Dissipation

The depth averaged TKE dissipation rate, $\overline{\epsilon}$, is the rate at which energy is lost through viscous effects and is proportional to the amount of mixing in a system (Monismith, 2010; Thorpe, 2007). TKE dissipation was collected at three locations across the estuary, and while general observations can be made about the variation of $\overline{\epsilon}$ with distance, the data resolution is not fine enough to resolve dependency on bathymetry, other than making general connections.

Depth averaged TKE dissipation, $\overline{\epsilon}$, reaches a maximum ($10^{-5.6}$ W/kg) at mid ebb tide (16h00 to 16h30) over the main channel (3 km across estuary) and a minimum ($10^{-6.8}$ W/kg) during early flood (7h00 to 8h00) and at slack after ebb (12h30) from 1.5 to 3 km and at 3 km across, respectively (Figure 3.8a1). At 4 km across estuary the time average value of $\overline{\epsilon}$ is $10^{-5.9}$ W/kg, which is larger than at the other two stations ($\sim 10^{-6}$ at 3 km and $10^{-6.3}$ at 1.5 km; Figure 3.8). There is an increase in $\overline{\epsilon}$ from the Le Verdon side to the Royan side of the estuary. The distance averaged $\overline{\epsilon}$ shows a slight increase from flood to ebb tide with lowest values, $10^{-6.5}$ W/kg, occurring during early flood, corresponding well with the elevated values of N^2. There is an increase over flood tide, and at slack after flood a dip in $\overline{\epsilon}$ around 13h00 and then values fluctuate up and down for the remainder of ebb tide.

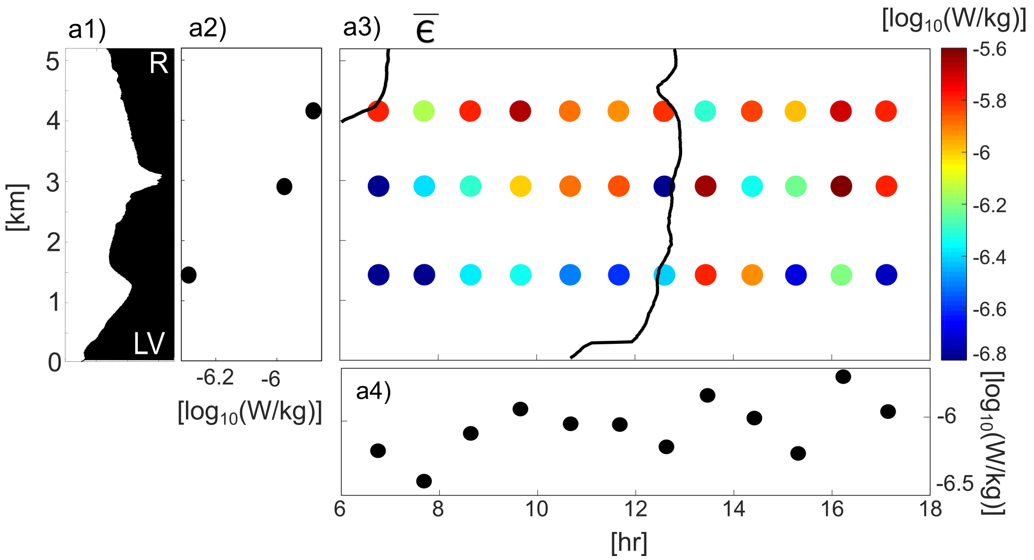

Figure 3.8. TKE dissipation with time and cross channel distance. (a1) The bathymetry with the Royan bank is indicated by ‘R’ at 5 km across and the Le Verdon bank is indicated by ‘LV’ at 0 km across. (a2) Depth and time averaged TKE dissipation. (a3) Depth averaged TKE dissipation, varying with time (x-axis) and distance across the estuary (y-axis). (a4) Depth and distance averaged TKE dissipation. All subplots are plotted on a log scale. The black lines on the contour indicates the time of axial flow slack tide, with flood tide from 6h00 to 12h00 and ebb tide from 12h30 to 17h30.

Just after slack after flood tide there is an increase in $\overline{\epsilon}$, which is seen in both the depth averaged plot (Figure 3.8a2) and the distance and depth averaged plot, where after the initial decrease during slack tides there is a sharp increase in $\overline{\epsilon}$. This elevated $\overline{\epsilon}$ during slack after flood was also seen in Ross et al. (2019), and was specifically seen near surface, decoupled from bottom boundary friction, at one location across the estuary.

Elevated TKE dissipation, ϵ, occurs near slack after flood near the surface at the three stations across the estuary (see Figure 3.9). This increase in dissipation corresponds to an increase in near surface shear. This is a result of forcing from the lateral baroclinic pressure gradient driving surface secondary flows during slack tides, as seen in Chambers et al. (submitted). The forcing induces near surface squared vertical secondary flow shear, and in addition near surface elevated squared vertical axial shear is seen as well. On the right side of the estuary near Royan, there is also elevated ϵ, $\sim 10^{-5.5}$ W/kg that was not seen in the

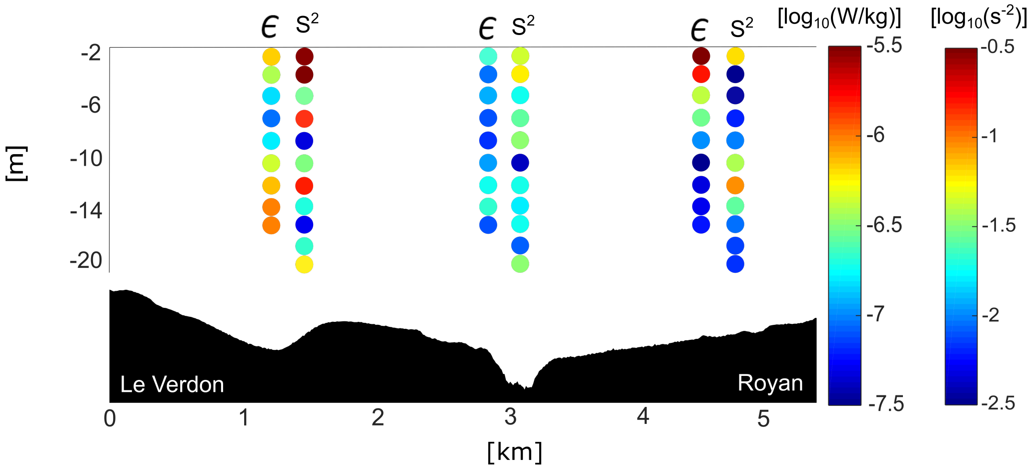

Figure 3.9. Depth varying TKE dissipation and squared vertical shear near slack after flood. Dissipation, ϵ, and squared vertical shear, S^2, near slack after flood varying with depth and provided for three stations across the estuary. The orientation of the cross section, looking seaward, is indicated by Le Verdon labeled on the left side and Royan labeled on the right side of the bathymetry.

depth average. This suggests that there is a bias with the depth average that may hide some of the near surface features seen in Figure 3.9.

The range of distance averaged $\bar{\epsilon}$ is 1 order of magnitude while the range of time averaged $\bar{\epsilon}$ is 0.5 orders of magnitude, signifying that $\bar{\epsilon}$ is more time dependent than distance dependent. However, the depth and time averaged dissipation shows significantly more lateral variability than past studies. Collignon and Stacey (2013) studied dissipation on a shoal-channel interface and found a lateral range in depth averaged TKE dissipation of 0.005 orders of magnitude, with higher dissipation values in the channel. Another study by Huguenard et al. (2015) investigated spacial (depth and distance) and temporal changes in dissipation and found elevated TKE dissipation over the shoals, however this lateral pattern was not apparent in the vertical eddy viscosity.

3.5.6 Vertical Eddy Viscosity

Temporal variations in $\overline{Az}$ show mixing increasing during both flood and ebb, with elevated $\overline{Az}$ during ebb (Figure 3.10). After slack after flood $\overline{Az}$ increases, the same pattern that is seen with TKE dissipation and by Ross et al. (2019), which is driven by increased

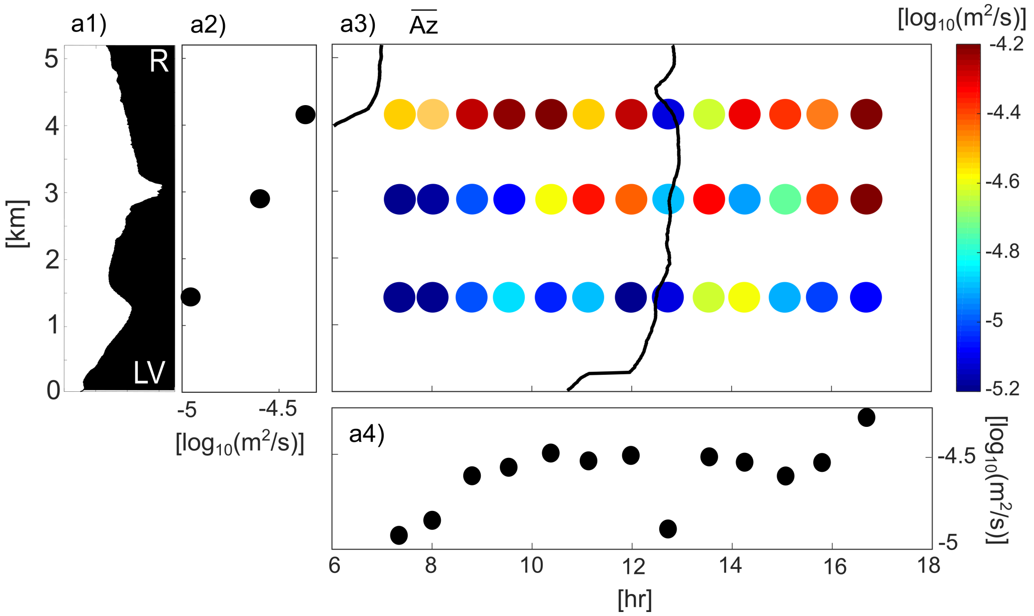

Figure 3.10. Vertical eddy viscosity with time and cross channel distance. (a1) The bathymetry with the Royan bank is indicated by ‘R’ at 5 km across and the Le Verdon bank is indicated by ‘LV’ at 0 km across. (a2) Depth and time averaged vertical eddy viscosity. (a3) Depth averaged vertical eddy viscosity, varying with time (x-axis) and distance across the estuary (y-axis). (a4) Depth and distance averaged vertical eddy viscosity. All subplots are plotted on a log scale. The black lines on the contour indicates the time of axial flow slack tide, with flood tide from 6h00 to 12h00 and ebb tide from 12h30 to 17h30.

near surface shear. Aside from the increase after slack after flood, there is a general decrease in $\overline{Az}$ during slack tides. This temporal pattern indicates that increased $\overline{Az}$ is correlated with increased axial flows, as seen in Ralston and Stacey (2006), Rippeth et al. (2001), and Wiles et al. (2006). The variation with time resembles squared vertical shear, which shows decreased values during slack after ebb and elevated values during both flood and ebb, with a clear increase in shear over ebb tide (Figure 3.5c3). Additionally, TKE dissipation exhibits the same local minima during slack tides, again with a general increase in values over both flood and ebb (Figure 3.8a3). Several of the influencing mechanisms of mixing display increasing values over ebb tide, but TKE dissipation and shear are the only ones that show increasing values over flood tide as well. This correlation indicates that shear and TKE dissipation drive the temporal variations in vertical eddy viscosity.

A time average of $\overline{Az}$ (Figure 3.10a2) increases across the estuary from the Le Verdon side to the Royan side. At 1.5 km across the time averaged $\overline{Az}$ is 10^{-5} m^2/s and increases at 3 km to $10^{-4.5}$ m^2/s. On the Royan side of the estuary the time averaged $\overline{Az}$ is highest, $10^{-4.25}$ m^2/s. This cross channel pattern is very similar to the time averaged $\overline{\epsilon}$ (Figure 3.8a2) and can be linked to elevated axial flows (Figure 3.4a) on the Royan side of the estuary, as peaks in axial flow have been found to initiate elevated mixing (Ralston and Stacy, 2006; Rippeth et al., 2001, 2002; Wiles et al., 2006).

The distance averaged $\overline{Az}$ provides enough resolution to see variability across the estuary with time (Figure 3.10a3). At slack after ebb the distance averaged $\overline{Az}$ is lowest, 10^{-5} m^2. At the beginning of flood $\overline{Az}$ increases and by the end of flood the distance averaged $\overline{Az}$ is $10^{-4.5}$ m^2/s. At slack after flood there is a decrease in $\overline{Az}$ to 10^{-5} m^2/s, and as ebb starts $\overline{Az}$ jumps back up to $10^{-4.5}$ m^2/s and continues to increase for the remainder of ebb, peaking at 17h00 at $10^{-4.25}$ m^2/s.

3.6 Discussion

This study aims to investigate the cross channel and temporal variations in mixing at the mouth of a macrotidal estuary during high river discharge. The influencing mechanisms of mixing determine the temporal and cross channel variation in vertical eddy viscosity. The temporal variability in vertical eddy viscosity exhibits increases in mixing over both flood and ebb with higher mixing values during ebb tide. During slack tides mixing is approximately half an order of magnitude lower than mixing during flood and ebb. The temporal variations are influenced primarily by shear and TKE dissipation, which prompt the increase in mixing over both flood and ebb. Vertical eddy viscosity was also found to consistently increase across the channel from the Le Verdon to Royan sides, a pattern attributed to the location of peak axial flows.

The range of eddy viscosity observed in the Gironde during high river discharge season is 10^{-5} to 10^{-4} m^2/s (Figure 3.10a1), a magnitude less than previous studies. Geyer (2010) proposed a typical range of vertical eddy viscosity in estuaries between 10^{-4} and 10^{-2} m^2/s. In a study conducted in the James River estuary, a partially mixed microtidal estuary, eddy viscosity values had a range of 10^{-5} to 10^{-3} m^2/s (Huguenard et al., 2015). Observations from in the Hudson River, a partially mixed estuary, found eddy viscosity between 10^{-3} and 10^{-2} m^2/s despite exhibiting higher stratification than the Gironde, with Richardson numbers that frequently exceeded the critical value of 0.25 (Geyer et al., 2000).

A study conducted at the mouth of the Gironde during low river discharge season shows eddy viscosity as high as 10^{-1} m^2/s (Ross et al., 2019). The vertical eddy viscosity is dependent on the ratio of dissipation (ϵ) to production (approximated by S^2) and a mixing efficiency. This ratio means that when there is a high dissipation rate in relation to production, there is increased mixing. Essentially production, in the form of shear, provides energy to the system. Dissipation, which is a function of shear, takes energy away from the system by transferring energy to smaller scales and ultimately converting it to heat. The ratio of the two describes the momentum being mixed by turbulent eddies. When there is significantly more production in the system than dissipation, which is seen in the Gironde during high river discharge, there is a relatively low amount of energy being mixed. This explains why mixing is lower during high river discharge than lower river discharge.

3.6.1 Wind

Wind has been shown to induce mixing in estuaries (Burchard, 2009; MacCready et al., 2008; Stacey et al., 2011) and therefore a quantification of wind induced dissipation is necessary to determine if dissipation observed is driven by wind. During the field campaign wind velocities reached a maximum of 4 m/s (see Figure 3.2c). A method to estimate wind induced dissipation is presented in Csanady (1979) and used to compare with observed dissipation from VMP measurements. Wind induced dissipation, ϵ_w, is quantified as

$$\epsilon_w = \left(\frac{\rho_{air} C_D |u_w^2|}{\rho_{water}}\right)^3 \frac{1}{\kappa z}, \tag{3.13}$$

where ρ_{air} is the density of air, 0.0012 kg/m^3, C_D is the drag coefficient, u_w is the wind velocity, ρ_{water} is the density of the sea water, κ is the von-Karman constant, 0.41, and z is the depth in sigma-coordinates (Csanady, 1979; Ross et al., 2019). The drag coeffient is a function of the wind velocity and is expressed as $C_D = 0.001(1.1 + 0.35 \times u_w)$.

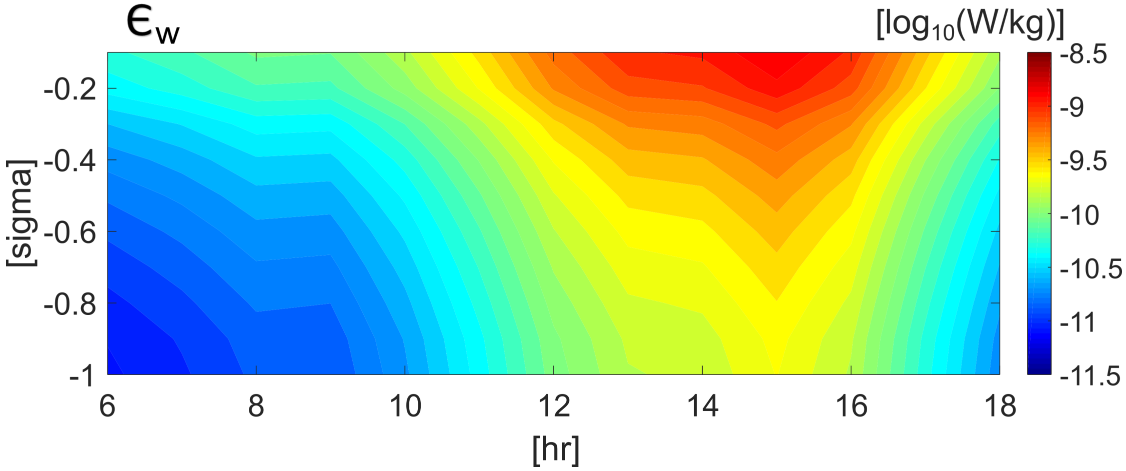

Figure 3.11. Wind induced TKE dissipation. Wind induced TKE dissipation plotted on a log scale varying with time and sigma coordinates.

The wind induced dissipation calculated following Csanady (1979) shows dissipation values ranging from $10^{-11.5}$ to $10^{-8.5}$ W/kg (Figure 3.11), which are three orders of magnitude lower that dissipation measured by the VMP (see Figure 3.8), concluding that wind induced dissipation is negligible.

3.6.2 Limitations

The model provides salinity at the surface and at the bottom of the channel at 10 points across the cross section. As a result, calculations of stratification and squared buoyancy frequency were reliant on only those two depth measurements, and the squared buoyancy frequency is considered a depth average assuming the change in salinity with depth is constant, or there is continuous stratification. There may be a pycnocline that is unaccounted for by this assumption which would alter the depth averaged squared buoyancy frequency, which in turn would alter the Richardson number. For a more accurate representation of squared buoyancy frequency and for the quantification of a depth-varying eddy viscosity, a finer vertical resolution of salinity is needed.

3.7 Chapter Conclusions

This study investigated intratidal and cross channel variations in hydrodynamic properties that influence mixing in a partially mixed, macrotidal estuary with complex bathymetry. The results conclude that there is both temporal and cross channel variability of hydrodynamic processes that influence the magnitude variability of mixing. Squared vertical shear, buoyancy frequency, and the Richardson number show cross channel variability that is dependent on depth and therefore change in relation to the bathymetry, with increased values over shallow areas. Additionally, TKE dissipation shows variation across the channel and temporal asymmetries which, in conjunction with the other influencing mechanisms, produce a laterally and temporally varying vertical eddy viscosity. The relatively low mixing values can be explained by a low dissipation to production ratio, driven by elevated squared vertical shear.

Understanding the temporal and cross channel variability of hydrodynamic properties that affect mixing allows for the identification of processes responsible for the tidal and cross channel asymmetry of mixing. This study emphasizes that in addition to tidal variations, cross channel variations must be considered when evaluating mixing and the components that influence mixing in estuaries. Future research on the cross channel variability in hydrodynamic processes would benefit from increased resolution of dissipation measurements so that a connection between bathymetric changes and mixing can be identified.

3.8 Chapter Acknowledgements

Authors would like to thank Jean-Philippe Mauros, Guillaume Detandt (EPOC), and Energie de la Lune (EDL) for their help with data collection, as well as Pascal Brunet

(Bertin Technologies) for his support. This project was financially sponsored by the Bpifrance collaboration with the University of Bordeaux and is a contribution to the URABAILA Project. Data are available through http://dataverse.acg.maine.edu/dvn/dv/chambers.

CHAPTER 4

CONCLUSIONS

This thesis aims to determine the spatial and temporal variations of secondary flows and turbulent mixing in macrotidal estuaries. This work was carried out through a combination of in-situ collected data and numerical modeling and revealed that lateral variations in both secondary flows (and driving mechanisms) and mixing (and influencing mechanisms) are highly dependent upon cross-channel location, with the strength of this dependency varying throughout a tidal cycle.

The first objective of this thesis was to investigate the cross channel and temporal variations in forcing mechanisms of secondary flows in a macrotidal estuary. The results conclude that secondary flow circulation patterns vary intratidally and across the estuary as a result of variation in the forcing mechanisms, the baroclinic pressure gradient, Coriolis, and curvature. In addition, the combination of curvature and Coriolis induced a lateral sea surface slope that influenced surface secondary flows during ebb tide, and was a prominent forcing mechanism driving secondary subtidal flows.

The second objective of this thesis was to investigate the cross channel and temporal variations in mixing in a macrotidal estuary during high river discharge. This was done through an analysis of the mechanisms that influence mixing, which were found to vary with time and across the channel, exhibiting variation in response to changes in bathymetry. As a result of these influencing mechanisms, mixing was found vary with time and distance across the estuary, with lateral variability in mixing tied to the lateral asymmetry in peak axial flow. The atypically low mixing levels were attributed to a low dissipation to production ratio, which is thought to be a result of the elevated freshwater input contributing to increased levels of production in the form of shear.

Many studies investigating estuarine dynamics focus on time and depth dependency and neglect cross-estuary variations. These results show that there can be significant lateral changes in estuarine dynamics in macrotidal estuaries that need to be taken into consideration when analyzing these systems. The dependency on topographic and bathymetric features suggests that changes to the geometry of a macrotidal system, such as coastline infrastructure and dredging, can impact estuarine hydrodynamics, which can affect the health of an estuary. Secondary flows have been shown to induce mixing, which is tied to sediment transport and particle distribution. If these processes change, that means that the retention time and distribution of sediments and particles such as toxins, can change as well. This can have negative affects, with sediments building up in navigation channels and toxins staying inside of the estuary longer, increasing their concentration and threatening biological life. Additionally, if industries and communities release their runoff at strategic locations along the estuary to decrease the retention rate of possible pollutants, the change in hydrodynamic processes spurred by changes in the channel geometry could mean that these release points are no longer suitable. Increases levels of pollutants or suspended sediments in estuaries could affect fish and plant life, and as a result affect communities reliant on the estuary for fishing. Additionally, if sediment transport patterns change this could affect the depth of navigation channels or erode beaches, affecting recreation, shipping, and transportation in the estuary. As shorelines are built up and navigational channels are dredged, their changes on the hydrodynamic processes must be considered to ensure that the health of the estuary does not decline and affect the surrounding communities.

Future studies on the lateral variability of hydrodynamics in a macrotidal estuary would benefit from studying the along channel variability of intratidal flows and mixing to fully understand the inter-connectivity of generating mechanisms of secondary flows in a region of curvature and to understand what drives the variability in mechanisms that influence mixing. Additionally, a more complete cross sectional data collection of TKE dissipation would allow for a more thorough analysis of how changes in bathymetry affect mixing.

REFERENCES

Abril, G., Etcheber, H., Le Hir, P., Bassoullet, P., Boutier, B., & Frankignoulle, M. (1999). Oxic/anoxic oscillations and organic carbon mineralization in an estuarine maximum turbidity zone (The Gironde, France). *Limnology and Oceanography*, **44**, 1304-1315

Allen, G.P. (1972). Etude des processus sedimentaires dans l'estuaire de la Gironde, *PhD Thesis*, University of Bordeaux, France.

Allen, G.P., & Castaing, P. (1973). Suspended sediment transport from the Gironde estuary (France) into the adjacent continental shelf. *Marine Geology*, **14**, M47 - M53.

Allen, G.P., Salomon, J.C., Bassoullet, P., Du Penhoat, Y., & De Grandpré, C. (1980). Effects of tides on mixing and suspended sediment transport in macrotidal estuaries. *Sedimentary Geology*, **26**, 69 - 90.

Basdurak, N.B, Huguenard, K.D., Valle-Levinson, A., Li, M., & Chant, R.J. (2017). Parameterization of mixing by secondary circulation. *Journal of Geophysical Research*, **122** 5666 - 5688. doi: 10.1002/2016JC012328

Basdurak, N.B. & Valle-Levinson, A. (2013). Tidal variability of lateral advection in a coastal plain estuary. *Coastal Shelf Research*, **61-62**, 85 - 97.

Becherer, J., Stacey, M.T., Umlauf, L., & Burchard, H. (2015). Lateral circulation generates flood tide stratification and estuarine exchange flow in a curved inlet. *Sedimentary Geology*, **26**, 69 - 90.

Brand, A., Lacy, J.R, Hsu, K., Hoover, D., Gladding, S., & Stacey, M.T. (2010). Wind-enhanced resuspension in the shallow waters of south San Francisco Bay: Mechanisms and potential implications for cohesive sediment transport. *Journal of Geophysical Research*, **115**, C11024. doi: 10.1029/2010JC006172..

Brenon, I., & Le Hir, P. (1999). Modelling the tubidity maximum in the Seine estuary (France): identification of formation processes. *Estuarine, Coastal, and Shelf Science*, **49**, 525 - 544.

Buijsman, M.C. & Ridderinkhof, H. (2008). Variability of secondary currents in a weakly stratified tidal inlet with low curvature. *Continental Shelf Research*, **28**, 1711 - 1723.

Burchard, H. (2009). Combined effects of wind, tide and horizontal density gradients on stratification in estuaries and coastal seas. *Journal of Physical Oceanography*, **39**, 2117 - 2136.

Burchard, H. & Hetland, R.D. (2010). Quantifying the contributions of tidal straining and gravitational circulation to residual circulation in periodically stratified tidal estuaries. *Journal of Physical Oceanography*, **40**, 1243 - 1262.

Cameron, W.M. & Pritchard, D.W. (1963). Estuaries. In: M. N. Hill (ed.) *The Sea.* **Vol 2**, New York: John Wiley and Sons, Inc. 306 - 324.

Castaing, P., & Allen, G.P. (1981). Mechanisms controlling seaward escape of suspended sediment from the Gironde: a macrotidal estuary in France. *Marine Geology*, **40**, 101 - 118.

Chant, R.J. (2010). Chapter 5: Estuarine secondary circulation. In: Valle-Levinson, A. (Ed), *Contemporary Issues in Estuarine Physics*, University Press. 100-124.

Chant, R.J. (2012). Secondary circulation in a region of flow curvature: Relationship with tidal forcing and river discharge. *Journal of Geophysical Research*, **107**. doi: 10.1029/2001JC001082.

Chant, R.J., Geyer, W.R., Houghton, R.H., Hunter, E., & Lerczak, J. (2007). Estuarine boundary layer mixing processes: insights from dye experiments. *Journal of Physical Oceanography*, **37**, 1859 - 1877.

Chant, R.J., Sommerfield, C.K., & Talke, S.A. (2018). Impact of Channel Deepening on Tidal and Gravitational Circulation in a Highly Engineered Estuarine Basin. *Estuaries and Coasts*, doi: 10.1007/s12237-018-0379-6.

Chambers, R., Ross, L., & Sottolichio, A. (submitted). Spaciotemporal variations in drivers of secondary flow in a macrotidal estuary. *Journal of Geophysical Research.*

Chen, S-N., Sanford, L.P., & Ralston, D.K. (2009). Lateral circualtion and sediment transport driven by axial winds in an idealized, partially mixed estuary. *Journal of Geophysical Research*, **114**, C12006. doi: 10.1029/2008JC005014.

Cloern, J. (1991). Tidal stirring and phytoplankton bloom dynamics in an estuary. *Journal of Marine Research*, **49**, 203 - 221.

Collignon, A., & Stacey, M. (2013). Turbulence dynamics at the shoal-channel interface in a partially stratified estuary. *Journal of Physical Oceanography*, **43**, 970 - 989. doi: 10.1175/JPO-D-12-0115.1

Craig, P.D. & Banner, M.L. (1994). Modeling waves-enhanced turbulence in the ocean surface layer. *Journal of Physical Oceanography*, **24**, 2546 - 2559.

Csanady, G.T. (1978). Turbulent interface layers. *Journal of Geophysical Research*, **83(C5)**, 2329.

Cugier, P. & Le Hir, P. (2002). Development of a 3D hydrodynamic model for coastal ecosystem modelling. Application to the plume of the Seine river (France). *Estuarine, Coastal, and Shelf Science*, **55**, 673 - 695.

Davidson, P. A. (2015). Turbulence, an introduction for scientists and engineers. **2nd Ed.**, Oxford, UK: Oxford University Press.

Davies, L.J. (1964). A morphogenic approach to the worlds' shorelines. *Zeitschrift für Geomorphologie*, **8**, 127 - 142.

de Jong, V.N., Schuttelaars, J.E., van Beusekom, J.E., Talke, S.A., & de Swart, H.E. (2014). The influence of channel deepening on estuarine turbidity levels and dynamics, as exemplified by the Ems estuary. *Estuarine, Coastal and Shelf Science*, **139**, 46 - 59.

Dunckley, J.F., Koseff, J.R., Steinbuck, J.V., Monismith, S.G., & Genin, A. (2012). Comparison of mixing efficiency and vertical diffusivity models from temperature microstructure. *Journal of Geophysical Research*, **117 (C10008)**, doi:10.1029/2012JC007967.

Dyer, K.R. (1997). Estuaries: A physical introduction. Aberdeen, UK: John Wiley and Sons.

Efron, B. & Gong, G. (1983). A leisurely look at the bootstrap, the jackknife and cross-validation. *The American Statistician*, **37**, 36 - 48.

Fischer, H.B., List, E.J., Koh, R.C.Y., Imberger, J., and Brooks, N.H. (1979). Mixing in inland and coastal waters. New York: Academic Press.

French, J.R. & Clifford, N.J. (1992). Characteristics and 'event-structure' of near-bed turbulence in a macrotidal saltmarsh channel. *Estuarine, Coastal and Shelf Science*, **34**, 49 - 69.

Friedrichs, C.T. & Aubrey, D.G. (1988). Non-linear tidal distortion in shallow well-mixed estuaries: a synthesis. *Estuarine, Coastal and Shelf Science*, **27**, 521-545.

Friedrichs, C.T. & Hamrick, J.M. (1996). Effects of channel geometry on cross-sectional variation in along-channel velocity in partially mixed tidal estuaries. In: Aubrey, D.G., Friedrichs, C.T. (Eds). *Buoyancy Effects on Coastal and Estuarine Dynamics*, Washington, D.C., American Geophysical Union. 265 - 281.

Galperin, B., Kantha, L.H., Hassid, S., & Rosati, A. (1988). A quasi-equilibrium turbulent energy model for geophysical flows. *Journal of Atmospheric Science*. **62**, 45 - 55.

Garvine, R.W. (1995). A dynamical system for classifying buoyant coastal discharges. *Continental Shelf Research.* **15(13)**, 1585 - 1596.

Geyer, W.R. (1993). The importance of supression of turbulence by stratification on the estuarine turbidity maximum. *Estuaries*, **16**, 113 - 125.

Geyer, W.R. (1997). Influence of wind on dynamics and flushing of shallow estuaries. *Estuarine, Coastal, and Shelf Science*, **44(6)**, 713-722. doi:10.1006/ecss.1996.0140.

Geyer, W.R. (2010). Chapter 2: Estuarine salinity structure and circulation. In: Valle-Levinson, A. (Ed), *Contemporary Issues in Estuarine Physics*, University Press. 12 - 26.

Geyer, W.R., Scully, M.E., & Ralston, D.K. (2008). Quantifying vertical mixing in estuaries. *Environmental Fluid Mechanics*, **8**. 495 - 509.

Geyer, W.R., Signell, R.P., & Kineke, G.C. (1998). Lateral trapping of sediment in a partially mixed estuary. *Physics of Estuaries and Coastal Seas*, 115 - 126.

Geyer, W.R., Trowbridge, J.H., & Bowen, M.M. (2000). The dynamics of a partially mixed estuary. *Journal of Physical Oceanography*, **30**, 2035 - 2048.

Guymer, I., & West, J.R. (1992). Longitudinal dispersion coefficients in an estuary. *Journal of Hydraulic Engineering*, **118**, 718 - 734.

Hansen, D.V., & Rattray, M. (1965). Gravitational Circulation in straights and estuaries. *Journal of Marine Research*, **23**, 104 - 122.

Huguenard, K.D., Valle-Levinson, A., Li, M., Chant, R.J., & Souza, A.J. (2015). Linkage between lateral circulation and near surface vertical mixing in a coastal plain estuary. *Journal of Marine Research*, **120**, 4048 - 4067. doi: 10.1002/2014JC010679.

Huijts, K.M.H., Schuttelaars, H.M., de Swart, H.E., & Friedrichs, C.T. (2009). Analytical study of the transverse distribution of along channel and transverse residual flows in tidal estuaries. *Continental Shelf Research*, **29**, 89 - 100.

Jalon-Rojas, I., Schmidt, S., & Sottolichio, A. (2015). Turbidity in the fluvial Gironde Estuary (southwest France) based on 10-year continuous monitoring: sensitivity to hydrological conditions. *Hydrologic Earth Systems Science*, **19**, 2805 - 2819. doi: 10.5194/hess-19-2805-2015.

Jay, D.A. & Kukulka, T. (2003). Revising the paradigm of tidal analysis - the uses of non-stationary data. *Ocean Dynamics*, **53(3)**, 110 - 125. https://doi.org/10.1007/s10236-003-0042-y

Jay, D.A. & Musiak, J.D. (1994). Particle trapping in estuarine tidal flows. *Journal of Geophysical Research*, **96(C11)**, 20585 - 20598.

Jay, D.A. & Smith, J.D. (1990). Circulation, density distribution and neap-spring transition in the Columbia River Estuary. *Progress in Oceanography*, **25**, 81 - 112.

Ji, Z-G. (2008). Hydrodynamics and Water Quality: Modeling Rivers, Lakes, and Estuaries. Hoboken, NJ: John Wiley & Sons, Inc.

Joyce, T.M. (1989). In situ calibration of ship-board ADCPs. *Journal of Atmospheric and Oceanic Technology*, **99**, 20445 - 20461.

Kalkwijk, J.P.T. & Booij, R. (1986) Adaptation of secondary flow in nearly-horizontal flow. *Journal of Hydraulic Engineering*. **24**, 19 - 37.

Kasai, A., Hill, A.E., Fujiwara, T., & Simpson, J.H. (2000) Effect of Earth's rotation on the circulation in regions of freshwater influence. *Journal of Geophysical Research*. **105(C7)**, 16961 - 16969.

Kasai, A., Kurikawa, Y., Ueno, M., Robert, D., Yamashita, Y. (2010). Salt-wedge intrusion for phytoplankton dynamics in the Yura Estuary, Japan. *Estuarine, Coastal, and Shelf Science*, **86(3)**, 408 - 414.

Kay, D. J. & Jay, D. A. (2003) Interfacial mixing in a highly stratified estuary: 1. Characteristics of Mixing. *Journal of Marine Research*. **108(C3)**, 3072.doi:10.1029/2000JC000252.

Koseff, J., Holen, J., Monismith, S., & Cloern, J. (1993). Coupled effects of vertical mixing and benthic grazing on phytoplankton populations in shallow, turbid estuaries. *Journal of Marine Research*, **51**, 843 - 868.

Lajaunie-Salla, K., Wild-Allen, K., Sottolichio, A., Thouvenin, B., Litrico, X., & Abril, G. (2017). Impact of urban effluents on summer hypoxia in the highly turbid Gironde Estuary, applying a 3D model coupling hydrodynamics, sediment trasport and biogeochemical processes. *Journal of Marine Systems*, **174** 89 - 105. https://doi.org/10.1016/j.jmarsys.2017.05.009

Le Cann, B. (1990). Barotropic tidal dynamics of the Bay of Biscay shelf: observations, numerical modelling and physical interpretation. *Continental Shelf Research*, **10**, 723 - 758.

Lerczak, J.A. & Geyer, W. R. (2004). Modeling the lateral circulation in straight, stratified estuaries. *Journal of Physical Oceanography*, **34**, 1410 - 1428.

Li, C., & O'Donnell, J. (2005). The effect of channel length on the residual circulation in tidally dominated channels. *Journal of Physical Oceanography*, **35**, 1826-1840.

Lieberthal, B., Huguenard, K., Ross, L., & Bears, K. (2019). The generation of overtides in flow around a headland in a low inflow estuary. *Journal of Geophysical Research*, **124**, https://doi.org/10.1029/2018JC014039.

Li, M., Cheng, P., Chant, R., Valle-Levinson, A., & Arnott, K. (2014). Analysis of vortex dynamics of lateral circulation in a straight tidal estuary. *Journal of Physical Oceanography*, **44**, 2779 - 2795. doi: 10.1175/JPO-D-13-0212.1.

Li, M., Trowbridge, J.H., & Geyer, W.R. (2008). Asymmetric tidal mixing due to the horizontal density gradient. *Journal of Physical Oceanography*, **38**, 418 - 434.

Li, Y., and Li, M. (2011) Effects of winds on stratification and circulation in a partially mixed estuary. *Journal of Geophysical Research.* **116**, doi: 10.1029/2010JC006893.

Lueck, R. (2013). Measuring tidal channel turbulence with a Vertical Microstructure Profiler (VMP). *Rockland Scientific Technical Note 026.*

Lwiza, K.M.M., Bowers, D.G., & Simpson, J.H. (1991) Residual and tidal flow at a tidal mixing front in the North Sea. *Continental Shelf Research*, **11(11)**, 1379 - 1395.

MacCready, P., Banas, N., Hickey, B., Dever, E., & Liu, Y. (2008). A model study of tide- and wind-induced mixing in the Columbia River estuary and plume. *Continental Shelf Research*, **29**, 278 - 291. doi:10.1016/j.csr.2008.03.015

MacCready, P., & Geyer, W.R. (2010). Advances in estuarine physics. *Annual Review of Marine Sciences*, **2**, 35 - 58.

MacCready. P., Hetland, R., & Geyer, W. (2002). Long term isohaline salt balance in an estuary. *Continental Shelf Research*, **22**, 1591 - 1601.

Migniot, C. (1971) L'évolution de la Gironde au cours des temps. *Bull. Inst. Geol. Bassin Aquitaine.* **11**, 221 - 281.

Miles, J. (1961). On the stability of heterogeneous shear flows. *Journal of Fluid Mechanics.* **417**, 58 - 63.

Monismith, S. (2010). Chapter 7: Mixing in estuaries. In: Valle-Levinson, A. (Ed), *Contemporary Issues in Estuarine Physics*, University Press. 145 - 185.

Monismith, S. (1986). An experimental study of the upwelling response of stratified reservoirs to surface shear stress. *Journal of Fluid Mechanics.* **171**, 407 - 439. doi: 10.1017/S0022112086001507.

Nepf, H.M. & Geyer, W.R. (1996). Intra-tidal variations in stratification and mixing in the Hudson estuary. *Journal of Geophysical Research*, **101**, 12079 - 12086.

Nidzieko, N.J., Hench, J.L., & Monismith, S.G. (2009). Lateral circulation in well-mixed and stratified estuarine flows with curvature. *Journal of Physical Oceanography*, **39**, 831 - 851. doi: 10.1175/2008JPO4017.1.

NOAA, National Ocean and Atmospheric Association (2005). NOAA Ocean Service Education: Estuaries [Online]. Available: `https://aamboceanservice.blob.core.windows.net/oceanservice-prod/education/tutorial_estuaries/lessons/estuaries_tutorial.pdf` (2005, June 08).

Nunes, R. & Simpson, J. (1985). Axial convergence in a well mixed estuary. *Estuarine Coastal Shelf Science*, **20**, 637 - 649.

Officer, C.B. (1976). Physical Oceanography of Estuaries (and associated coastal waters). New York: John Wiley.

Pieterse, A., Puleo, J.A., McKenna, T.E., & Aiken, R.A. (2015). Near-bed shear stress, turbulence production and dissipation in a shallow and narrow tidal channel. *Earth Surface Processes and Landforms* **40**, 2059 - 2070. doi: 10.1002/esp.3782

Pein, J., Valle-Levinson, A., & Stanev, E.V. (2018). Secondary circulation asymmetry in a meandering, partially stratified estuary. *Journal of Geophysical Research: Oceans*, **123**, 1670 - 1683. https://doi.org/10.1002/2016JC012623

Peters, H. (1997). Observations of stratified turbulent mixing in an estuary: Neap-to-spring variations during high river flow. *Estuarine, Coastal and Shelf Science*, **45**, 69 - 88.

Peters, H. (1999). Spacial and temporal variability of turbulent mixing in an estuary. *Journal of Marine Research*, **57**, 805 - 845.

Peters, H. & Bokhorst, R. (2000). Microstructure observations of turbulent mixing in a partially mixed estuary, Part II: Salt flux and stress. *Journal of Physical Oceanography*, **31**, 1105 - 1119.

Prandle, D.W. (1982). The vertical structure of tidal currents and other oscillatory flows. *Continental Shelf Research*, **1(2)**, 191 - 207.

Prandle, D.W. (2004). Saline intrusion in partially mixed estuaries. *Estuarine, Coastal, and Shelf Science*, **59(3)**, 385 - 397.

Prandle, D.W. (2006). Dynamical controls on estuarine bathymetry: Assessment against UK database. *Estuarine, Coastal, and Shelf Science*, **68(1)**, 282 - 288.

Prandle, D.W. (2009). Estuaries: dynamics, mixing, sedimentation, and morphology. Cambridge, NY: Cambridge University Press.

Pritchard, D.W. (1952). Estuarine hydrography. *Advanced Geophysics*, **1**, 243 - 280.

Pritchard, D.W. (1956). The dynamic structure of a coastal plain estuary. *Journal of Marine Research*, **20**, 121 - 133.

Pein, J., Valle-Levinson, A., and Stanev, E.V. (2018). Secondary circulation asymmetry in a meandering, partially stratified estuary. *Journal of Geophysical Research: Oceans*, **123**, 1670 - 1683. doi: 10.1002/2016JC012623.

Ralston, D.K. & Stacey, M.T. (2006). Shear and turbulence production across subtidal channels. *Journal of Marine Research*, **64**, 147 - 171. doi: 10.1357/002224006776412359

Rippeth, T.P., Fisher, N.R. & Simpson, J.H. (2001). The cycle of turbulent dissipation in the presence of tidal straining. *Journal of Physical Oceanography*, **31**, 2458 - 2471.

Rippeth, T.P., Williams, E., & Simpson, J.H. (2002). Reynolds stress and turbulent energy production in a tidal channel. *Journal of Physical Oceanography*, **32**, 1242 - 1251.

Ross, L., Huguenard, K.D., & Sottolichio, A. (2019). Intratidal and fortnightly variability of vertical mixing in a macrotidal estuary: the Gironde. *Journal of Geophysical Research*, https://doi.org/10.1029/2018JC014456

Ross, L. & Sottolichio, A. (2016). Subtidal variability of sea level in a macrotidal and convergent estuary. *Continental Shelf Research*, **131**, 28 - 41. doi: 10.1016/j.csr.2016.11.005.

Ross, L., Valle-Levinson, A., Sottolichio, A., & Huybrechys, N. (2017). Lateral variability in the mid-reaches of a macrotidal estuary. *Journal of Geophysical Research*, **122**, 7651 - 7673. doi: 10.1002/2016JC012504.

Sanford, L. (1994). Wave-forced resuspension of upper Chesapeake Bay muds. *Estuaries*, **17(1B)**, 148 - 165.

Savenije, H.H.G. (2006). Salinity and tides in alluvial estuaries. Amsterdam, Netherlands: Elsevier Science & Technology.

Scully, M.E., & Friedrichs, C.T. (2007). The importance of tidal and lateral asymmetries in stratification to residual circulation in partially mixed estuaries. *Journal of Physical Oceanography*, **37**, 1496 - 1511.

Scully, M.E. & Geyer, W.R. (2012). The role of advection, straining, and mixing on the tidal variability of estuarine circulation. *Journal of Physical Oceanography*, **42**, 855 - 868. doi:10.1175/JPO-D-10-05010.1.

Scully, M.E., Geyer, W.R., & Lerczak, J.A. (2009). The influence of lateral advection on the residual estuarine circulation: a numerical modeling study of the Hudson River estuary. *Journal of Physical Oceanography*, **39**, 107 - 124.

Seim, H.E. & Gregg, M.C. (1997). The importance of aspiration and channel curvature in producing strong vertical mixing over a sill. *Journal of Geophysical Research*, **102**, 3451 - 3472.

Simpson, J.H., Brown, J., Matthews, J., & Allen, G. (1990). Tidal straining, density curents, and stirring in the control of estuarine stratification. *Estuaries*, **13**, 125 - 132.

Simpson, J.H., Williams, E., Brasseur, L.H. & Brubaker, J.M. (2005). The impact of tidal straining on the cycle of turbulence in a partially stratified estuary. *Continental Shelf Research*, **25**, 51 - 64.

Smith, R. (1996). Combined effects of buoyancy and tides upon longitudinal dispersion. Buoyancy effects on coastal and estuarine dynamics. *American Geophysical Union*, 319 - 329.

Sottolichio, A., Le Hir, P., & Castaing, P. (2001). Modelling mechanisms for the turbidity maximum stability in the Gironde estuary, France. In: McAnally, W. H., Mehta, A. J. (Eds), *Coastal and Estuarine Fine Sediment Processes*, Amsterdam: Elsevier, 373 - 386.

Stacey, M.T., Burau, J.R., & Monismith, S.G. (2001). Creation of residual flows in a partially stratified estuary. *Journal of Geophysical Research*, **106**, 17013 - 17037.

Stacey, M.T., Monismith, S.G., & Burau, J.R. (1999). Observations of turbulence in a partially stratified estuary. *Journal of Physical Oceanography*, **29**, 1950 - 1970.

Stacey, M.T. & Ralston, D.K. (2005). The scaling and structure of the estuarine bottom boundary layer. *Journal of Physical Oceanography*, **35**, 55 - 71.

Stacey, M.T., Rippeth, T.D., and Nash, J.D. (2011). Turbulence and stratification in estuaries and coastal seas. *Reference Module in Earth Systems and Environmental Sciences*, **2**, 9 - 35. doi: 10.1016/B978-0-12-374711-2.00204-7

Statham, P.J. (2012). Nutrients in estuaries - An overview and the potential impacts of climate change. *Science of the Total Environment*, **434**, 213 - 227.

Talke, S.A., de Swart, H.E., & de Jong, V. (2009) An idealized model and systematic process study of oxygen depletion in highly turbid estuaries. *Estuaries and Coasts*, **32 (4)**, 602 - 620.

Tenorio-Fernandez, L., Valle-Levinson, A., & Gomez-Valdes, J. (2018). Subtidal hydrodynamics in a tropical lagoon: A dimensionless numbers approach. *Estuarine, Coastal and Shelf Science*, **200**, 449 - 459. doi: 10.1016/j.ecss.2017.11.037.

Thomson, R.E. & Emery, W.J. (2014). Data Analysis Methods in Physical Oceanography, Third Edition. *Elsevier Science*.

Thorpe, R.E. (2007). Measurement of Ocean Turbulence. In: An Intrroduction to Ocean Turbulence. New York: Cambridge University Press, 37 - 76.

Tjernstrom, M. (1993). Turbulence length scales in a stably stratified free shear flow analyzed from slant aircraft profiles. *Journal of Applied Meteorology*, **32**, 948 - 963.

Tomczak, M. & Godfrey, J.S. (1994). Regional Oceanography: an Introduction. Oxford, England; New York: Pergamon Press.

Traynum, S. & Styles, R. (2007). Flow, stress and sediment resuspension in a shallow tidal channel. *Estuaries and Coasts*, **30**, 94 - 101.

Turner, J.S. (1973). Buoyancy Effects in Fluids. Cambridge, UK: Cambridge University Press.

Valle-Levinson (2010). Chapter 1: Definition and classification of estuaries. In: Valle-Levinson, A. (Ed), *Contemporary Issues in Estuarine Physics*, University Press. 1 - 11.

Valle-Levinson, A., Reyes, C., & Sanay, R. (2003). Effects of bathymetry, friction, and rotation on estuary-ocean exchange. *Journal of Physical Oceanography*, **33**, 2375 - 2393.

van Maanen, B. & Sottolichio, A. (2018). Hydro- and sediment dynamics in the Gironde estuary (France): Sensitivity to seasonal variations in river inflow and sea level rise. *Continental Shelf Research*, **165**, 37 - 50.

Walsh, J.J. (1988). On the nature of continental shelves. New York: Academy Press.

Wargula, A., Raubenheimer, B., & Elgar, S. (2018). Curvature- and wind- driven cross-channel flows at an unstratified tidal bend. *Journal of Geophysical Research*, **123**, 3832 - 3843.

Wei, W., Zhijun, D., Xuefei, M., Paul, L., Shu, G., & Shushi, L. (2017). Shoal morphodynamics of the Changjiang estuary: Influences from river damming, estuarine hydraulic engineering and reclaiming projects. *Marine Geology*, **386**, 32 - 43.

West, J.R. & Mangat, J.S. (1986). Mechanisms controlling seaward escape of suspended sediment from the Gironde: a macrotidal estuary in France. *Estuarine, Coastal and Shelf Science*, **27**, 521 - 545.

Whitney, M.M., Codiga, D.L., Ullman, D.S., McManus, P.M., & Jiorle, R. (2012). Tidal cycles in stratification and shear and their relationship to gradient Richardson number and eddy viscosity variations in estuaries. *Journal of Physical Oceanography*, **42**, 1124 - 1133. doi: 10.1175/JPO-D-11-0172.1.

Wiles, P.J., Rippeth, T.P., Simpson, J.H.& Hendricks, P.J. (2006). A novel technique for measuring the rate of turbulent dissipation in the marine environment. *Geophysical Research Letters*, **33**, L21608. doi: 10.1029/2006GL027050

Winant, C.D. (2004). Three-dimensional wind-driven flow in an elongated, rotating basin. *Journal of Physical Oceanography*, **34(2)**, 462 - 476.

Woodruff, J.D., Geyer, W.R., Sommerfield, C. K., & Driscoll, N. W. (2001). Seasonal variation of sediment deposition in the Hudson River estuary. *Marine Geology*, **179**, 105 - 119.

Wong, K-C. (1994). On the nature of transverse variability in a coastal plain estuary. *Journal of Geophysical Research*, **99**, 14209 - 14222.

BIOGRAPHY OF THE AUTHOR

Rachel Chambers was born in Bolton, CT on October 7, 1995. She graduated from Bolton High School in 2013. She attended The University of Rhode Island where she graduated with a Bachelor's degree in Civil Engineering in 2017. In the summer of her Junior year until her enrollment at The University of Maine she interned at GM2 Associates based out of Glastonbury, CT where she worked on bridge and highway design projects. She entered the Civil Engineering graduate degree program at The University of Maine in the fall of 2017. After receiving her Master's Degree, Rachel will be joining Stantec in Maryland as a coastal engineering specialist. Rachel is a member of the American Society of Civil Engineers (ASCE) and participated in the University of Rhode Island ASCE Student Chapter as an undergraduate student. Rachel is a candidate for the Master of Science degree in Civil Engineering from The University of Maine in May 2019.

ƒ